Continuum Modeling of Two Battery Systems: Lithium-Sulfur and Rechargeable Hybrid Aqueous Cells

by

Mahmoudreza Ghaznavi

A thesis
presented to the University of Waterloo
in fulfillment of the
thesis requirement for the degree of
Doctor of Philosophy
in
Chemical Engineering

Waterloo, Ontario, Canada, 2015

I hereby declare that I am the sole author of this thesis. This is a true copy of the thesis, including any required final revisions, as accepted by my examiners.

I understand that my thesis may be made electronically available to the public.

Abstract

Mathematical models are powerful tools for understanding the mechanisms of a working battery. This thesis develops continuum mechanics models for two battery systems: lithium-sulfur (Li-S) and rechargeable hybrid aqueous battery (ReHAB). In both models, continuous partial differential equations and the Butler-Volmer equation are used to describe the diffusion/transfer of species in electrolyte and the electrochemical reactions at the electrode/electrolyte interface, respectively.

The first part of the thesis deals with modeling of Li-S batteries. A mathematical model is presented and the kinetic parameters of the electrochemical reactions of polysulfides are found. Sensitivity analyses of the mathematical model are performed on different parameters, including the effects of discharge current, electronic conductivity of the cathode, precipitation rate constants, sulfur content, exchange current densities and cathode thickness. The sensitivity of the model to variations of these parameters over a wide range of values is investigated. In particular, we show that the discharge voltage profile of Li-S at low discharge current rates typically contains two plateaus, while at high current rates, the first voltage plateau disappears. Furthermore, it is demonstrated that the performance of Li-S batteries is a function of the ability of the electrolyte to dissolve elemental sulfur; the undissolved portion of elemental sulfur cannot take part in the reduction reactions, thereby causing capacity loss. On the other hand, if the reduced polysulfides do not precipitate, the accumulation of the products in the electrolyte solutions results in high concentration overvoltage and prevents further electrochemical reduction. Moreover, the charge process is also simulated. In order to charge the battery completely, the reduced polysulfides must rapidly dissolve back to the electrolyte to take part in oxidation reactions.

The second part of thesis investigates the electrochemistry of the zinc anode in a zinc/$LiMn_2O_4$ aqueous battery. The possible electrochemical reactions on the anode are discussed in detail and a mathematical model is formulated accordingly, and the suitable kinetic parameters are also suggested. To the best of our knowledge, this is the first time that the reversible electrochemistry of zinc in a charge/discharge cycle is modeled. The

model is then evaluated with experimental data. The complicated deposition and dissolution of zinc, along with side reactions such as hydrogen evolution and zinc-water reactions, are modeled by considering the electrochemical and physical reactions of the adsorbed species on the surface of the electrode, including hydrogen and zinc hydroxide compounds.

Both models are based on the mass transfer theory governed by continuous diffusion equations with boundary conditions given by the dynamics of chemical/electrochemical reactions at the electrode-electrolyte interface. The details of the physicochemical processes in these two batteries are, however, different. For instance, in the Li-S battery, the dissolution of elemental sulfur and precipitation of lithium sulfides occur within the bulk of the electrolyte, and the electrochemical reactions of intermediate products ($Li_2S_{x\geq 2}$) at the interface are critical processes. On the other hand, in the ReHAB, the dynamics of interfacially adsorbed species on the zinc determine the battery behavior during charge and discharge cycles. In spite of the similarities and differences between the two systems, the models nevertheless give much insight into the working mechanisms of the two batteries.

Acknowledgements

I express my gratitude to my supervisor Prof. Pu Chen, who has been a good friend, excellent advisor, and with whom it has been a pleasure and privilege to work. I thank him for his excellent advice and donation of his time. My research was greatly improved by observing the high standards with which my supervisor conducts his own work.

I would like to express my gratitude to all members of my committee: professors Mark Pritzker, Nasser Lashgarian Azad and Nasser Mohieddin Abukhdeir. During this project, I also benefited from very enlightening discussions with Prof. Mark Pritzker. His excellent knowledge on electrochemistry guided me through my research, and I thank him. Prof. Nasser Lashgarian Azad and Prof. Nasser Mohieddin Abukhdeir have been great sources of insight that helped to improve this research and I thank them.

I express my sincere appreciation to Prof. Gillian Goward for agreeing to be the external examiner of my thesis.

I am also grateful to Doan, my friend, for the many helpful discussions we have had. He kindly carried out an excellent experiment for my research.

I also acknowledge all of my colleagues and friends at Waterloo who helped to make my period of study here more satisfying. They have been a constant source of encouragement, assistance, friendship and amusement.

I express my profound gratitude to Mary McPherson of the Writing Center. Thanks to her for being such a kindhearted person.

My special thanks goes to my family: my beloved parents, brothers and sisters, for their endless love and support, without which I should not have succeeded. I am forever indebted to them. Words cannot express how grateful I am to my parents for all the sacrifices they have made. A special thanks to Milad, my brother, for being a great support and encouragement in Canada during the past few years.

Last but not least, I am deeply grateful to have the support, encouragement and love of my forever friend Rabab Mashayekhi over the past few years.

Dedication

To my beloved parents.

Table of Contents

Author's Declaration ii

Abstract iii

Acknowledgements v

Dedication vi

List of Tables xi

List of Figures xiii

1 Introduction 1

1.1 Fundamental of batteries 2

1.2 Mathematical modeling of battery systems 4

1.3 Thesis summary and objectives 6

2 Model Development of Lithium-Sulfur Cells 8

2.1 Introduction 8

2.2 Fundamentals and operating principles 12

2.3 Model development 14

2.4 Governing equations 16
2.5 Summary of the assumptions and limits of the model 23

3 Results and Discussion **26**

3.1 Applied discharge current I_{app} 26
3.2 Conductivity of the cathode, σ 34
3.3 Rate constants for the precipitation reactions 37
3.4 Sulfur content 46
3.5 Thickness of the cathode 52
3.6 Charging the modeled cell and solubility product of precipitates 55

4 Introduction to Aqueous Li-Ion Batteries **59**

4.1 Large-scale energy storage batteries 59
4.2 Organic electrolytes benefits and challenging issues 62
4.3 Aqueous electrolytes 63
4.3.1 Aqueous electrolytes benefits 64
4.3.2 Aqueous electrolytes challenging issues 64
4.4 Hybrid aqueous batteries 70

5 Zinc Electrochemistry **72**

5.1 Thermodynamic stability 72
5.2 Kinetics of electrochemical reactions 78
5.2.1 Dissolution 78
5.2.2 Deposition 81
5.2.3 Hydrogen evolution 82

6 Zinc Anode in ReHAB **87**

6.1 Experimental . . . 88

6.1.1 Electrolyte, anode, and cathode preparation . . . 88

6.1.2 Electrochemical characterizations . . . 88

6.2 Results . . . 89

6.3 Modeling attempts . . . 94

6.3.1 Simplest scheme of reactions . . . 95

6.3.2 Second scheme including direct reactions of zinc and water . . . 96

7 Model Development of Zinc Half-Cell **99**

7.1 Heterogeneous reactions . . . 100

7.2 Homogeneous reactions . . . 103

7.3 Governing equations . . . 104

7.3.1 Governing equations in the bulk of the solution . . . 104

7.3.2 Dynamics of adsorption on the electrode surface . . . 106

7.3.3 Boundary conditions . . . 107

7.4 Summary of the assumptions and limits of the model . . . 108

7.5 Model simulations . . . 108

8 Summary and Future Works **120**

8.1 Summary of Li-S model . . . 120

8.2 Future work on Li-S model . . . 122

8.3 Summary and future work on zinc model . . . 124

8.4 Conclusion on modeling . . . 125

APPENDICES 126

A Parameters and Symbols 127

References 130

List of Tables

2.1 Assumed reactions in lithium-sulfur cell 15

2.2 Governing equations of the model of lithium-sulfur cell 17

2.3 Stoichiometric coefficients $s_{i,j}$ 19

2.4 Kinetic and thermodynamic properties, taken from Ref. [29] 23

2.5 Transport properties and reference concentrations, taken from Ref.[29] or calculated. 24

2.6 Separator and cathode parameters, taken from Ref. [29] 24

2.7 Parameters for precipitation reactions, taken from Ref. [29] or assumed. . . 25

4.1 Energy and power characteristics of different types of batteries [11]. 61

4.2 The cost of various energy storage systems [11]. 61

5.1 Zinc reactions in aqueous solutions and their equilibrium conditions [39, 56] 73

5.2 Characteristics of hydrogen evolution, metal dissolution and corrosion of Fe, Zn and Pb in the presence of a solution with $pH = 0$ containing 0.01 mol/lit of dissolved metal [39]. 85

7.1 Set of assumed reactions on the surface of zinc anode. 101

7.2 Set of assumed reactions in the bulk of the aqueous solution. 103

7.3 Diffusion Coefficients (D_i), taken from Ref. [56]. (*: assumed) 109
7.4 Equilibrium conditions and kinetic parameters of the homogeneous reactions [39] 109
7.5 Assumed initial values for adsorbed species 110
7.6 Initial values of species' concentrations 110
7.7 Kinetic parameters of the heterogeneous reactions 111

List of Figures

1.1 Schematic energy diagram of a cell [20]; (a) solid electrodes and liquid electrolyte, (b) solid electrolyte and liquid reactants. 3

1.2 Schematic of modeling tasks and the interaction between them. Modified from Ref. [40] 5

2.1 Comparison of energy density and power density of different energy storage systems [45] 9

2.2 Theoretical energy vs practical energy density of various batteries [44] . . . 9

2.3 Typical charge/discharge profile of Li-S cell (modified from Ref. [55]). . . . 13

2.4 Schematic of Li-S cell and summary of governing equations [18, 19] 18

3.1 The discharge plateau of a sulfur-based cell at different discharge current rates. First plateau vanishes due to low dissolution rate of elemental sulfur. 27

3.2 (a), (b), (c), (d), and (e) Normalized current, due to different electrochemical reactions, produced by the reduction of S, S_8^{2-}, S_6^{2-}, S_4^{2-} , and S_2^{2-}, respectively. (f) Average volume fraction of solid elemental sulfur, $\varepsilon_{8(s)}$, and $Li_2S_{(s)}$, $\varepsilon_{Li_2S_{(s)}}$, in the cathode during discharge. 29

3.3 Average species concentration in the cathode during discharge. Increasing the discharge rate, high polysulfides' concentrations decrease and low polysulfides' concentrations increase. 30

3.4 Volume fraction of $Li_2S_{(s)}$, $\varepsilon_{Li_2S_{(s)}}$ across the cell at different times of discharge with a current rate of 7 C. The interface of the separator and the cathode is located at $x = 9\ \mu m$. 32

3.5 The discharge profile of various curents. Taken from Ref. [41] 33

3.6 The discharge profile of various curents. Taken from Ref. [47] 33

3.7 The discharge plateaus of the sulfur-based cell with different conductivities of the cathode matrix for discharge current rates of 5 C and 1 C. 35

3.8 Volume fraction of $Li_2S_{(s)}$, $\varepsilon_{Li_2S_{(s)}}$ across the cell at different times of discharge for a discharge current rate of 5 C. The separator-cathode interface is located at $x = 9\ \mu m$. 35

3.9 Discharge voltage plateau for different rate constants at discharge current rates of 0.1 C. (a) to (e) In each case, only the mentioned rate constant differs from the initial assumptions. (f) Some other cases for comparison. In each set, $k_k = k_k^* \times b_k$, and b_k are equal to one in "set *", (1, 1, 20, 6, 1) in "set 1", (0.1, 1, 25, 8, 2.5) in "set 2", and (0.051, 1, 60, 16, 250) in "set 3". 38

3.10 Discharge voltage plateau for different rate constants at a discharge current rate of 1 C. (a) to (e) in each case, only the mentioned rate constant differs from the initial assumptions. (f) Discharge voltage plateau at high C rates for the case with a high solubility of sulfur. 40

3.11 Volume fraction of $Li_2S_{(s)}$, $\varepsilon_{Li_2S_{(s)}}$ across the cell at the end of a discharge with a discharge current rate of 0.1 C. The separator-cathode interface is located at $x = 9\ \mu m$. 45

3.12 Volume fraction of $Li_2S_{(s)}$ ($\varepsilon_{Li_2S_{(s)}}$) and $Li_2S_{2(s)}$ ($\varepsilon_{Li_2S_{2(s)}}$) across the cell at the end of a discharge with a discharge current rate of 0.1 C. 45

3.13 Discharge curves at different volume fraction of sulfur content and discharge current rates. 47

3.14 Discharge capacity percentage out of the total capacity for the cells with different sulfur contents and at various discharge rates. 47

3.15 Average volume fraction of precipitants across the cathode at the end of a discharge for different discharge currents. 50

3.16 Discharge capacity per unit surface area of the cathode for different sulfur contents and at various discharge rates. 50

3.17 (a) voltage profiles, and (b) Discharge capacity vs. cycle number of the Li-S cell with different sulfur/carbon ratios. Taken from Ref. [51] 51

3.18 Cycle performance of the sulfurcarbon sphere composites with 42 wt% and 51 wt% sulfur at the low current density of $40mAg^{-1}$. Taken from Ref. [53] 51

3.19 Discharge capacity percentage out of the total capacity for the cells with different cathode thicknesses at discharge rates of 2 C and 5 C. 54

3.20 Discharge capacity per unit surface area of the cathode with different cathode thicknesses, at discharge rates of 2 C and 5 C. 54

3.21 Decrease in voltage of the liquid phase at the end of cathode and at the surface of anode versus the cathode thickness for discharge rates of 2 C and 5 C at two specific times. 55

3.22 The cycle voltage plateau of Li-S cell at a current of $0.02C$, at different solubility of Li_2S. The cell is discharged completely first and the relaxed for 5 hours before being charge at constant current. At the end cell is left for 5 hours to relax to OCP. 56

3.23 Volume fraction of elemental sulfur and Li_2S, during cycle. 56

3.24 Concentration of species during cycle at $K_{Li_2S_{(s)}} = K^*_{Li_2S_{(s)}} \times 3 \times 10^7$. . . . 57

4.1 Comparison of several energy storage systems [11] 60

4.2 The intercalation potential of some electrode materials and the stability voltage window of an aqueous solution with $1 M Li_2SO_4$ at different pH values [33] 66

4.3 Schematic view of ReHAB. Taken from Ref. [52] 71

5.1 Potential-pH equilibrium for zinc-water system at $25°C$ [39, 56] 74

5.2 Theoretical conditions of corrosion, passivity and passivation of zinc, (a) for solutions free from CO_2, and (b) for solutions containing CO_2 [39] 76

5.3 Influence of pH on the corrosion of zinc [39] 76

5.4 Influence of pH on the solubility of zinc hydroxides, at $25°C$ [39] 77

5.5 Values of hydrogen exchange current density, $\log i_0$, on various metals in acid solutions [27]. 83

5.6 Corrosion of metals (Fe, Zn, Pb) with the evolution of hydrogen in the presence of a solution of $pH = 0$ containing 0.01 $mol/liter$ of dissolved metal [39]. 84

6.1 Polarization of zinc anode during charge and discharge of ReHAB with current rates of (a) 0.2C, (b) 0.2C, (c) 1C and (d) 4C. 90

6.2 Voltage of (a) cathode and (b) anode vs reference electrode during charge and discharge at current rate of 1C. 91

6.3 Measuring OCV of zinc anode vs reference electrode during charge and discharge in ReHAB. 92

6.4 Modeling Results (a) Voltage, (b) Fraction of surface area occupied by species, (c) pH of the solution. (d), (e), and (f) same data for another set of kinetic parameters 97

6.5 Modeling Results of second reaction scheme (a) Voltage, (b) Fraction of surface area occupied by species, (c) pH of the solution. 98

7.1 Schematic of the zinc-half-cell 104
7.2 Polarization of zinc at 0.02C. 112
7.3 pH of the solution in the vicinity of zinc electrode. 113
7.4 Fraction of adsorbed zinc ions on the electrode surface. 113
7.5 Fraction of zinc oxide and hydroxide on the electrode surface. 114
7.6 Polarization of zinc at 0.02C, for various kinetics of reaction 4. 116
7.7 Fraction of perfect sites Zn^* on zinc surface, at various kinetics of reaction 4 116
7.8 Polarization of zinc at 0.02C, when reaction 16 does not occur. 117
7.9 Polarization of zinc at 0.02C, when equilibrium constant of reaction 18 is increased by a factor of 10. 118
7.10 pH of the solution in the vicinity of zinc electrode, when equilibrium constant of reaction 18 is increased by a factor of 10. 118

Chapter 1

Introduction

In the past few centuries, humans have experienced a technological revolution that brings comfort to daily life. This revolution would not have been possible without advances in the energy supply, which still comes mainly from various kinds of combustion reactions. Recently, the cost of this kind of energy has brought deep concern: the emissions resulting from fuel consumption are driving climate change. Therefore, technological developments are facing the new challenge of reconsidering how to use energy in various devices. Batteries are considered the potential solution to the need for storing energy in various applications. They are currently used to power a diverse range of devices, from cellphones to cars. Moreover, sodium/sulfur battery technology is commercially available for large-scale storage.

Although batteries are fundamentally simple in concept, they have been extremely hard to improve. Indeed, progress in their development has been very slow compared to the advancements in other electronic areas. This lag becomes more surprising when considering that the first electrochemical battery was made by Alessandro Volta in 1800. In fact, we are very unlikely, at least in the near future, to find a single technology that can store electric energy efficiently and at low cost [11].

Historically, the term battery was first used by Benjamin Franklin to describe multiple Leyden jars by analogy to a battery of cannon. In the military, battery refers to weapons

functioning together, but a Leyden jar is a capacitor which stores static electricity between two electrodes on the inside and outside of a glass jar. In 1800, Alessandro Volta built the first electrochemical battery consisting of zinc and copper electrodes, known as the voltaic pile. However, he did not realize that voltage is due to chemical reactions; rather he thought that his cell was an endless source of energy.

In 1899, lead-acid batteries were used in a Belgian electric car that reached a speed of $30m/s$ [3]. In the same year, the only petrol-driven car was disqualified from participating in a car competition in Paris because of its high fuel consumption. Between 1900 and 1920, the numbers of electrical cars produced in the United States dropped significantly [3]. The lack of efficient batteries slowed down the development of electrical cars and many other portable devices.

1.1 Fundamental of batteries

In general, the structure of a cell consists of two electrodes with different chemical potential, connected by an ionically conductive electrolyte. The electrolyte can be a liquid or solid. Usually, solid electrolytes are used for liquid electrodes. They might be used for solid electrodes, but the solid-solid interfaces cause difficulties unless the solid electrodes are thin or the solid electrolytes are made of polymer [20]. When a battery is connected to an external device, since electrons cannot be transferred through electrolytes, they pass through an external circuit from more negative to more positive potential, and positive ions are transferred through the electrolyte. The batteries can be characterized into two types: primary batteries, which transform chemical energy into electrical energy in an irreversible way, and secondary batteries, in which the chemical-to-electrical energy transformation is reversible.

The important parameters in manufacturing batteries are the gravimetric and volumetric energy densities and power density. The theoretical energy density or amount of energy per mass (gravimetric), or volume (volumetric), depends on the chemistry of the

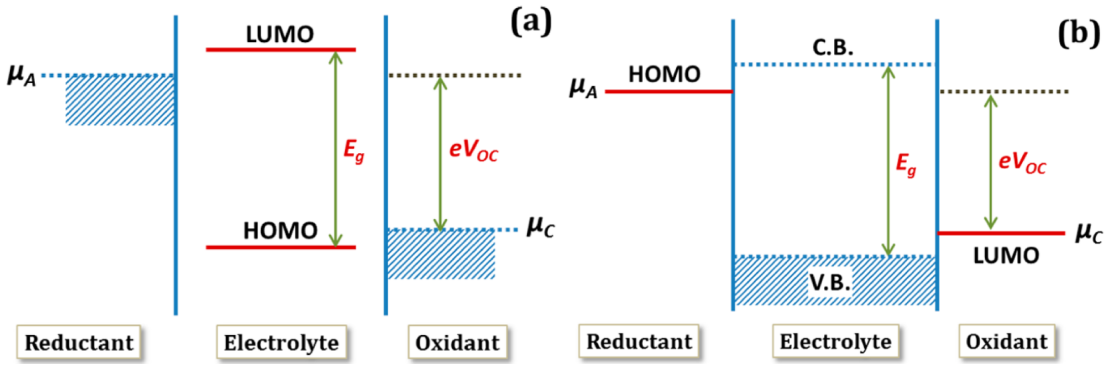

Figure 1.1: Schematic energy diagram of a cell [20]; (a) solid electrodes and liquid electrolyte, (b) solid electrolyte and liquid reactants.

battery. The chemistry of the system determines the cell voltage and capacity. Practically, the energy density depends on the operating current of the cell as well [20]. Moreover, irreversible side reactions between electrodes and electrolyte materials, decomposition of electrodes or electrolyte, and/or changes in the electrodes morphology during cycling, can lead to irreversible capacity loss. Cell engineering can improve the practical energy density so that it approaches the theoretical value and increases the cycle life by, for example, controlling the size and morphology of the active material particles. The power is also critically dependent on the chemistry of the battery although battery engineering can also partially improve the power [3, 20]. The energy density of a battery and its efficiency can be maximized by ensuring a large chemical potential difference between two electrodes, minimizing the mass or volume of the reactants per exchanged electron, and avoiding the consumption of electrolyte materials in the battery [3].

Batteries store energy within the electrode structure through charge transfer reactions. The open circuit potential of a cell is related to the difference between the electrochemical potential of the anode and cathode, i.e., $V_{oc} = (\mu_A - \mu_C)/e$. The energy gap, or window between a liquid electrolytes lowest unoccupied and highest occupied molecular orbitals (LUMO and HOMO, respectively) or the energy gap between the conduction and valence

bands of a solid electrolyte, limits the open circuit potential of the cell [20]. Figure 1.1 shows a schematic energy diagram of a cell with solid electrodes and liquid electrolyte or solid electrolyte and liquid or gaseous reactants. If LUMO is placed below , the electrolyte will be reduced unless a passivating solid-electrolyte interface (SEI) blocks the reaction. Likewise, if HOMO is above , the electrolyte will be oxidized unless a passivating SEI blocks the oxidization [20].

1.2 Mathematical modeling of battery systems

Designing an advanced battery system requires understanding of the mechanism of all its parts, including the anode, cathode and electrolyte. Mathematical models have proven to be powerful tools for clarifing, optimizing and designing various battery systems [40]. Figure 1.2 shows a schematic of modeling tasks and their interaction. For a given electrochemical system, one must identify the base material properties and physiochemical mechanism of the system. According to these identifications, a model can be developed and then verified using the experimental data. A successful simulation of the system can be efficiently formulated for optimization and design purposes [16, 40].

Different modeling methods, from empirical models to molecular/atomistic models, have been widely employed in battery research. Continuum models, initially developed by Newman et al. [38], are by far the most used in battery research [40]. These models capture the dynamics of species concentrations in electrolyte, electrolyte potential, solid-phase concentrations and solid-phase potential within porous electrodes. The continuum models are based on principles of mass and charge transport theory coupled with the thermodynamics and kinetics of electrochemical reactions. Generally, the kinetics of the electrochemical reactions are governed by the Butler-Volmer equation [38]. These types of models approximate the effect of the microstructure of the battery system using a few phenomenological parameters and empirical parameters, such as diffusion coefficents and effective conductivity[38, 16]. The mass and charge transport theory, based on mass and

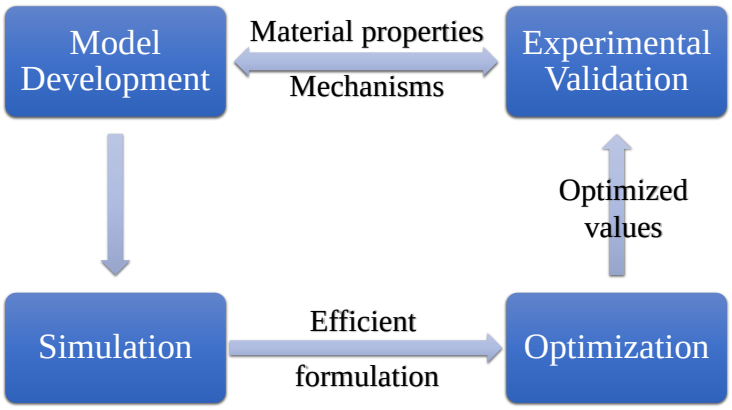

Figure 1.2: Schematic of modeling tasks and the interaction between them. Modified from Ref. [40]

charge conservation, is given by continuous partial differential equations which are typically coupled to ordinary differential equations of reaction kinetics based on conservation of charges.

This thesis employs the continuum model to study two battery systems: lithium-sulfur (Li-S) and rechargeable hybrid aqueous batteries (ReHAB). Despite all the physiochemical differences of these two battery systems, this work emphasises mainly the capabilities of the continuum model to describe different battery systems and provide detailed insights on their mechanisms and the effects of various physiochemical parameters on their performance.

Our continuum model of Li-S successfully describes the typical behaviour of these two batteries. Furthermore, the sensitivity analysis explains several reported features of Li-S batteries in the literature. The continuum model of a zinc half-cell in ReHAB also shows good agreement with our experimental results. To the best of our knowledge, this is the first theoretical study focusing on the low polarization and reversible electrochemistry of a zinc electrode. In the literature, typically, the deposition and dissolution of zinc are studied separately under conditions of high polarization when reactants are irreversible.

1.3 Thesis summary and objectives

The first part of the thesis employs the continuum model on Li-S batteries. An introduction to the Li-S batteries along with the details of model development are given in Chapter 2. Simulation and sensitivity analysis results are presented in Chapter 3 along with several experimental results from the literature are compared with the simulation results.

The second part of this thesis focuses on the electrochemistry of zinc anodes in ReHAB batteries. Again, a continuum model is used to investigate this system. An introduction to aqueous batteries and ReHAB is given in Chapter 4. Various proposed mechanisms for zinc electrochemistry are compared in Chapter 5. The experimental results of the polarization of zinc inside the ReHAB battery are presented and explained in Chapter 6 and, accordingly, a new mechanism for zinc electrochemistry is proposed in Chapter 7. A mathematical model based on the mechanism is implemented using continuum theory in this chapter, and the simulation results are presented. Last, a summary of both models and suggested future work is presented in Chapter 8.

The main scientific objectives of this work are as follows:

- To employ a continuum model on a Li-S cell.
- To find the kinetic parameters that describe the typical behaviour of Li-S batteries.
- To perform sensitivity analysis on the model parameters:

  to define ranges for model parameters,

  to possibly explain different features in experimental results,

  to find the model's limits in describing or predicting of system behaviour.
- To describe the electrochemistry of the zinc electrode in ReHAB.
- To employ the continuum model on a zinc half-cell.

- To find kinetic parameters that explain the behaviour of zinc electrodes in aqueous electrolytes.

Chapter 2

Model Development of Lithium-Sulfur Cells

2.1 Introduction

During the last two centuries, many electrode couples have been suggested. Among the most notable secondary batteries have included lead-acid and Ni-Cd batteries in the nineteenth and early twentieth centuries, and more recently, Ni-MH and lithium (Li) ion batteries (LIB) [3]. The LIBs have enabled the revolution in portable devices. However, high voltage LIBs are limited to $V \lesssim 5$ vs Li, because the organic liquid electrolytes used decompose at larger voltages [20]. Therefore, to increase the stored energy density, the cathode capacity must be increased significantly. For powering an electric vehicle, however, a cathode capacity beyond what LIBs can provide is needed. Thus, the use of inexpensive multi-electron redox reactants such as sulfur and oxygen has become attractive.

Figure 2.1 compares the gravimetric energy density and power density of different kinds of batteries and gasoline, while practical energy density vs theoretical energy density is illustrated in Figure 2.2. As shown in figures 2.1 and 2.2 lithium sulfur (Li-S) batteries can be a possible solution to the requirement for high energy and high power density batteries.

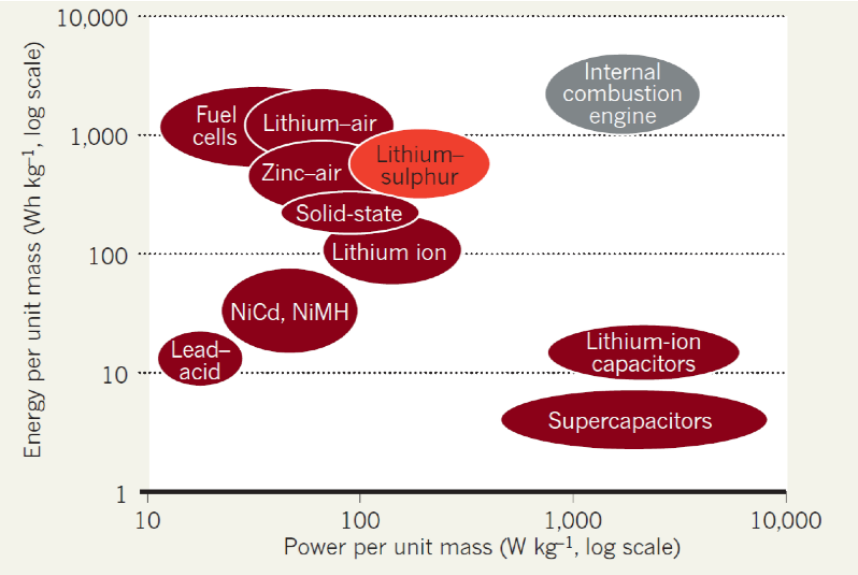

Figure 2.1: Comparison of energy density and power density of different energy storage systems [45]

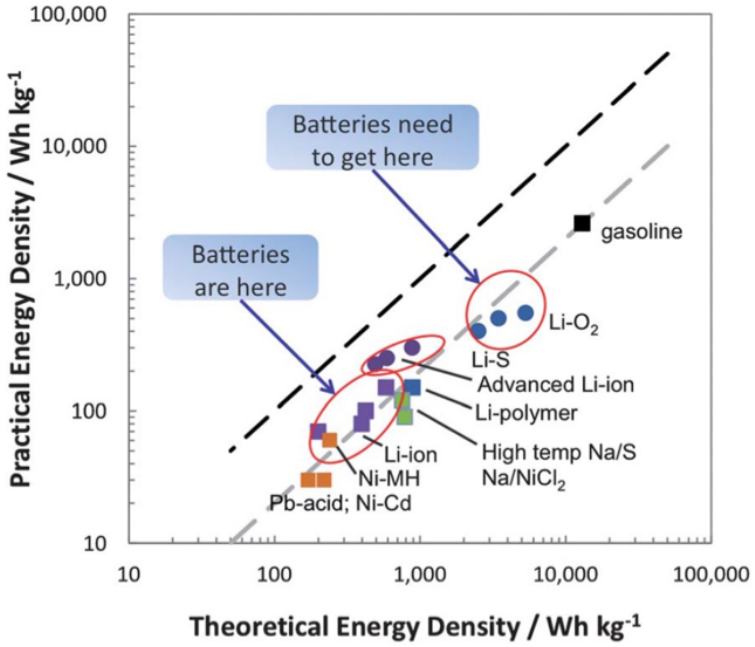

Figure 2.2: Theoretical energy vs practical energy density of various batteries [44]

The Li-S battery has a high theoretical specific energy (2,600 Wh/kg), and furthermore, sulfur is inexpensive, abundant and nontoxic. Over the past decade, extensive efforts have focused on developing a rechargeable Li-S battery [12]. However, no Li-S battery has been commercialized to date due to several unsolved problems. Because of the insulating nature of the Li-S battery discharge products, i.e., sulfur and lithium sulfides (Li_2S_2, Li_2S), a relatively large amount of conductive material must be added to the Li-S battery cathode to guarantee the utilization of the active material [55]. In addition, the dissolved polysulfides in the electrolyte diffuse through the separator to the lithium anode and react directly with the lithium. This reaction creates the so-called internal shuttle phenomenon, which causes passivation of active material and the self-discharge of the battery [12, 55, 24].

In fact, the behavior of sulfur batteries strongly depends on the morphology [53] and chemical properties of the cathode composite and electrolyte chosen [55]. Therefore, changing the additives in the cathode composite [55, 53, 22] or electrolyte [55, 23] leads to different discharge plateau shapes. Two flat discharge plateaus are observed in most cathode composites of sulfur and carbon materials [55]. In some cases of low loading of sulfur and specific electrolytes, three plateaus are also observed [4, 42]. In contrast, when cathode composites made of sulfur and polymer materials are used, only one decreasing plateau typically appears during discharge duo to the interaction between sulfur and polymer [22, 15]. Even within the two categories, significant changes occur in the details of the discharge plateau in different experiments.

Although a wide range of experimental strategies have attempted to tackle these problems, little theoretical attention has been paid to understanding the mechanism of the Li-S battery. Moreover, the behavior of the sulfur as the active material is very complicated and extremely sensitive to the different physical and chemical parameters involved in the preparation of the cathode composite or even during the assembly of a cell [6, 8-10]. For example, very complex reduction reactions of elemental sulfur S_8 occur during the discharge processes, and different polysulfide chains form in as-yet-undetermined ways [21, 4, 28]. Although the exact reduction reaction mechanism is not yet definitively determined, some models have been introduced to describe Li-S batteries. Y. V. Mikhaylik et al. [34] de-

veloped a mathematical model for the shuttle effect based on a two-stage reduction of sulfur. Specifically, S_8 is reduced to S_4^{2-} and S_4^{2-} is converted to S_2^{2-} and S^{2-}. The direct reduction of high-polysulfides on the surface of the lithium anode was also included in the model. The model produced a good understanding of the shuttle effect, thus providing evidence that self-discharge, overcharge and efficiency are strongly related to the shuttle effect.

Another mathematical model, introduced by K. Kumaresan et al. [29], considered five different stages for the reduction of sulfur to mathematically describe the discharge behavior of Li-S batteries. The model considers the dissolution and precipitation of sulfur and polysulfides into the electrolyte. Assuming that the electrochemical reactions in the system follow the Butler-Volmer equation, the equations governing the material balance of each individual species are solved in the model. The authors assumed many different parameters that must be determined by proper experiments, but in the absence of such experimental results, they provided educated guesses for most of the parameters. Nevertheless, their results corresponded well with a class of experimental results. However, implementing their model with the given parameters, one realizes that the reported parameters cause the simulation result to diverge.

In this part of study we employ the continuum model to the Li-S cell. The first goal is to find suitable kinetic parameters with which model governs the typical behaviour of Li-S cells. Afterwards, sensitivity analysis on important parameters is performed to exhibits the abilities of the model to explains observed behaviour of the Li-S cells in different experiments. However we do not focus on specific experiment. Despite the difficulty of doing so, investigating a specific system using the continuum model requires that each parameter be determined through an analysis of the results of experiments on that system, moreover, many of the parameters can not be measured directly in the experiments. Conversely, because of the system's complexity, different sets of parameters may result in the same model output. A sensitivity analysis of the model parameters will help elucidate the model and identify the actual Li-S cell behavior. The results of a sensitivity analysis would identify a range of values for each physical parameter and, more importantly, a set

of possible physical or chemical properties responsible for a specific behavior of the cell.

The aim of this work is not only to investigate the possible ranges of the physical parameters by performing a sensitivity analysis but also the model and thus clarify its abilities and limits. The results of the sensitivity analysis can be used to improve the mathematical model and can ultimately contribute to the development of commercial Li-S batteries. After finding the limits of the model, we propose modifications to improve the model's results, and more importantly, to shed light on the electrochemical mechanism of Li-S batteries.

2.2 Fundamentals and operating principles

Compared to the intercalation mechanism in conventional LIBs, the electrochemistry of the cathode in Li-S batteries is much more complex because of multistep reduction reactions of sulfur that occur during cell operation [24, 4, 1]. As mentioned earlier, the reduction mechanism, depends on the different physical and chemical factors such as the nature of the cathode composite, the morphology of the cathode and the composition of the electrolyte.

The exact details of the reduction mechanism of sulfur are not yet known beyond a doubt. However, given that the most stable form of elemental sulfur at standard temperature and pressure is the crown shape S_8 the overall electrochemical reaction for full discharge is:

$$S_8 + 16\ Li \rightleftharpoons 8\ Li_2S$$

Since elemental sulfur is an insulator (the electric conductivity of sulfur at room temperature is $5 \times 10^{-30} S\ cm^{-1}$), a large amount of conductive material must be added to the cathode composite [55]. at the same time, the reduction of sulfur particles during discharge is associated with a large volume expansion ($\sim 76\%$), which causes changes in the morphology of the cathode during cycling. Furthermore, to the best of our knowledge, no evidence of Li intercalation in sulfur particle has been reported in the literature. In

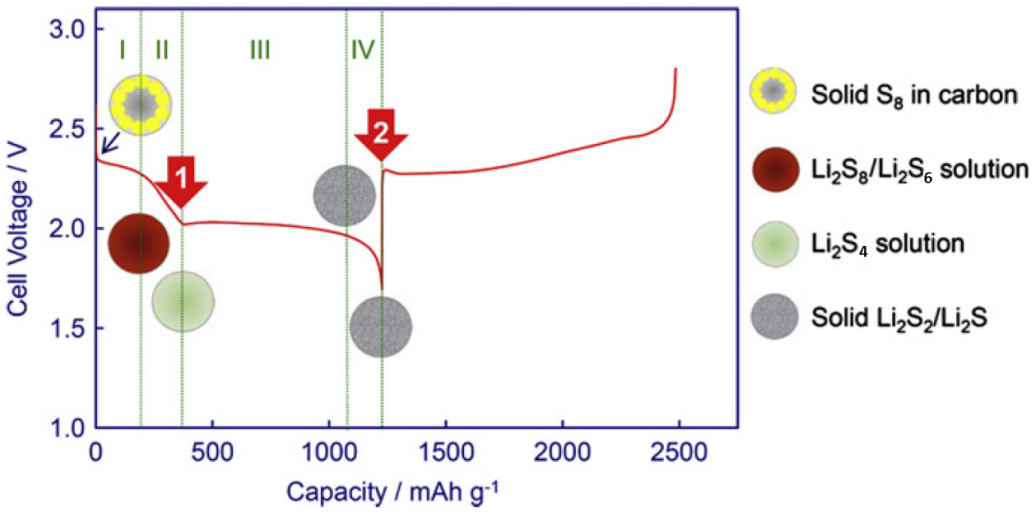

Figure 2.3: Typical charge/discharge profile of Li-S cell (modified from Ref. [55]).

fact, it is expected that the insulating nature of sulfur and large volume expansion of the reduced sulfur inhibit Li intercalation [55].

Experimental results show that sulfur is partially soluble in the liquid electrolyte [55, 24]. Thus elemental sulfur first dissolves in electrolyte and then undergoes a series of reduction reactions. The resulting high polysulfides, Li_2S_n $(n \geq 4)$ are soluble in electrolyte whereas the low polysulfides Li_2S_n $(n < 4)$ are not soluble and form a solid phase [55, 24].

In general, in sulfur-carbon cathode composite, two and occasionally three discharge voltage plateaus are observed during charge/discharge [24, 4]. A typical discharge-charge profile of Li-S cells is shown in Figure 2.3. Several mechanisms are suggested for reduction [55, 24, 21, 4, 28, 34, 29]; although they are different in detail, they are based on the following overall process. The first discharge plateau in region I (Figure 2.3), is associated with the reduction of elemental sulfur to soluble S_8^{2-} and then S_6^{2-}. In this region, solid elemental sulfur dissolves in the electrolyte and feeds the reactions. As elemental sulfur is entirely consumed at the end of region I, the system enters region II where voltage drops

with the formation of polysulfide S_4^{2-}. Region III is characterized by a larger plateau associated with the formation of low-ploysulfides S_2^{2-} and S^{2-}. At the end of discharge in region IV, the voltage more sharply decreases. The increase of the internal resistance due to coverage of active (conductive) cathode surface by non-conductive Li_2S_2 and Li_2S [55] and the solid-solid reduction of Li_2S_2 to Li_2S [24] are the proposed causes of the potential drop in region IV.

Two plateaus during charging are seen regularly [24]; however the transition between two plateaus is smooth with a large region where the voltage increases from first plateau to the second. Thus a well-defined phase transition point cannot be defined. The voltage difference between two plateaus is also typically smaller than the voltage difference during the discharge process. The discharge profile typically shows a well-known sharp trough, while the charge profile exhibits a small peak in the beginning of the process. In Figure 2.3, these points are shown as points 1 and 2, respectively.

Although recent extensive studies have focused on the mechanism of sulfur reduction [4, 53], this mechanism is still a subject of debate. In this study, we start with the simple, but well-detailed model proposed by K. Kumaresan et al [29].

2.3 Model development

A list of the assumed reactions in the lithium-sulfur cell is given in Table 2.1. The reactions in the cell include Li metal oxidization at the anode surface during discharge [29]:

$$Li \rightleftharpoons Li^+ + e^- \tag{2.1}$$

During discharge, the elemental sulfur, which is initially in the solid phase, dissolves in the electrolyte and then goes through the following electrochemical reactions [29]:

$$\frac{1}{2}\ S_{8(l)} + e^- \rightleftharpoons \frac{1}{2}\ S_8^{2-} \tag{2.2}$$

$$\frac{3}{2}\ S_8 + e^- \rightleftharpoons 2\ S_6^{2-} \tag{2.3}$$

Table 2.1: Assumed reactions in lithium-sulfur cell

	Reaction		Anode	Separator	Cathode
Electrochemical reactions	$Li \rightleftharpoons Li^+ + e^-$	(1)	•		
	$\frac{1}{2} S_{8(l)} + e^- \rightleftharpoons \frac{1}{2} S_8^{2-}$	(2)			•
	$\frac{3}{2} S_8^{2-} + e^- \rightleftharpoons 2\, S_6^{2-}$	(3)			•
	$S_6^{2-} + e^- \rightleftharpoons \frac{3}{2} S_4^{2-}$	(4)			•
	$\frac{1}{2} S_4^{2-} + e^- \rightleftharpoons S_2^{2-}$	(5)			•
	$\frac{1}{2} S_2^{2-} + e^- \rightleftharpoons S^{2-}$	(6)			•
Precipitation / dissolution	$S_{8(s)} \rightleftharpoons S_{8(l)}$	(7)	•	•	•
	$2\, Li^+ + S_8^{2-} \rightleftharpoons Li_2S_{8(s)}$	(8)	•	•	•
	$2\, Li^+ + S_4^{2-} \rightleftharpoons Li_2S_{4(s)}$	(9)	•	•	•
	$2\, Li^+ + S_2^{2-} \rightleftharpoons Li_2S_{2(s)}$	(10)	•	•	•
	$2\, Li^+ + S^{2-} \rightleftharpoons Li_2S_{(s)}$	(11)	•	•	•

$$S_6^{2-} + e^- \rightleftharpoons \frac{3}{2}\, S_4^{2-} \tag{2.4}$$

$$\frac{1}{2}\, S_4^{2-} + e^- \rightleftharpoons S_2^{2-} \tag{2.5}$$

$$\frac{1}{2}\, S_2^{2-} + e^- \rightleftharpoons S^{2-} \tag{2.6}$$

As dissolved elemental sulfur $S_{8(l)}$ is consumed during discharge, its concentration in electrolyte drops below the solubility limit; consequently, solid elemental sulfur $S_{8(s)}$ dissolves in the electrolyte:

$$S_{8(s)} \rightleftharpoons S_{8(l)} \tag{2.7}$$

An increase in the concentration of the lithium and sulfide ions leads to the precipitation

reactions. Thus, the following precipitation/dissolution reactions also occur:

$$2\ Li^+ + S_8^{2-} \rightleftharpoons Li_2S_{8(s)} \tag{2.8}$$

$$2\ Li^+ + S_4^{2-} \rightleftharpoons Li_2S_{4(s)} \tag{2.9}$$

$$2\ Li^+ + S_2^{2-} \rightleftharpoons Li_2S_{2(s)} \tag{2.10}$$

$$2\ Li^+ + S^{2-} \rightleftharpoons Li_2S_{(s)} \tag{2.11}$$

2.4 Governing equations

The schematic view of the Li-S cell and the summary of governing equations are listed in Figure 2.4 and Table 2.2. The anode is assumed to be a metallic lithium foil, while the cathode is a porous carbon-sulfur composite. In a porous medium, the governing equation for the material balance of an individual species is [26, 38]

$$\frac{\partial \epsilon C_i}{\partial t} = -\nabla . N_i + r_i - R_i \tag{2.12}$$

where ε represents the pore volume fraction of the porous electrode or separator, C_i is the concentration of Li^+, $S_{8(l)}$, S_8^{2-}, S_6^{2-}, S_4^{2-}, S_2^{2-}, and S^{2-}, while the anion of the lithium salt is denoted as A^-. In a dilute electrolyte solution within the pores, the flux N_i of the species i is attributed to diffusion and migration:

$$\frac{N_i}{\epsilon} = -D_i \nabla C_i - z_i \frac{D_i}{RT} F C_i \nabla \varphi_l \tag{2.13}$$

The diffusion coefficient D_i for species i is corrected based on Bruggeman's expression for porosity and tortuosity: $D_i = D_{i,0}\varepsilon^b$ and $b = 0.5$ [26], where $D_{i,0}$ is the diffusion coefficient in the bulk medium. z_i is the charge number of species i and φ_l is the liquid phase potential.

The rate of production/consumption of species i due to the all electrochemical reactions can be written in the form

$$r_i = a \sum_j \frac{s_{ij} i_j}{n_j F} \tag{2.14}$$

Table 2.2: Governing equations of the model of lithium-sulfur cell

process	Governing equation
Material balance of an individual species:	$\frac{\partial\, \varepsilon C_i}{\partial t} = -\nabla \cdot N_i + r_i - R_i$
Individual species flux:	$\frac{N_i}{\varepsilon} = -D_i\, \nabla C_i - z_i \frac{D_i}{RT} F C_i\, \nabla \varphi_l$
Bruggeman's expression:	$D_i = D_{i,0}\varepsilon^b$
The rate of production/consumption of species *i* due to the electrochemical reactions:	$r_i = a \sum_j \frac{s_{ij}\, i_j}{n_j F}$
Butler-Volmer equation:	$i_j = i_{0,j\,ref}\left\{\prod_i \left(\frac{C_i}{C_{i,ref}}\right)^{P_{i,j}} exp\left(\frac{\alpha_{aj} F}{RT}\eta_j\right) - \prod_i \left(\frac{C_i}{C_{i,ref}}\right)^{q_{i,j}} exp\left(-\frac{\alpha_{cj} F}{RT}\eta_j\right)\right\}$
	$p_{i,j} = s_{ij}$: anodic species / $q_{i,j} = -s_{ij}$: cathodic species
The evolution of specific surface area of the cathode:	$a = a_0 \left(\frac{\varepsilon}{\varepsilon_{initial}}\right)^{\xi}$
Overpotential for the reaction *j*:	$\eta_j = \varphi_s - \varphi_l - U_{j,ref}$
	$U_{j,ref} = U_j^{\theta} - \frac{RT}{n_j F} \sum_i s_{i,j}\, ln\left[\frac{C_{i,ref}}{1000}\right]$
The liquid phase current density:	$i_l = F \sum_i z_i N_i$
The solid phase current density:	$i_s = -\sigma \nabla \varphi_s$
Charge transfer at the liquid/solid interface:	$\nabla \cdot i_l = a \sum_j i_j$
	$\nabla \cdot i_s + \nabla \cdot i_l = 0$
The rate of consumption or production of species *i* due to precipitation/dissolution:	$R_i = \sum_k \gamma_{i,k} R'_k$
	$R'_k = k_k \varepsilon_k \left(\prod_i C_i^{\gamma_{i,k}} - K_{sp,k}\right)$
The porosity variation with time:	$\frac{\partial \varepsilon}{\partial t} = -\sum_k \tilde{V}_k R'_k$
The volume fraction of the precipitate, *k:*	$\frac{\partial \varepsilon_k}{\partial t} = \tilde{V}_k R'_k$
Boundary conditions at the interface of the cathode and the current collector:	$N_i = 0$
	$i_s = I_{app}$
	$i_l = 0$
Boundary conditions at the cathode-separator interface:	$N_{i,seperator} = N_{i,cathode}$
	$i_{l,seperator} = i_{l,cathode} = I_{app}$
	$i_s = 0$
Boundary conditions at the surface of anode:	$\varphi_s = 0$
	$N_i = 0$
	$N_1 = i_1/F$
	$i_l = FN_1$

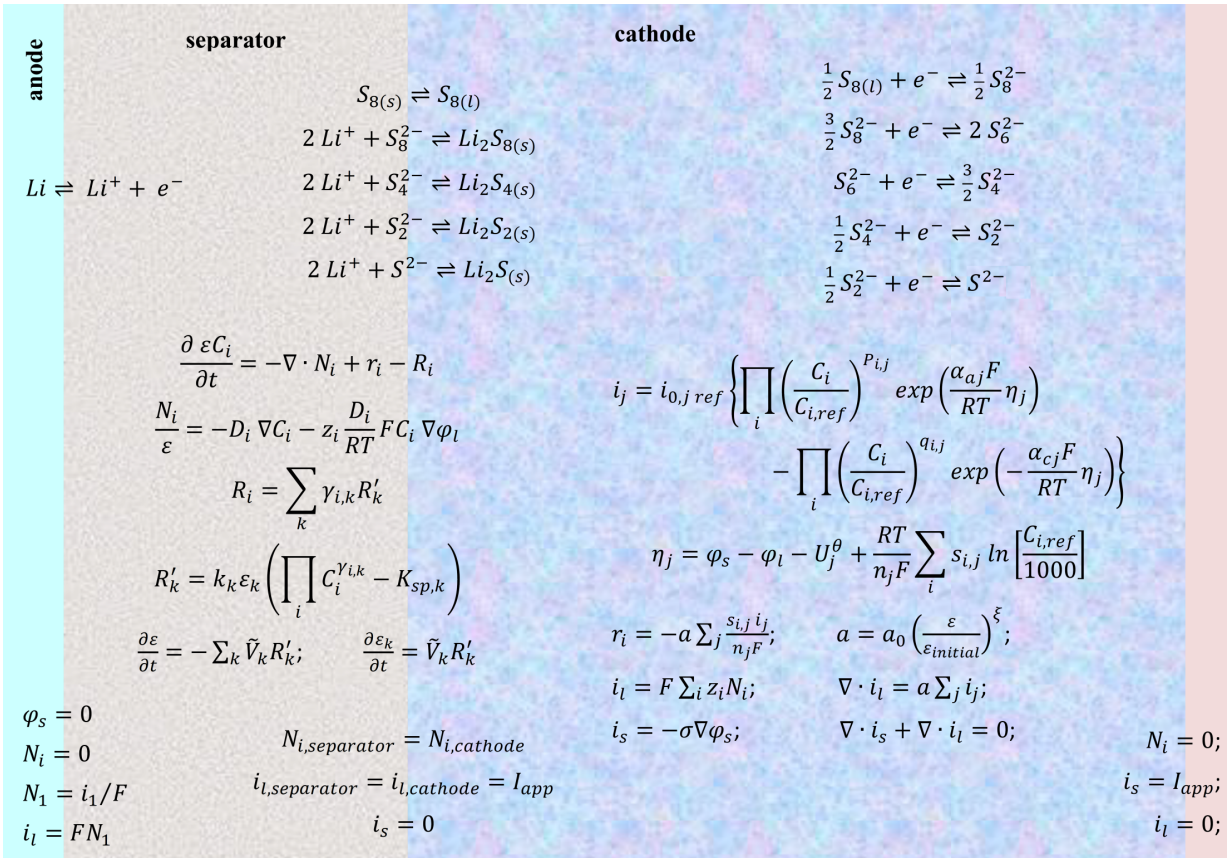

Figure 2.4: Schematic of Li-S cell and summary of governing equations [18, 19]

where the specific surface area a of the porous cathode is the area of the solid-liquid interface per unit volume of the porous cathode. The stoichiometric coefficients s_{ij} are given in Table 2.3. Here, the number of electrons n_j transferred in each electrochemical reaction is normalized to 1. The specific surface area of the cathode varies due to the precipitation/dissolution of the various lithium sulfide species and is assumed to be governed by the empirical expression:

$$a = a_0\left(\frac{\varepsilon}{\epsilon_{initial}}\right)^\xi \tag{2.15}$$

where the empirical parameter ξ is assigned a value of 1.5 [38].

The Butler-Volmer equation yields the current density due to each electrochemical

Table 2.3: Stoichiometric coefficients $s_{i,j}$

S_{ij}	Reactions given by Equation (j)					
Species (i)	1	2	3	4	5	6
Li^+	-1	0	0	0	0	0
$S_{8(l)}$	0	-1/2	0	0	0	0
S_8^{2-}	0	1/2	-3/2	0	0	0
S_6^{2-}	0	0	2	-1	0	0
S_4^{2-}	0	0	0	3/2	-1/2	0
S_2^{2-}	0	0	0	0	1	-1/2
S^{2-}	0	0	0	0	0	1
A^-	0	0	0	0	0	0

reaction [26, 38, 46]:

$$i_j = i_{0,j\ ref}\Big\{\prod_i \big(\frac{C_i}{C_{i,ref}}\big)^{p_{i,j}} \exp\big(\frac{\alpha_{aj}F}{RT}\eta_j\big) - \prod_i \big(\frac{C_i}{C_{i,ref}}\big)^{q_{i,j}} \exp\big(\frac{-\alpha_{cj}F}{RT}\eta_j\big)\Big\} \tag{2.16}$$

where the overpotential for the reaction j is

$$\eta_j = \varphi_s - \varphi_l - U_{j,ref} \tag{2.17}$$

The terms $p_{i,j} = s_{ij}$ refer to anodic species and $q_{i,j} = -s_{ij}$ refer to cathodic species. The open-circuit potential for reaction j at the reference concentrations $C_{i,ref}$ of species i is given by (when $C_{i,ref}$ is in mol/m^3 units)

$$U_{j,ref} = U_j^{\theta} - \frac{RT}{n_j F}\sum_i s_{i,j} \ln\big[\frac{C_{i,ref}}{1000}\big] \tag{2.18}$$

The liquid phase current density is given by

$$i_l = F\sum_i z_i N_i \tag{2.19}$$

The solid phase current density follows Ohm's law

$$i_s = -\sigma\nabla\varphi_s \tag{2.20}$$

Because the charge can enter or leave the liquid phase only by the electrochemical reactions, the following equation applies at the liquid-solid interface:

$$\nabla \cdot i_l = a \sum_j i_j \tag{2.21}$$

while charge conservation requires

$$\nabla \cdot i_s + \nabla \cdot i_l = 0 \tag{2.22}$$

The rate of consumption or production of species i due to precipitation/dissolution is related to the rate of precipitation/dissolution reaction k by

$$R_i = \sum_k \gamma_{i,k} R_k^{'} \tag{2.23}$$

where the rate of precipitation of solid species $k(S_{8(s)},\ Li_2S_{8(s)},\ Li_2S_{4(s)},\ Li_2S_{2(s)},\ Li_2S_{(s)})$ is assumed to be governed by the following kinetic equation:

$$R_k^{'} = k_k \varepsilon_k \big(\prod_i C_i^{\gamma_{i,k}} - K_{sp,k} \big) \tag{2.24}$$

$\gamma_{i,k}$ is the number of moles of ionic species i in solid species k and k_k is a rate constant. In the above equation, supersaturation has been taken into account through the solubility product $K_{sp,k}$. When the species concentration is below (/above) its saturation point, the solid phase dissolves in the electrolyte (/precipitates). Normally, the beginning of a precipitation reaction is associated with a slow nucleation process. At the beginning of the discharge, no solid phase of lithium polysulfides exist in the cathode. When the electrolyte becomes supersaturated for a given sulfide, the corresponding precipitation begins by nucleation during which a few precipitate nuclei are formed at the active sites in the porous medium. Subsequently, more precipitation occurs at the interface of the nuclei and the electrolyte. Therefore, at the start of the precipitation process, the precipitation rate depends on both the number of active sites (nuclei) and the interfacial area between nuclei and electrolyte. The interfacial area for a precipitate is assumed to be proportional to its volume fraction [29].

The volume fraction of the precipitate k depends on time as follows:

$$\frac{\partial \varepsilon_k}{\partial t} = \widetilde{V}_k R_k^{'} \tag{2.25}$$

where $\widetilde{V}_k$ is the partial molar volume of precipitate k. Therefore, the porosity variation with time is

$$\frac{\partial \varepsilon}{\partial t} = -\sum_k \widetilde{V}_k R_k^{'} \tag{2.26}$$

The boundary conditions (BCs) of the model are as follows. At the interface $x = L$ of the cathode and the current collector the flux of each species is zero due to the presence of the current collector:

$$N_i = 0 \tag{2.27a}$$

and therefore

$$i_s = I_{app} \tag{2.27b}$$

$$i_l = 0 \tag{2.27c}$$

At the cathode-separator interface, $x = L_s$, the flux of each species must be continuous:

$$N_{i,separator} = N_{i,cathode} \tag{2.28a}$$

Since the separator must be made of an insulator, all the current density is carried by liquid phase only:

$$i_{l,separator} = i_{l,cathode} = I_{app} \tag{2.28b}$$

$$i_s = 0 \tag{2.28c}$$

At the surface $x = 0$ of the anode, the lithium anode is assumed to be the reference point for the potential:

$$\varphi_s = 0 \tag{2.29a}$$

The flux of all species except Li^+ must be zero, i.e.,

$$N_i = 0 \tag{2.29b}$$

The flux boundary for Li^+ can be written as

$$N_1 = i_1/F \tag{2.29c}$$

Since only ions can carry the current at this point, the liquid phase current is

$$i_l = FN_1 \tag{2.29d}$$

The governing equations are solved numerically using COMSOL Multiphysics software. The parameters used in this model are given in Tables 2.4-2.7.

The normalized current [18, 19] due to electrochemical reaction j at the cathode is defined by the following expression and in this study to describe the system's kinetics:

$$I_j^N = \frac{1}{I_{app}} \int_{x=L_s}^{x=L} a\ i_j\ dx \tag{2.30}$$

where $\sum_{j=2}^{6} I_j^N = 1$. In other words, I_j^N represents the overall contribution of the electrochemical reaction j in producing the discharge current at a given time. In the ideal case of utilizing the entire capacity of sulfur, the normalized discharge currents satisfy the following relations:

$$\frac{1}{T_{DC}} \int_{t=0} I_j^N dt = C_j^d \tag{2.31a}$$

$$\{C_2^d, \ldots, C_6^d\} = \{\frac{1}{8}, \frac{1}{24}, \frac{1}{12}, \frac{1}{4}, \frac{1}{2}\} \tag{2.31b}$$

where T_{DC} is the total time of an ideal complete discharge and C_j^d is the contribution of reaction j to the total capacity.

Table 2.4: Kinetic and thermodynamic properties, taken from Ref. [29]

Reaction (j)	$i^*_{0,j\,ref}\ (A/m^2)$	α^*_{aj}	α^*_{cj}	n_j	U^θ_j
1	0.394	0.5	0.5	1	0.0
2	1.9719	0.5	0.5	1	2.39
3	0.019719	0.5	0.5	1	2.37
4	0.019719	0.5	0.5	1	2.24
5	1.972×10^{-4}	0.5	0.5	1	2.04
6	1.972×10^{-7}	0.5	0.5	1	2.01

2.5 Summary of the assumptions and limits of the model

In this model we ignored the thermal effects on the system. Temperature is assumed to be uniform and constant in the cell. We have also ignored the mechanical stresses in the solid phase. Assuming a coin cell geometry, the model is presented in one dimension since the thickness of a coin cell is much smaller than its radius.

Because eight different type of species are assumed to be dissolved in the electrolyte, concentrated solution theory is not applied; instead we employ the dilute solution theory in the Li-S model. Furthermore, it is assumed that the electrolyte does not participate in any side reaction, and also shuttle effect is ignored.

Table 2.5: Transport properties and reference concentrations, taken from Ref.[29] or calculated.

Species (i)	z_i	$D_{i0}^{*}\ (m^2/s)$	$C_{i,ref}^{*}\ (mol/m^3)$
Li^+	+1	1×10^{-10}	1001.08 *
$S_{8(l)}$	0	10×10^{-10}	19.0
S_8^{2-}	-2	6×10^{-10}	0.1832 *
S_6^{2-}	-2	6×10^{-10}	0.3351 *
S_4^{2-}	-2	1×10^{-10}	0.02146 *
S_2^{2-}	-2	1×10^{-10}	5.999×10^{-7} *
S^{2-}	-2	1×10^{-10}	9.94×10^{-10} *
A^-	-1	4×10^{-10}	1000

*: calculated based on OCPs.

Table 2.6: Separator and cathode parameters, taken from Ref. [29]

Parameter	Separator	Cathode
Thickness (m)	9×10^{-6}	41×10^{-6}
$\boldsymbol{\varepsilon_{initial}}$	0.37	0.778
$\boldsymbol{\varepsilon_{S_{8(s)},initial}}$	1×10^{-12}	0.160
$\boldsymbol{\varepsilon_{Li_2S_{8(s)},initial}}$	1×10^{-6}	1×10^{-6}
$\boldsymbol{\varepsilon_{Li_2S_{4(s)},initial}}$	1×10^{-6}	1×10^{-6}
$\boldsymbol{\varepsilon_{Li_2S_{2(s)},initial}}$	1×10^{-6}	1×10^{-6}
$\boldsymbol{\varepsilon_{Li_2S_{(s)},initial}}$	1×10^{-7}	1×10^{-7}
$\boldsymbol{a_0}$	-	132,762

Table 2.7: Parameters for precipitation reactions, taken from Ref. [29] or assumed.

Precipitate (k)	Rate constant (k_k^*)	Solubility product (K_k^*)	Molar volume ($\tilde{V}_k$ (m^3/mol))
$S_{8(s)}$	$1.0\ s^{-1}$	$19.0\ mol\ m^{-3}$	1.239×10^{-4}
$Li_2S_{8(s)}$	$1 \times 10^{-11}\ m^6 mol^2 S^{-1}$ *	$183400\ mol^3\ m^{-9}$ *	1.361×10^{-4}
$Li_2S_{4(s)}$	$9.98 \times 10^{-12}\ m^6 mol^2 S^{-1}$ *	$21480\ mol^3\ m^{-9}$ *	7.415×10^{-5}
$Li_2S_{2(s)}$	$9.98 \times 10^{-9}\ m^6 mol^2 S^{-1}$ *	$0.6006\ mol^3\ m^{-9}$ *	4.317×10^{-5}
$Li_2S_{(s)}$	$6.875 \times 10^{-5}\ m^6 mol^2 S^{-1}$ *	$9.95 \times 10^{-4}\ mol^3\ m^{-9}$ *	2.768×10^{-5}

*: assumed.

Chapter 3

Results and Discussion

The result of the model is presented in this chapter. Model exhibits the typical discharge voltage plateaus observed in experiment. The physiochemical process of the cell is discussed in detail. Furthermore sensitivity analysis are performed on following important parameters of the model: applied discharge current, conductivity of the cathode, rate constant for the precipitation reactions, sulfur content, and the thickness of the cathode. A range of values is assumed for each parameter. This range is not bounded by a range of physical values. The goal is to determine the behavior of the model system with respect to different situations and also to find a range for the parameters which are feasible for the Li-S cells. However, the functionality of the model with respect to these parameters was found not to be linear. Instead, we must investigate the effect of each parameters on the model while keeping the other parameters constant.

3.1 Applied discharge current I_{app}

One of the important goals in battery research is to widen the discharge current operation range of batteries; for example, a particularly high current rate is required for electric vehicles. Moreover, the discharge voltage plateau of a battery and its cyclability are strongly

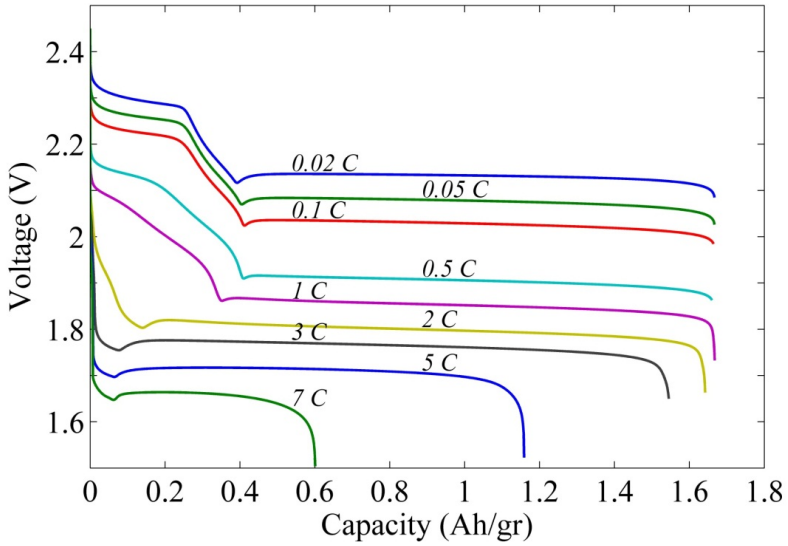

Figure 3.1: The discharge plateau of a sulfur-based cell at different discharge current rates. First plateau vanishes due to low dissolution rate of elemental sulfur.

dependent on the current rate during operation. Therefore, the response of the model to a range of applied currents must be investigated.

Figure 3.1 presents the discharge voltage plateaus. At low applied discharge currents of 0.02 C, 0.05 C and 0.1 C, two voltage plateaus are very evident. Moreover the discharge curves are quite similar, except for a decrease in potential at any given state of charge. This similarity suggests that the kinetics of the chemical reactions are similar at these rates of discharge. Because the decrease in the potential due to the resistivity of the cathode matrix and electrolyte is very small ($< 10^{-4}\ V$) compared to the total decrease in potential, one may conclude that the kinetics of the chemical reactions causes the decrease. In other words, the decrease is due to polarization at the surface of the anode and cathode. The Taylor expansion of the Butler-Volmer equation (Equation 2.16) to the first order describes that the overpotential and current are proportional at low current rates, i.e., $\Delta i \propto \Delta V$ and thus well approximates the observed plateaus in the first three discharge currents.

The first plateau starts to deform at the discharge rate of 0.05 C, as the speed of dissolution of elemental sulfur into the electrolyte is too slow to maintain a constant concentration of dissolved sulfur. The slow dissolving rate of sulfur is the main reason for the capacity loss, which starts at 2 C. Figure 3.2 provides more details of the reactions kinetics of the Li-S system.

The averaged concentration of the sulfide species over the cathode volume is presented in Figure 3.3. Because the graphs of normalized current for the cases $I_{app} = 0.1\ C$ and 0.5 C are similar to the case of 0.02 C, they are not shown in Figure 3.2, whereas the concentration of the sulfide species in these cases are shown (dotted lines) to illustrate the difference in the second part of the discharge. As the discharge current rate increases to 0.1 C, the concentration of the high sulfides ($S_{8(l)}$, S_8^{2+}, and S_6^{2+}) decreases more during the second part than in the first part because more material is used in the reaction. Thus, a higher concentration of the low sulfides (S_4^{2+}, S_2^{2+}, and S^{2+}) forms before the rate of the low-sulfide reactions becomes sufficiently high and the precipitation of Li_2S begins. This sequence of events causes a small shift in the sharp trough between the two stages. The shift in precipitation toward the right occurs even for a discharge current rate of 0.5 C, for which the trough starts to shift because the low-sulfide reaction begins relatively sooner. The relatively fast dissolution of sulfur into the electrolyte maintains a constant sulfur concentration during the first stage, and therefore, a constant reaction rate. The reduction of S_8^{2-} occurs simultaneously at a constant rate because the reference voltage is similar. When the solid sulfur in the system is fully consumed, the concentration of sulfur decreases suddenly (in the related time scale), as does the related current. At this point, the second reaction reaches a sharp peak and quickly reduces almost all of the S_8^{2-}. The reduction of S_6^{2-} becomes the dominant reaction in the system, leading to the production of the lower sulfides. As a result, the concentration of the low sulfides increases and further reaction requires a higher polarization at the cathode surface. The potential of the cell consequently decreases to a local minimum. At the point at which Li_2S starts to precipitate, the concentration of S^{2-} decreases, causing a sharp increase in rate of the last two reactions (Equations 2.5 and 2.6). Interestingly, because the S_4^{2-} concentration

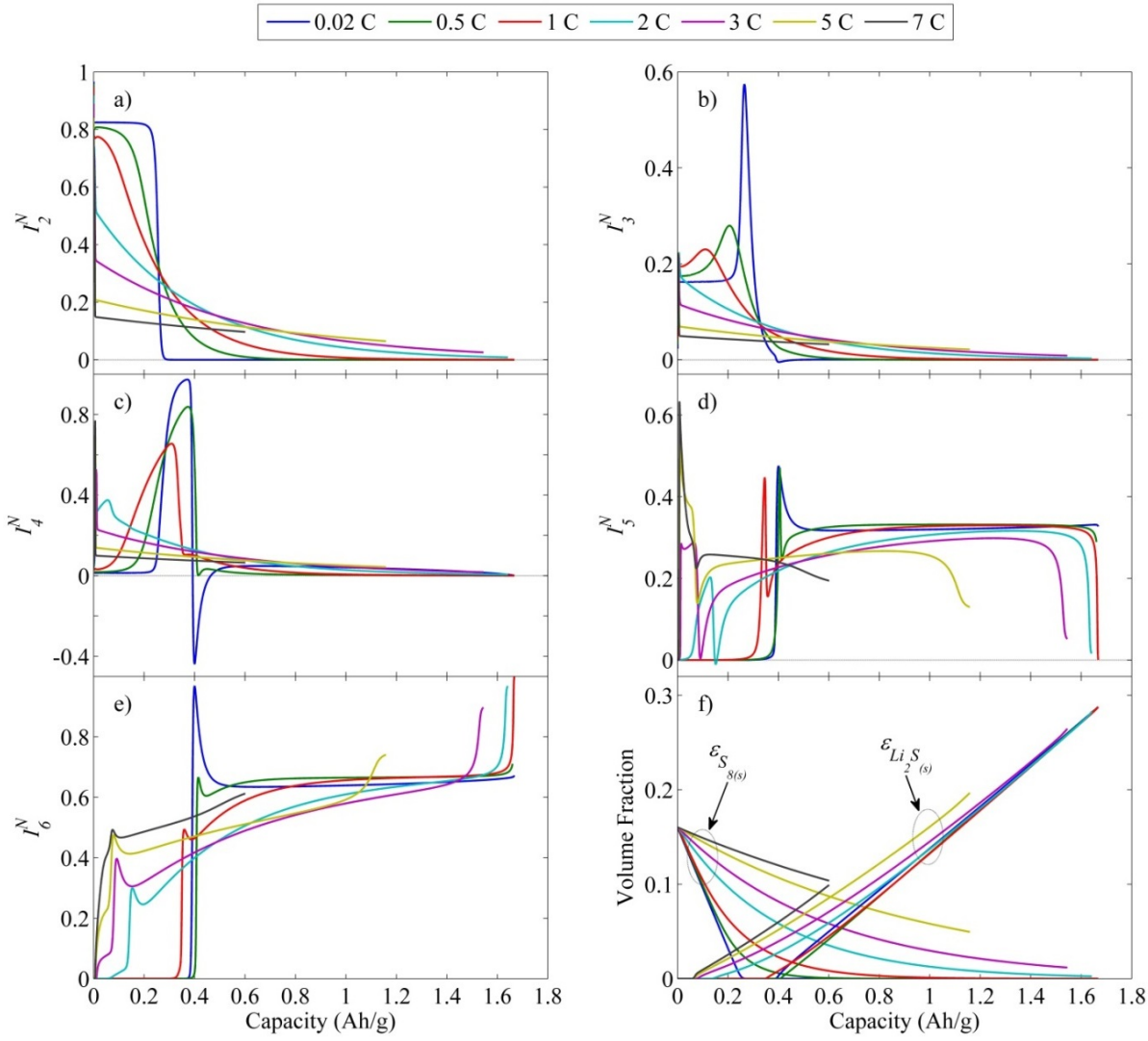

Figure 3.2: (a), (b), (c), (d), and (e) Normalized current, due to different electrochemical reactions, produced by the reduction of S, S_8^{2-}, S_6^{2-}, S_4^{2-}, and S_2^{2-}, respectively. (f) Average volume fraction of solid elemental sulfur, $\varepsilon_{8(s)}$, and $Li_2S_{(s)}$, $\varepsilon_{Li_2S_{(s)}}$, in the cathode during discharge.

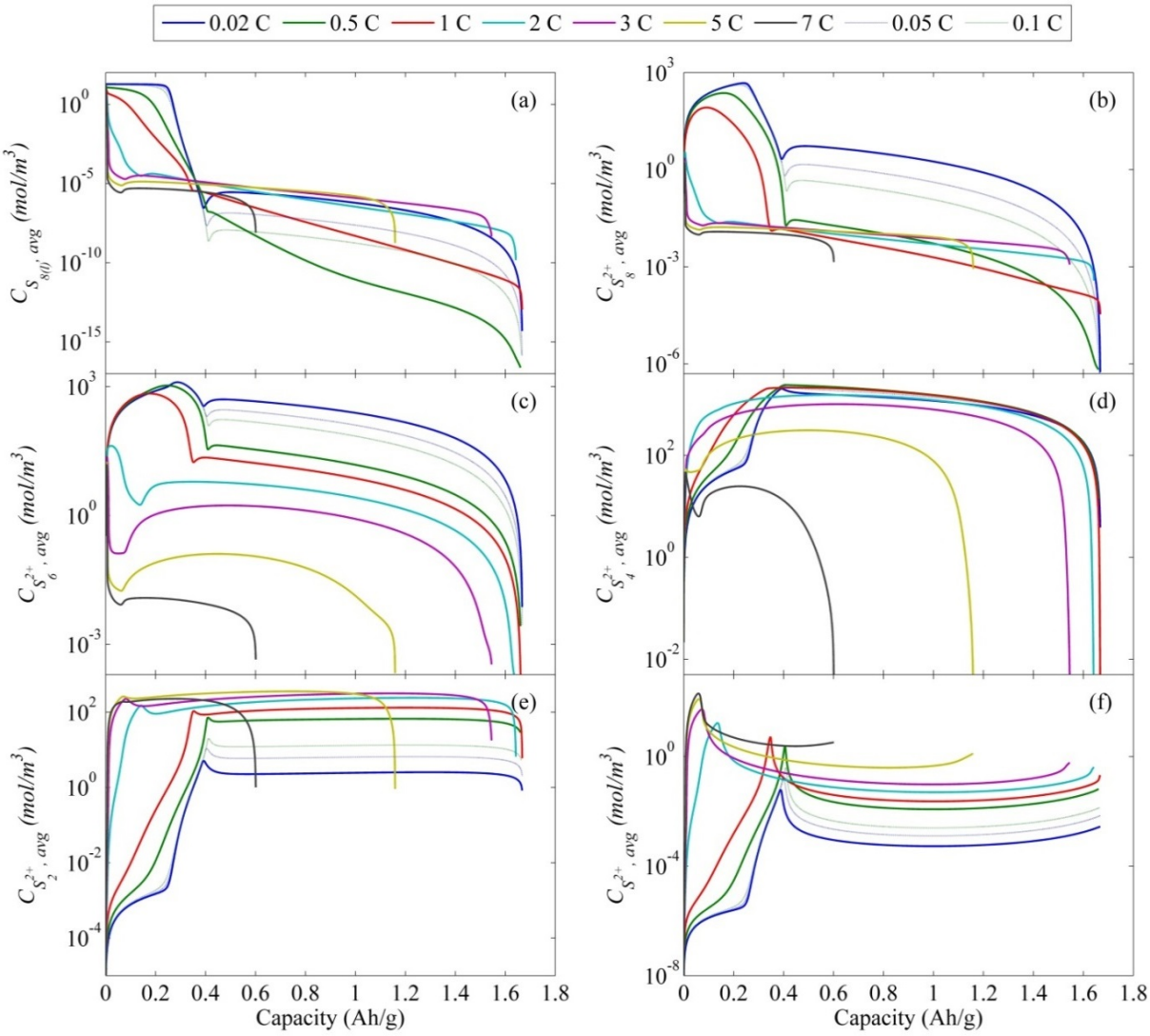

Figure 3.3: Average species concentration in the cathode during discharge. Increasing the discharge rate, high polysulfides' concentrations decrease and low polysulfides' concentrations increase.

is high for the related potential, a reverse reaction occurs for the high sulfides. Upon reaching a quasi-steady state, the rate of the last two reactions becomes constant during the remaining discharge time. However, the third reaction continues slowly. Once all of the sulfides have been reduced, a sudden drop in the potential occurs.

For a discharge current of 0.5 C and higher, sulfur dissolution is too slow to maintain a constant concentration of elemental sulfur in the electrolyte solution. Thus, the other reactions begin correspondingly sooner, creating smoother peaks and drops. However, up to a 1 C discharge rate, the dissolution is sufficiently fast to keep the first (and second) reaction dominant during the first stage of discharge. These reactions continue during the second part of the discharge because some solid sulfur is still present that can be dissolved into the electrolyte solution. The reverse reactions then cease due to the earlier start of the low-sulfide reactions in their relative time scales. Although the sharp troughs in potential and in the concentrations of high sulfides and concentration peaks of the low sulfides still exist when S^{2-} precipitation starts (for the reasons explained earlier), the sharp troughs in the high-sulfide concentrations no longer appear due to the reverse reactions. Instead, this trough now occurs as the species consumption rate drops due to a reduction reaction, concurrent with the production due to sulfur dissolution. The dependence of the dissolution/precipitation of each species on the nucleus size of each precipitate (Equation 2.24) is clearly observed in the volume fraction of elemental sulfur, which does not exhibit a linear decrease.

At 2 C, elemental sulfur does not dissolve fast enough for the first two reactions to be dominant. Low-sulfide reduction starts earlier, and the low-sulfide concentrations reach their maximum levels very quickly. Again, the start of S^{2-} precipitation causes the sharp trough in the levels of the high-sulfide concentrations and the peaks in low-sulfide concentrations. Whereas the high-sulfide reaction rates change smoothly over time, the reduction of S_4^{2-} exhibits a sharp trough at this starting point of precipitation and the last reaction reaches a peak. The solid sulfur particles dissolve more slowly as they become smaller. Thus, the sulfide species cannot be produced in the quantities required to participate in the reactions, causing the potential to drop and the end of discharge with some unused

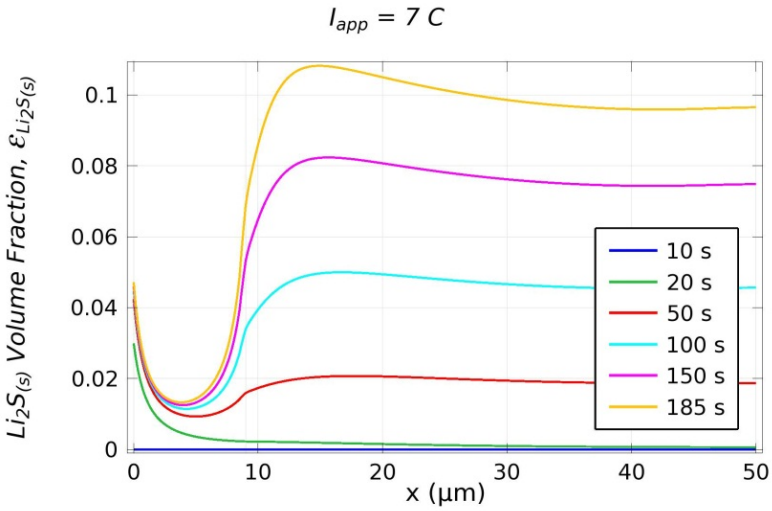

Figure 3.4: Volume fraction of $Li_2S_{(s)}$, $\varepsilon_{Li_2S_{(s)}}$ across the cell at different times of discharge with a current rate of 7 C. The interface of the separator and the cathode is located at $x = 9\ \mu m$.

solid sulfur remaining in the cathode.

At low discharge rates, the species concentration is nearly uniform in the cell because diffusion proceeds faster than the production and consumption. However, at high C rates, gradients in the concentration of the species are generated across the cell. For all the species, except S^{2-} and $S_{8(l)}$, the maximum concentration occurs at the interface of the anode and separator. The concentration gradients have higher slopes at the separator than at the cathode. The S^{2-} concentration exhibits the same behavior before precipitation starts but drops at both the separator and cathode once precipitation starts. However, comparing the concentrations in both areas, the S^{2-} concentration remains higher in the cathode because of its simultaneous production. Consequently, a concentration gradient forms at the cathode-separator interface. In contrast, a high concentration of S^{2-} and Li^+ at the anode and separator interface causes the relatively high precipitation of $Li_2S_{(s)}$ at the anode surface soon after discharge begins. Figure 3.4 shows the volume fraction of $Li_2S_{(s)}$ across the cell at different discharge times, at $I_{app} = 7\ C$. At t = 10 s, the volume

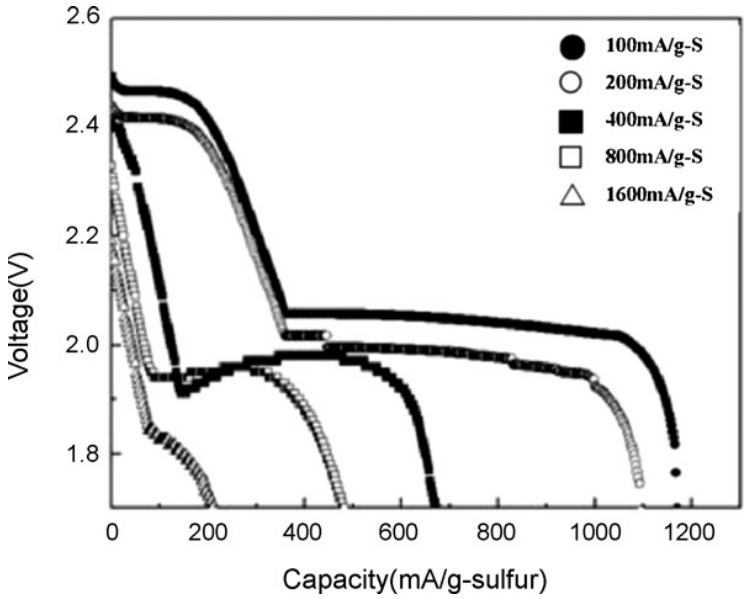

Figure 3.5: The discharge profile of various curents. Taken from Ref. [41]

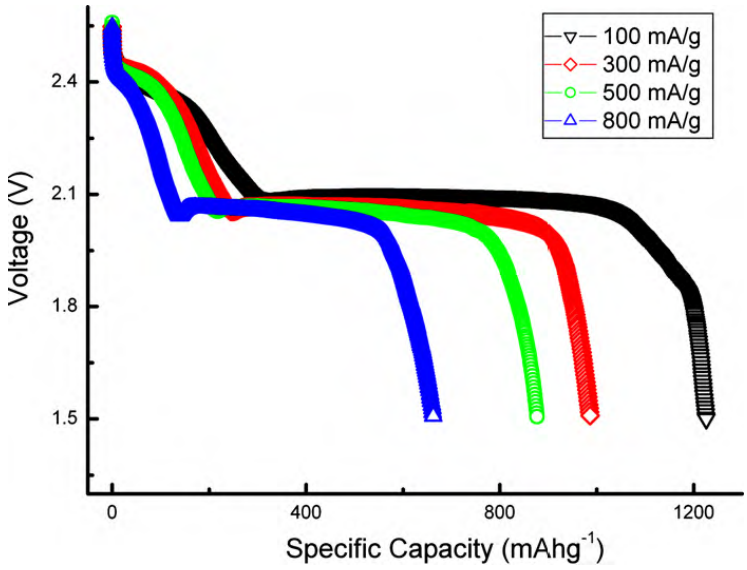

Figure 3.6: The discharge profile of various curents. Taken from Ref. [47]

fraction is almost zero everywhere. At t = 20 s, the volume fraction begins to increase and has a large maximum at the anode surface. Over time, the precipitation continues everywhere in the cathode where S^{2-} is produced. Moreover, the diffusion of S^{2-} into the separator causes $Li_2S_{(s)}$ to form deep in the separator (for the same reason, the volume fraction in the cathode at a short distance from the interface is less than that deep inside the cathode). However, the higher concentration of Li^+ at the interface causes a peak in $Li_2S_{(s)}$ volume fraction to form at a short distance from the interface inside the cathode. The formation of $Li_2S_{(s)}$ here would cause stresses in the cell and the deformation of the cathode during cycling.

Ryu et al. [41] and Wang et al. [47] have reported the vanishing first plateau and capacity loss being due to the increase of current density in Li-S cells. Their experimental results shown in Figures 3.5 and 3.6 support our modeling results.

3.2 Conductivity of the cathode, σ

Neither sulfur nor polysulfides are conductive; therefore, the cathode must contain a conductive porous matrix that holds sulfur in its pores and facilities the accessibility of electrons to the sulfur. The method of manufacturing the conductive matrix is one of the major difficulties in sulfur-based cell fabrication. On one hand, higher conductivity requires more conductive additives and less sulfur in the cathode, causing the cell to lose its specific energy capacity; on the other hand, lower conductivity causes less of the sulfur to be utilized as the active material. This section investigates the effect of the conductivity of the porous matrix on the cell performance. No difference in the matrix porosity is assumed; only the conductivity was varied. This investigation approach matches the situations in which the conductive additive is changed but not the amount used, assuming the porosity remains the same.

Figure 3.7 illustrates the effect of the conductivity of the cathode porous media matrix on the battery performance. The upper and lower sets of lines represent the voltage

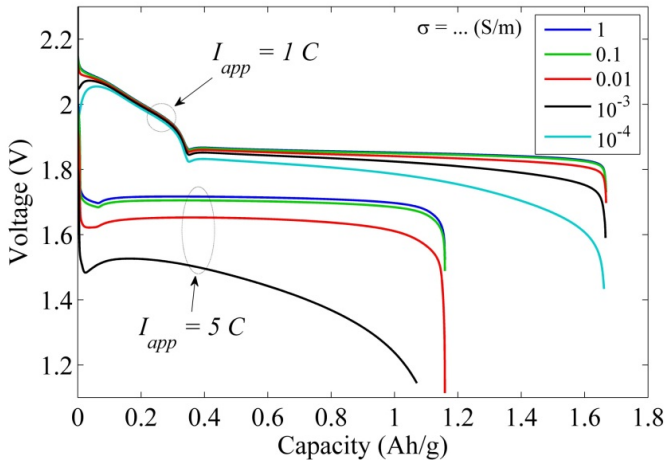

Figure 3.7: The discharge plateaus of the sulfur-based cell with different conductivities of the cathode matrix for discharge current rates of 5 C and 1 C.

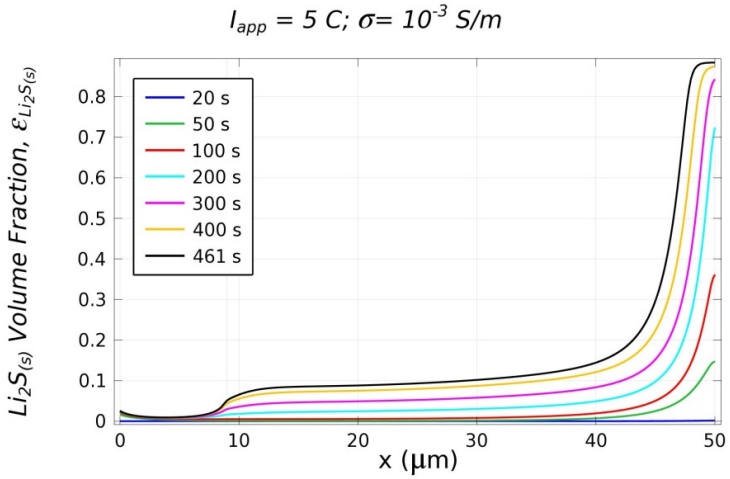

Figure 3.8: Volume fraction of $Li_2S_{(s)}$, $\varepsilon_{Li_2S_{(s)}}$ across the cell at different times of discharge for a discharge current rate of 5 C. The separator-cathode interface is located at $x = 9$ μm.

plateaus for a 1 C and 5 C discharge rate, respectively. The conductivity of the cathode matrix is assumed to vary from 1 to $10^{-4} S/m$. For the discharge rate of 5 C, the simulations for $\sigma = 10^{-4} S/m$ did not converge to a solution at times longer than approximately 2 s, i.e., it is not possible to discharge at a high C rate when the conductivity is low. The graphs indicate that once a certain conductivity threshold has been exceeded, no significant change occurs to the voltage plateau if the conductivity is increased further, indicating the dominant role of the reaction kinetics in the cell behavior. As the conductivity decreases, an unexpected drop in potential at the beginning of the cell discharge was observed. This drop is more obvious at a rate of 1 C. At low conductivity, the potential gradient in the cathode matrix is steep (unlike at high conductivity), with a minimum at the interface of the cathode and current collector. Therefore, a steep gradient in the concentration of the species is required for a well-distributed electrochemical reaction across the cathode. Since the species concentration is uniform, when cell discharge begins, a sharp drop in the potential of the solid matrix forms at the interface of the cathode and current collector to draw all of the current from this region. Over time, the production of more ions in the electrolyte causes a gradient in the species concentration to form, leading to a wider distribution of electrochemical reaction rates across the cathode. However, the reaction rate is still maximum at that interface, but it is not as sharp as before. At the end of the discharge, the smaller number of ions again causes a sharp potential drop to form at the interface. The high rate of low-sulfide production at the interface leads to formations of precipitants that fill the pores. Figure 3.8 presents the volume fraction of $Li_2S_{(s)}$ at the separator and cathode during discharge. The porous medium at the interface of the cathode and current collector, is completely filled by the precipitant. One may conclude that this filling phenomenon causes active material to be lost during cycling because the solid sulfur in that area does not have easy access to the electrolytes.

3.3 Rate constants for the precipitation reactions

Each rate constant controls the dissolution and precipitation rates of the related species. Although the model assumes that the precipitation rate and dissolution rate behave symmetrically around the saturation concentrations (see Equation 2.24) they behave differently far away from saturation: there is no limitation on the precipitation rates if the concentration of the species increases, but dissolution rates have an upper limit that depends on the related solubility product, rate constant and solid volume fraction.

Thus, the precipitated species may not completely re-dissolve into the solution to be involved in the reactions. In the model, an initial equilibrium between the electrochemical reactions and precipitation reactions is assumed; Numerical instability was observed when this assumption was ignored. Therefore, the solubility products are kept constant to satisfy to this assumption.

Generally, the solubility of each species and thus their respective rate constants depend on the type of solvent used. Because the kinetics of each reaction is influenced by the concentration of each species, the discharge voltage will also depend on the solvent. In this section, the rate constant parameters are the subject of study. Figures 3.9 and 3.10 present the simulation results for 0.1 C and 1 C, respectively.

The behavior for the rate constant $k_{8(s)}$ of solid elemental sulfur is simple. If the dissolution speed is fast compared to the reduction rate of $S_{8(l)}$, a two-stage voltage plateau exists. As the rate constant decreases, the $S_{8(l)}$ concentration and thus the discharge voltage become lower. The first discharge plateau vanishes, and the contribution of sulfur reduction in the discharge current decreases, causing $S_{8(s)}$ to exist longer in the system. As expected, for equal ratios of $k_{8(s)}/I_{app}$, similar behavior in the discharge and retained discharge capacity were observed (Figures 3.9a and 3.10a); only the onset of the sharp trough changes due to the different ratio of $k_{Li_2S_{(s)}}$ $/I_{app}$.

For the mid-polysulfide products, the behavior is more complicated, particularly on the voltage plateau. The effect of the rate constant on the capacity can be summarized

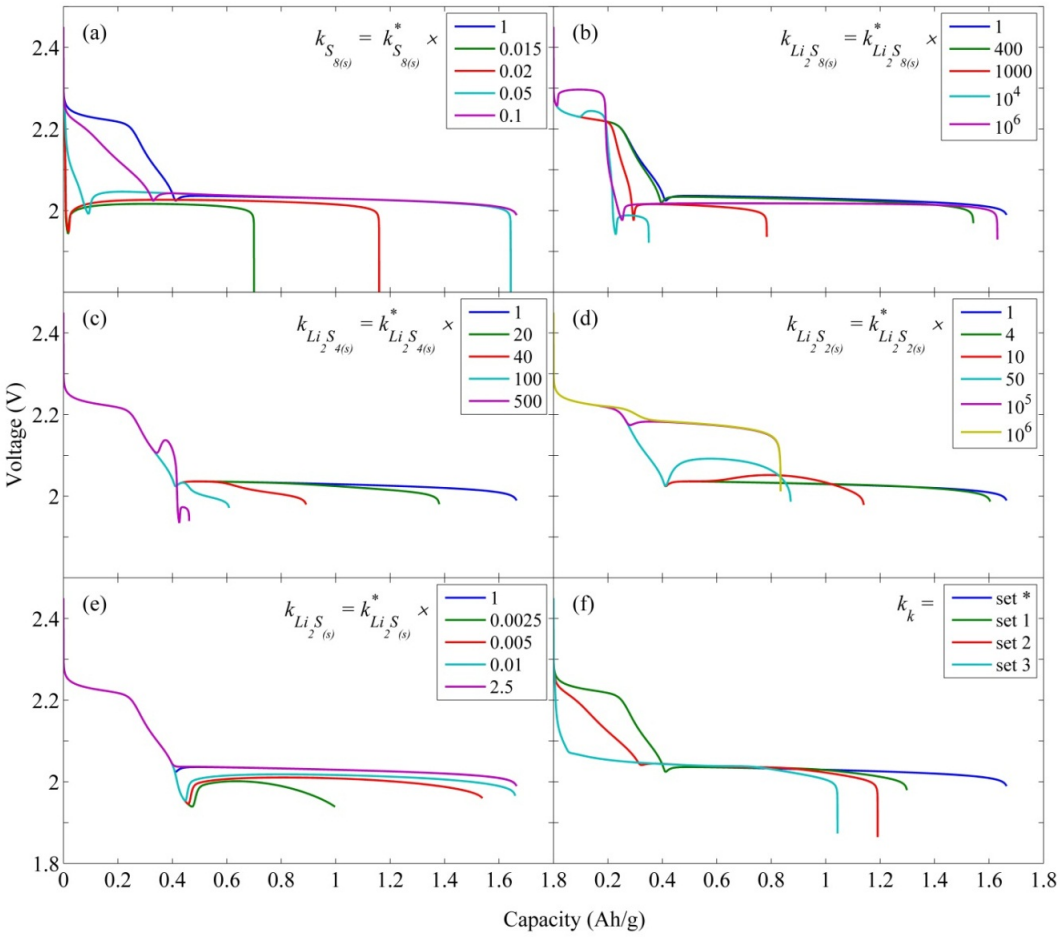

Figure 3.9: Discharge voltage plateau for different rate constants at discharge current rates of 0.1 C. (a) to (e) In each case, only the mentioned rate constant differs from the initial assumptions. (f) Some other cases for comparison. In each set, $k_k = k_k^* \times b_k$, and b_k are equal to one in "set *", (1, 1, 20, 6, 1) in "set 1", (0.1, 1, 25, 8, 2.5) in "set 2", and (0.051, 1, 60, 16, 250) in "set 3".

as follows. To start the precipitation of a species, a rate constant threshold is required, which depends on the concentration of the species and thus the applied current. As the rate constant exceeds the threshold to a greater degree, the amount of the solid phase of the species formed becomes greater. As mentioned earlier, rapid precipitation does not necessarily mean rapid dissolution. Also, the precipitated material is not involved in the electrochemical reaction, thus leading to capacity loss. If the rate constant is sufficiently large to reproduce the amount of species dissolved in the electrolyte, the retention capacity increases again. This type of behavior is observed for $k_{Li_2S_{8(s)}}$ and $k_{Li_2S_{4(s)}}$ (Figures 3.9b, 3.10b, and 3.10c).

The behavior of the system in the plateau region depends on more parameters and is more complicated. At 0.1 C, increasing $k_{Li_2S_{8(s)}}$ by a factor of 400 causes the threshold of initiating precipitation to be exceeded, leading to some capacity loss. If the rate constant is increased further, S_8^{2-} will be removed earlier and faster, causing the reduction of $S_{8(l)}$ to increase up to a peak; not not only the peak of I_3^N will vanish, but also the reverse oxidization of S_6^{2-} will make it negative. This phenomenon occurs for $k_{Li_2S_{8(s)}} \geq k^*_{Li_2S_{8(s)}} \times 1000$, causing significant capacity loss.

A factor of 10^4 makes this phenomenon stronger: as precipitation starts, when it passes its peak, the normalized current of the second reaction I_2^N reaches a value of 1 and the voltage increases, i.e., a new type of deep trough forms. Although precipitation has started, the S_8^{2-} concentration remains constant while all of the elemental sulfur is reduced. With a decrease in the concentration of $S_{8(l)}$, the potential also decreases and some of the S_8^{2-} will be reduced. Only a small portion of sulfur will be reduced to S^{2-} and so most of the capacity will be lost.

At $k_{Li_2S_{8(s)}} = k^*_{Li_2S_{8(s)}} \times 10^6$, almost all of the capacity can be maintained. Precipitated materials dissolve again, contributing to the electrochemical reactions.

A higher rate constant threshold is expected at 1 C. Interestingly, the lowest maintained capacity is much higher than at 0.1 C, and the potential along the first plateau always decreases. The key is the lower dissolution rate of elemental sulfur with respect

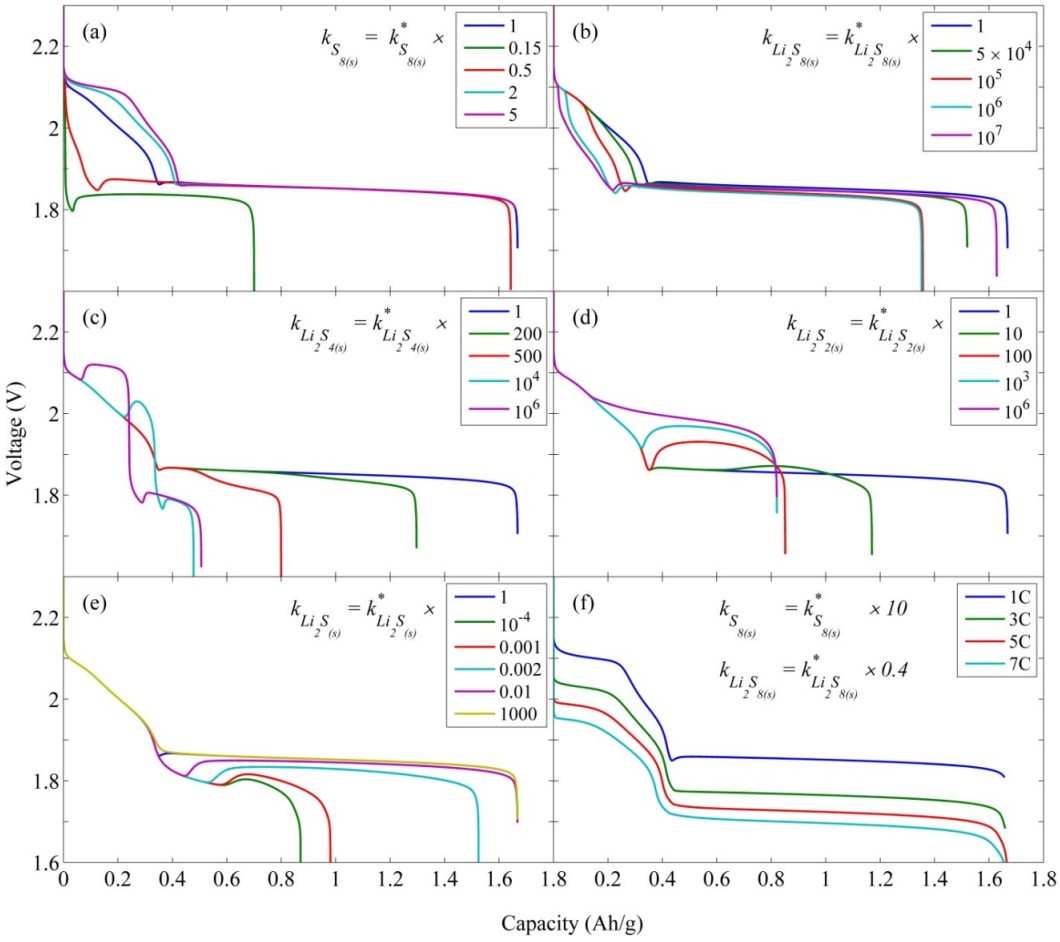

Figure 3.10: Discharge voltage plateau for different rate constants at a discharge current rate of 1 C. (a) to (e) in each case, only the mentioned rate constant differs from the initial assumptions. (f) Discharge voltage plateau at high C rates for the case with a high solubility of sulfur.

to the electrochemical reaction rates. Thus, the $S_{8(l)}$ concentration remains low, and I_2^N cannot reach 1; therefore, the voltage along the first plateau is reduced. In contrast, the S_8^{2-} concentration does not significantly exceed the saturation level, leading to slow precipitation compared to the electrochemical reaction rate. After a period of time, because the S_8^{2-} production rate is low, its concentration remains below saturation, even causing the precipitated material to re-dissolve in the electrolyte. Therefore, the cell discharges more evenly for the same ratios of $k_{Li_2S_{8(s)}}/I_{app}$.

The same explanation applies to the $k_{Li_2S_{4(s)}}$ parameter as well. If this rate constant is increased, active material is lost by precipitation. Eventually, an increase in this rate allows for re-dissolution, thus retaining more capacity. S_4^{2-} precipitation lowers its concentration, causing a decrease in potential along with a local minimum in I_5^N and I_6^N, whereas I_4^N rises to a peak. The decrease in potential allows for the pseudo-equilibrium of reaction rates.

At 0.1 C, only for $k^*_{Li_2S_{4(s)}} \times 500$ does S_4^{2-} precipitation occur before the second plateau, leading to another deep trough in the potential. At this point, the reduction of S_4^{2-} has not yet started. As the S_4^{2-} concentration decreases due to precipitation, less overpotential is required to reduce S_6^{2-} and the potential increases, leading to faster S_6^{2-} reduction and also to its partial reverse oxidization and the partial reverse oxidation of S_8^{2-}. The increased potential leads to a new semi-equilibrium between the electrochemical reactions (I_2^N, I_3^N and I_4^N) until the S_6^{2-} concentration decreases very suddenly, which causes a sudden decrease in potential. The same behavior is observed at 1 C.

As the rate constant $k^*_{Li_2S_{4(s)}}$ is increased by factors of 10^4 and 10^6, precipitation again occurs in the first plateau, causing another deep trough. At factors of 10^6 and higher, the discharge capacity starts to increase again.

Increasing $k_{Li_2S_{2(s)}}$ increased the amount of S_2^{2-} precipitation. As the constant rate becomes larger, the precipitation occures faster and the S_2^{2-} concentration decreases. Therefore, the potential increases along with an increase in I_5^N and a decrease in I_6^N. At $k^*_{Li_2S_{2(s)}} \times 50$, the precipitation of S_2^{2-} and S^{2-} both begin simultaneously (see Figure 3.9d). I_5^N increases to a very large peak and the potential raises. This leads to the reverse

oxidation of S_4^{2-}, with I_6^N becoming almost zero after a sharp and relatively small peak. Only a small portion of S_2^{2-} is reduced to S^{2-}.

Increasing the rate constant by a factor greater than 50 causes the precipitation to start before the second plateau. Consequently, the factors of 10^5 and 10^6 cause a large increase in the potential, and no reduction of S_2^{2-} occurs. Therefore, only half of the capacity is maintained.

The same behavior is observed at 1 C (see Figure 3.10d). For the same ratios of $k_{Li_2S_{2(s)}}/I_{app}$, the same discharge capacity is retained. Attempts to increase the discharge capacity by increasing the rate constant failed because of numerical instability.

The precipitation of the last polysulfide, S^{2-}, is controlled by $k_{Li_2S_{(s)}}$. Removing the last product from the electrolyte is necessary to fully discharge the cell and to avoid the cost of decreasing voltage due to high product concentration. As long as the rate constant is above a threshold (which depends on the applied current), product removal occurs completely and no change in the shape or behavior occurs (see the largest values of the rate constant in Figures 3.9e and 3.10e).

At 0.1 C , the only difference in the discharge plateau between the two highest values of the rate constant is the lack of the trough (also in 1 C , see Figure 3.10e). At high values of the rate constant, as soon as S_2^{2-} reduction begins, S^{2-} product begins to precipitate because very tiny solid phase nuclei can initiate the precipitation. However, at $k^*_{Li_2S_{(s)}}$, the tiny nuclei cannot initiate the precipitation, so the S^{2-} concentration exceeds the saturation point and the potential decreases until the very sudden start of precipitation removes the product, at which point the potential increases.

Decreasing the rate constant by a factor of 0.01 delays the precipitation, which causes the accumulation of S^{2-} in the electrolyte, thereby resulting in a further decrease in the potential. The lower potential causes enhanced production of S_2^{2-} as well so that it starts to precipitate; however, the precipitation does not last long because S^{2-} suddenly starts to precipitate. The removal of S^{2-} brings the potential back to a higher level, along with a very large peak of S_2^{2-} reduction, its reverse oxidization to S_4^{2-} and even reverse oxidization

to S_6^{2-}. As the rate constant continues to decrease, the precipitation becomes more delayed and these effects become stronger.

At $k^*_{Li_2S_{(s)}} \times 0.0025$, $Li_2S_{2(s)}$ is the predominate precipitate; therefore, the discharge capacity only just exceeds half of the total capacity. Note that as the S_4^{2-} concentration (and also S_6^{2-}) decreases due to electrochemical reactions and most of the S_2^{2-} is removed by precipitation and not by the electrochemical reactions (the contribution of I_6^N in total current is weak), the potential gradually decreases to maintain the reduction of S_4^{2-}.

The same behavior is observed at 1 C, except that the deep trough is stretched over awider capacity range (Figure 3.10e). When the reduction of both S_4^{2-} and S_2^{2-} begins, elemental sulfur and the high polysulfides are still being reduced as well (whereas at 0.1 C, no significant reduction of the high polysulfides occurs because they are all consumed; see Figure 3.2). Therefore, I_5^N is not as high as in the 0.1 C case; as a result, on the time scale of the 1 C case, the precipitation is delayed longer, thereby leading to the stretched trough. When the rate constant is decreased by a factor of 0.002 or lower, S_2^{2-} precipitation also occurs. At the factor of 0.001, S_2^{2-} precipitation starts slightly before S^{2-} precipitation and constitutes the major solid phase. Decreasing the rate constant by a factor of 10^{-4} causes all of the precipitation to be $Li_2S_{2(s)}$ instead of $Li_2S_{(s)}$, resulting in a discharge of only half of the capacity.

Three representative cases are presented in Figure 3.9f to emphasize the nonlinear behavior of the system. In each set, $k_k = k_k^* \times b_k$. b_k is equal to 1.0 in "set *", (1, 1, 20, 6, 1) in "set 1", (0.1, 1, 25, 8, 2.5) in "set 2", and (0.051, 1, 60, 16, 250) in "set 3". The only difference between the discharge plateau of "set *" and "set 1" is the shorter second plateau. The higher rate constants for $Li_2S_{4(s)}$ and $Li_2S_{2(s)}$ cause the loss of capacity. At the end of the discharge, the volume fractions are approximately 0.037 and 0.025 for $\varepsilon_{Li_2S_{2(s)}}$ and $\varepsilon_{Li_2S_{4(s)}}$, respectively. $\varepsilon_{Li_2S_{(s)}}$ drops from approximately 0.287 in "set *" to 0.183 in "set 1". In "set 2", decreasing $k_{8(s)}$ by a factor of 0.1 makes the first discharge plateau similar to that at the 1 C discharge rate (see Figure 3.10). However, the three last rate constants lead to a significant capacity loss. Note that the second plateau remains

fairly flat. The volume fractions are approximately 0.039, 0.037, and 0.159 for $\varepsilon_{Li_2S_{4(s)}}$, $\varepsilon_{Li_2S_{2(s)}}$, and $\varepsilon_{Li_2S_{(s)}}$, respectively. "Set 3" indicates the rate constants for which only one discharge plateau occurs.

A comparison of different discharge rates for the cell with high solubility is shown in Figure 3.10f. Even for a very high rate of 7 C, all of the capacity is retained. The two plateaus are easily distinguishable. In addition, the sharp curves become smooth, particularly in the deep trough that disappeared. The reason for this behavior is the dependency of dissolution on the size of the particle; for high C rates, as sulfur particles become smaller, they dissolve slower than the rate of the electrochemical reactions, thus causing a smooth start and end for each electrochemical reaction and thus a smooth increase or decrease of the concentrations of the species. Consequently, S^{2-} starts to precipitate gradually, not suddenly, and the trough disappears.

The location of the precipitated material is very important. If the rate constant is high, the species precipitate inside the cathode. However, if the rate constant is small, the dissolved species diffuses into the separator and precipitates there as well. To illustrate this effect, the volume fraction of $Li_2S_{(s)}$ is presented in Figure 3.11, which demonstrates that a further decrease in the rate constant leads to an increase in the formation of the solid phase in the separator. Such movement of the active material to the separator is a cause of capacity fading by cycling. Considering the possibility of higher-polysulfide precipitation makes this fading effect even worse. For example, Figure 3.12 shows the volume fraction of $Li_2S_{2(s)}$ and $Li_2S_{(s)}$ across the cell at the end of a discharge. The low rate constant of $k_{Li_2S_{2(s)}}$ leads to a uniform precipitation across the entire cell. However, a large rate constant leads to the presence of more solid phase everywhere compared to the case of a low rate constant, but not distributed uniformly. The volume fraction is higher in the cathode.

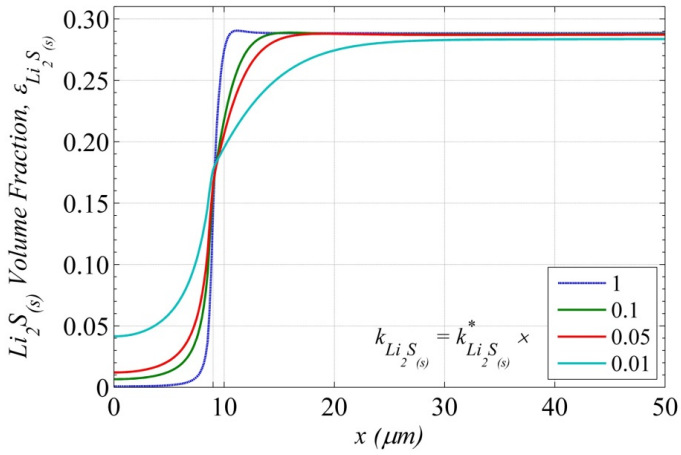

Figure 3.11: Volume fraction of $Li_2S_{(s)}$, $\varepsilon_{Li_2S_{(s)}}$ across the cell at the end of a discharge with a discharge current rate of 0.1 C. The separator-cathode interface is located at $x = 9\ \mu m$.

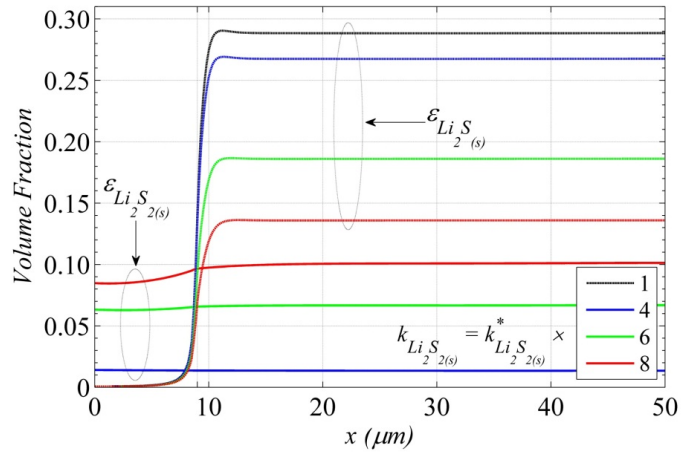

Figure 3.12: Volume fraction of $Li_2S_{(s)}$ ($\varepsilon_{Li_2S_{(s)}}$) and $Li_2S_{2(s)}$ ($\varepsilon_{Li_2S_{2(s)}}$) across the cell at the end of a discharge with a discharge current rate of 0.1 C.

3.4 Sulfur content

It is desirable to increase the energy density of a battery by increasing the active material content per volume of the cathode. The volume expansion of the sulfur products during the discharge processes and the porosity loss are limitations that place an upper limit on the sulfur content. This section provides a quantitative discussion of the cell behavior with respect to the sulfur content based on the discharge current rate. Based on the model, the entire cathode-electrolyte interface is considered to be an active surface for electrochemical reactions, thus ignoring the insulating nature of sulfur and the precipitated polysulfides. Therefore, the negative phenomenon of losing active surface area for electrochemical reactions is not considered. For simplicity, the volume ratio of conductive material in a cathode and its structure (porosity and specific surface area) are assumed to remain constant even if the sulfur content is changed.

Simulations were performed at the three different discharge current rates of 0.25, 2.5, and $25 A/m^2$. Figure 3.13 presents the discharge curves for various sulfur content levels, while Figure 3.14 presents the final retained discharge capacity as a function of sulfur content. Both of the figures indicate that cells with less than 20% sulfur content (per volume of cathode) can be fully discharged, even for high discharge rates of approximately 1 C. At a high discharge current rate of $25 A/m^2$, the short first plateau and no trough are expected, as explained earlier.

When the sulfur content is 0.3, at higher discharge rates, the voltage plateaus are very similar to those in Figures 3.9d and 3.10d when $Li_2S_{2(s)}$ forms, whereas at 0.25, the discharge rate is similar to that in the plateaus with S_4^{2-} precipitation (see Figures 3.9c and 3.10c). At a discharge rate of $25 A/m^2$, if the sulfur content exceeds 30% of the cathode volume, the first discharge plateau attains its full shape because $\varepsilon_{8(s)}$ is sufficiently large to keep the dissolution sufficiently fast for a longer time. An almost constant $S_{8(l)}$ concentration is obtained, and consequently, a sufficiently high S_8^{2-} concentration in the electrolyte (as the reduction product of elemental sulfur) is achieved. Thus, no potential reduction is required to involve S_8^{2-} in the electrochemical reaction. At a sulfur content of

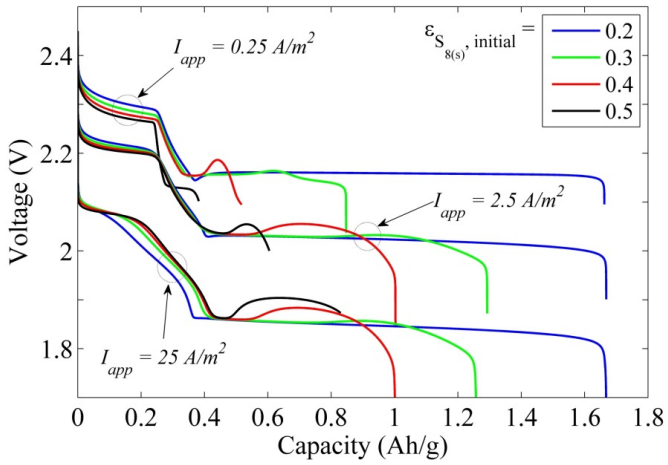

Figure 3.13: Discharge curves at different volume fraction of sulfur content and discharge current rates.

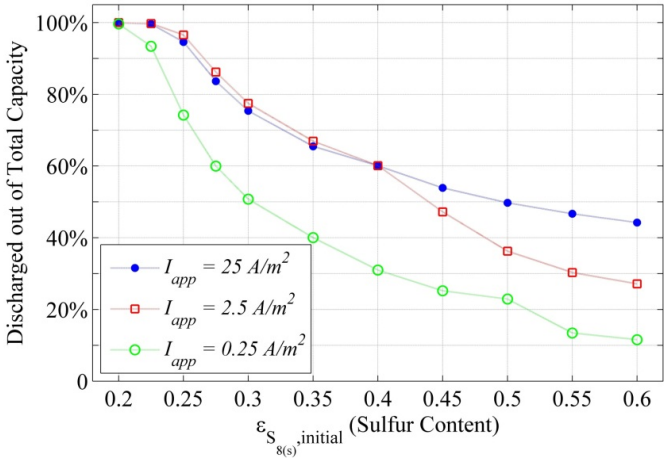

Figure 3.14: Discharge capacity percentage out of the total capacity for the cells with different sulfur contents and at various discharge rates.

0.4, the voltage plateaus at high discharge rates are similar to those in previous simulation results; at low discharge rates, the voltage plateau has an unexpected shape and end.

Figure 3.14 provides more details of the discharge capacity. For a low discharge rate, the discharge capacity percentage decreases rapidly because the reduction reactions of the different polysulfides occur more individually, i.e., a polysulfide is almost reduced completely before its product start its subsequent reaction. Therefore, the concentration of high polysulfides can reach the saturation concentration and begin to precipitate. At a discharge rate of $0.25A/m^2$, even a sulfur content of 0.225 increases the S_4^{2-} concentration to the saturation point such that $\varepsilon_{Li_2S_{4(s)}}$ at the cathode area is almost 0.02 on average. This volume fraction increases to approximately 0.334 when the sulfur content is 0.4, whereas $\varepsilon_{Li_2S_{(s)}}$ decreases to approximately 0.06.

Increasing the sulfur content to over 0.4 causes a $Li_2S_{8(s)}$ solid phase to form. This solid phase has a sudden increase at a sulfur content over 0.45, reaching an amount of approximately 0.27 at a sulfur content of 0.5. Thus, the capacity decreases at this point. When the sulfur content is 0.55, all of the solid phase is $Li_2S_{8(s)}$. Even at 0.6, approximately 0.07 of the sulfur volume fraction remains in the cathode without being involved in the reactions. For all of these sulfur content levels, only an insignificant amount of solid $Li_2S_{2(s)}$ forms because of the simultaneous reduction of S_4^{2-} and S_2^{2-}, which prevents the S_2^{2-} concentration to reach the saturation point. In the previous section, high polysulfides were shown to precipitate everywhere in the cell. Large amounts of precipitated material can block the cathode-separator interface. At a discharge current rate of $0.25A/m^2$, this blocking phenomenon occurs for cells with a sulfur content of 0.4 and greater.

At high discharge current rates, the partial simultaneous reduction of the different polysulfides prevents the saturation of a high polysulfide and causes a higher capacity to be retained than at low discharge currents. At a discharge rate of $2.5A/m^2$, the predominant solid phase changes from $Li_2S_{(s)}$ to $Li_2S_{2(s)}$ when the sulfur content is raised to 0.4 ($Li_2S_{(s)}$ and $Li_2S_{2(s)}$ become approximately 0.162 and 0.354, respectively). A very small amount of $Li_2S_{4(s)}$ forms when the sulfur content is 0.4 (approximately 0.02). However, an increase in

the sulfur content to 0.45 causes its volume fraction to raise suddenly (approximately 0.12) and an even greater reduction in the discharge capacity. The details of the average volume fractions of the precipitants in the cathode area are provided in Figure 3.15. At this point, the cathode-separator interface becomes blocked as well. The higher sulfur content leads to an increase in the amount of $Li_2S_{4(s)}$ precipitate. The precipitated material almost completely fills the pores of the separator (the porosity becomes less than 0.05 in the separator at a sulfur content of 0.6) and blocks the cathode-separator interface.

At a high discharge rate of $25A/m^2$, no solid phase of $Li_2S_{4(s)}$ forms, resulting in the smooth blue line in Figure 3.14. For sulfur contents greater than 0.4, the cathode-separator interface is blocked. The slightly lower discharge capacity at $25A/m^2$ than $2.5A/m^2$, when the sulfur content is between 0.225 and 0.4, is related to the relatively earlier appearance of S_2^{2-} at the higher current rates, which causes slightly more precipitation.

To find the optimum sulfur content to obtain the highest cell capacity, its effect on the discharge capacity per surface area of the cathode is presented in Figure 3.16. The optimum sulfur content is between 0.225 and 0.25, depending on the discharge current. However, considering the movement of active material to the separator due to the precipitation of $Li_2S_{n\geq 2}$, one should keep the sulfur content below 0.225 to avoid poor cyclability.

The shapes of the curves in the graphs shown in Figures 3.14 and 3.16 suggest a way to distinguish the precipitant as the final product of the discharge process. Each of the points in the figure which exhibits a sudden decrease in the line indicates that the discharge capacity is related to the initiation of the precipitation of the species.

Note that these results depend on the coefficients of the precipitation rate constants, particularly the shape of the voltage plateaus. However, the result that at high sulfur contents, a higher discharge capacity is observed at high discharge rates, unlike at low discharge rates, is a direct consequence of the assumed chain of reduction, meaning that other sets of rate constants exhibit the same results. At low discharge rates, the reduction of the various species does not occur simultaneously, thus leading to the saturation of high polysulfides.

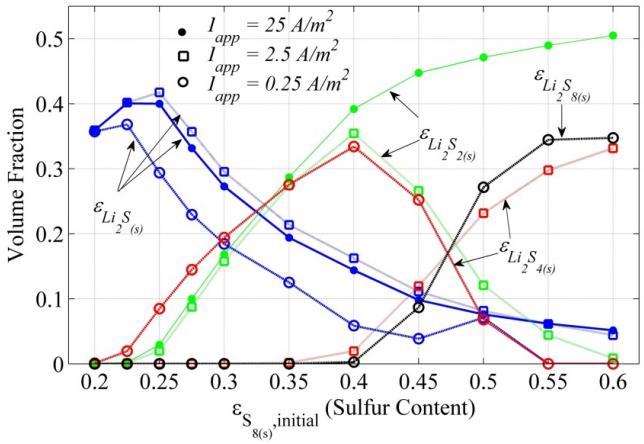

Figure 3.15: Average volume fraction of precipitants across the cathode at the end of a discharge for different discharge currents.

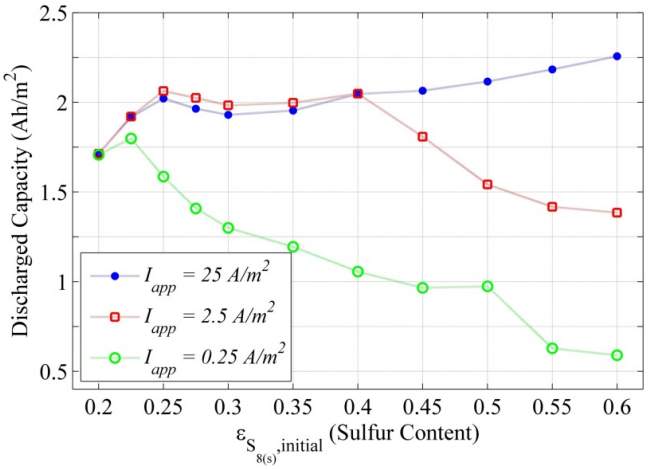

Figure 3.16: Discharge capacity per unit surface area of the cathode for different sulfur contents and at various discharge rates.

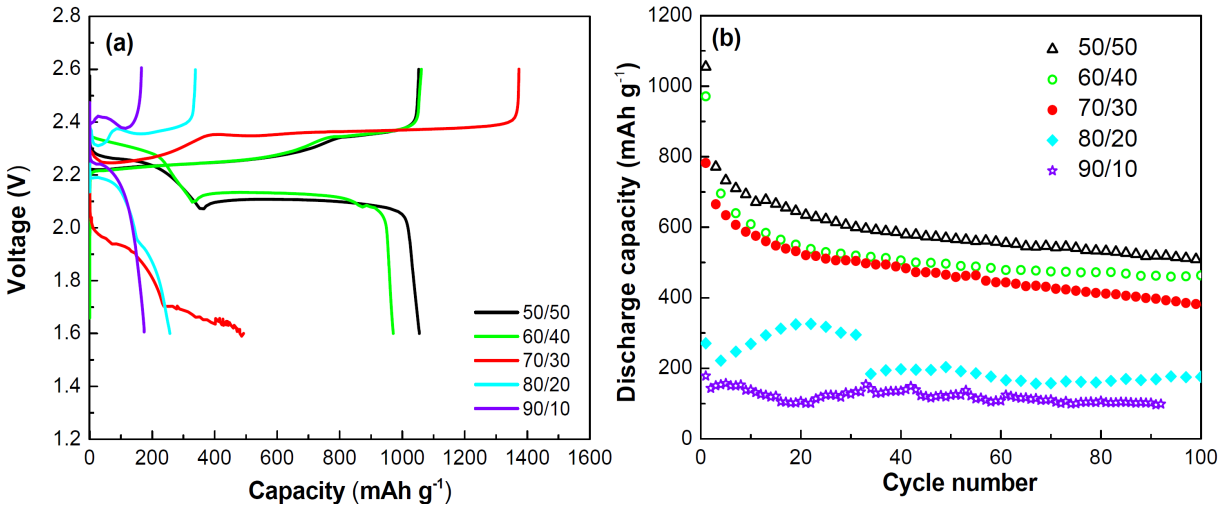

Figure 3.17: (a) voltage profiles, and (b) Discharge capacity vs. cycle number of the Li-S cell with different sulfur/carbon ratios. Taken from Ref. [51]

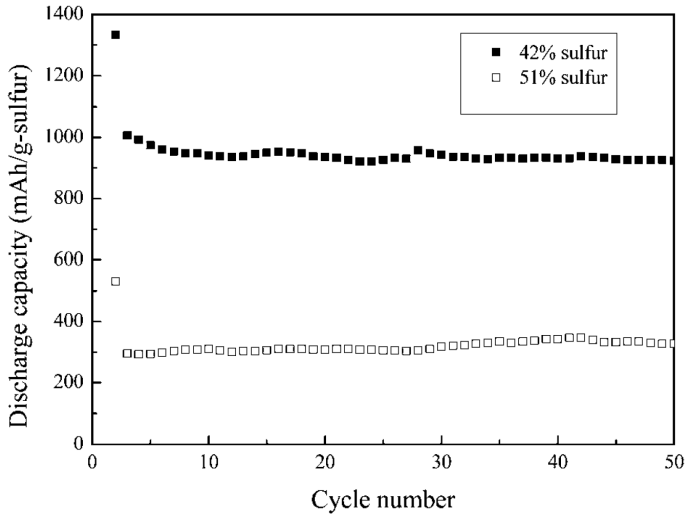

Figure 3.18: Cycle performance of the sulfurcarbon sphere composites with 42 wt% and 51 wt% sulfur at the low current density of $40 mA g^{-1}$. Taken from Ref. [53]

In carbon-sulfur composite cathodes, as one of the most popular methods for cathode preparation, liqified sulfur (or dissolved in a solvent) diffuses into the porous structure of carbon [24, 53]. Therefore, the morphology of the carbon structure does not significantly change. The ratio of carbon/sulfur only determines the ratio of pore volume to sulfur volume without a large change in the conductivity of carbon matrix. In this case, the behavior of the system follows the results of this section on sulfur content. However, high amounts of sulfur may disconnect carbon particles and cause the effective conductivity of carbon matrix to decrease. Xu et al. [51] (see Figure 3.17) and Zhang et al. [53] (see Figure 3.18) have reported a loss of specific capacity with increase in sulfur content. They used molten sulfur diffusion into the carbon micropores. When other methods of preparation of carbon-sulfur cathodes, such as mixing [24] or carbon coating on a surface of sulfur cathode [9] are used, the morphology of the carbon matrix changes depending on the carbon/sulfur ratio. However, with this change of morphology, the available surface area of the carbon matrix may not change considerably. The conductivity of carbon matrix is subjected to the most significant change since higher carbon content directly increases the conductivity of the cathode.

3.5 Thickness of the cathode

The effect of the thickness of the cathode on the discharge capacity and discharge voltage was also investigated. Figure 3.19 presents the discharge capacity of cells with different thicknesses at discharge rates of 2 C and 5 C. Furthermore, the discharge capacity per unit surface area of the cathode is presented in Figure 3.20. The amount of active material is proportional to the thickness of the cathode. Therefore, applied current density is proportional to the thickness at a given C rate. The discharge capacity remains constant up to a certain thickness for each discharge rate, as it is affected only by the rate at which elemental sulfur dissolves in the electrolyte. At thicknesses larger than $\sim 300\mu m$ at 2 C and $\sim 200\mu m$ at 5 C, the capacity decreases as the cathode becomes thicker. Capacity is

lost due to polysulfide precipitation, which blocks the surface of the anode. The overall shape of the discharge voltage plateau does not change depending on the thickness; only a downward shift is observed. As the loss in capacity starts, the voltage plateau shape is the same, except for a sudden decrease at the end of its discharge. As a good approximation of the downward shift of the discharge potential, the drop in potential with respect to that observed at the smallest thickness ($25\mu m$) at different points in the cell, at t =50 s at 5 C and 500 s at 2 C, is plotted in Figure 3.21. The green lines denote the drop in polarization at the surface of the anode with respect to the that at the smallest thickness. Because the applied discharge current is proportional to the thickness, the drop of the liquid potential at the surface of the anode has a logarithmic dependence on the thickness ratios. The blue lines denote the potential drop of the liquid phase at the current collector surface at the cathode side. The difference between the blue and green lines provides a good estimation of the resistivity in mass transfer. A small difference is observed for 2 C, indicating that mass transfer does not cause a large drop in potential; however, at 5 C, the difference is very large for thick cathodes, meaning that mass transfer causes a large decrease in potential. The red lines denote the decrease in potential at each thickness respect to that at the smallest thickness. The difference between the red and green lines is the overall decrease due to both polarization in the cathode and mass transfer in the cell, whereas the difference between the red and blue lines provides an approximation of the decrease in potential due to polarization. For small thicknesses, the decrease in potential is due to polarization at the surface of the anode. Whereas polarization remains the main cause of the decrease in potential at 2 C, mass transfer is the main cause for the potential drop at 5 C.

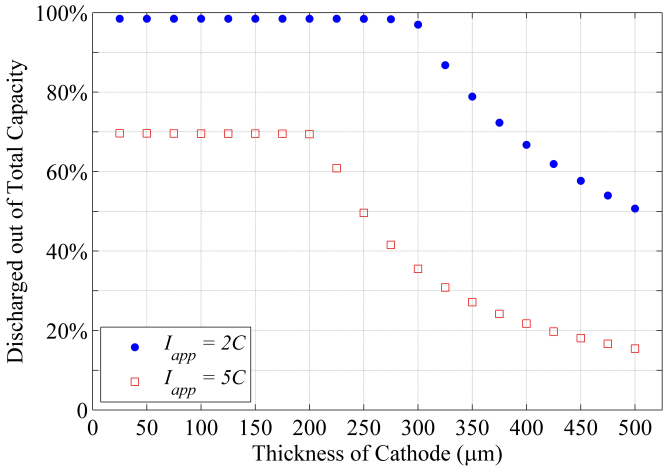

Figure 3.19: Discharge capacity percentage out of the total capacity for the cells with different cathode thicknesses at discharge rates of 2 C and 5 C.

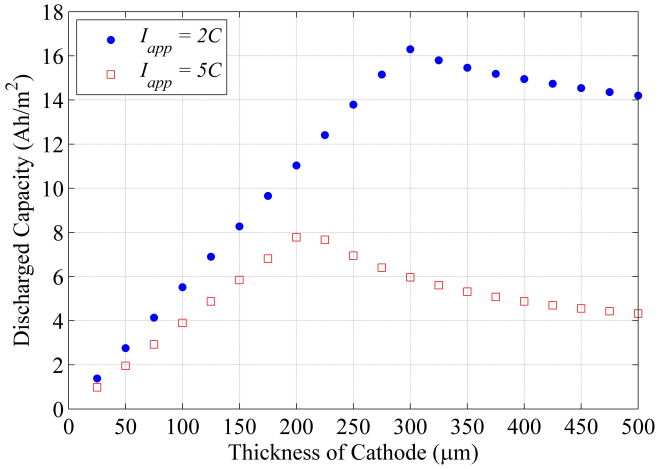

Figure 3.20: Discharge capacity per unit surface area of the cathode with different cathode thicknesses, at discharge rates of 2 C and 5 C.

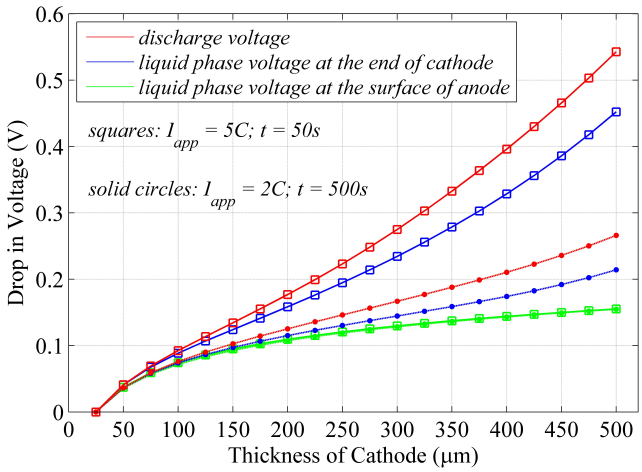

Figure 3.21: Decrease in voltage of the liquid phase at the end of cathode and at the surface of anode versus the cathode thickness for discharge rates of 2 C and 5 C at two specific times.

3.6 Charging the modeled cell and solubility product of precipitates

All the attempts to charge the modeled cell failed due to numerical instability caused by sudden increase of potential and drop of the concentration of S^{2-} in electrolyte. The only way to charge the modeled cell is by a significant increase of the solubility product of Li_2S. However, the low polysulfides are not very soluble [12, 55, 24, 21].

Figure 3.22 shows the voltage plateaus of discharge and charge of the modeled cell for different values of $K_{Li_2S_{(s)}}$, at applied current density of $0.02C$. The cell is first discharged and then is left at rest for 5 hours to relax to a semi-equilibrium state (open circuit potential (OCP)). Afterward, the cell is charged at constant current untill the voltage rise becomes vertical. Subsequently, cell is left at rest for 5 hours again to relax to OCP.

The solubility products of polysulfides do not have a considerable effect on discharge, except for $K_{8(s)}$, which determines the voltage of the first plateau. On the other hand, the

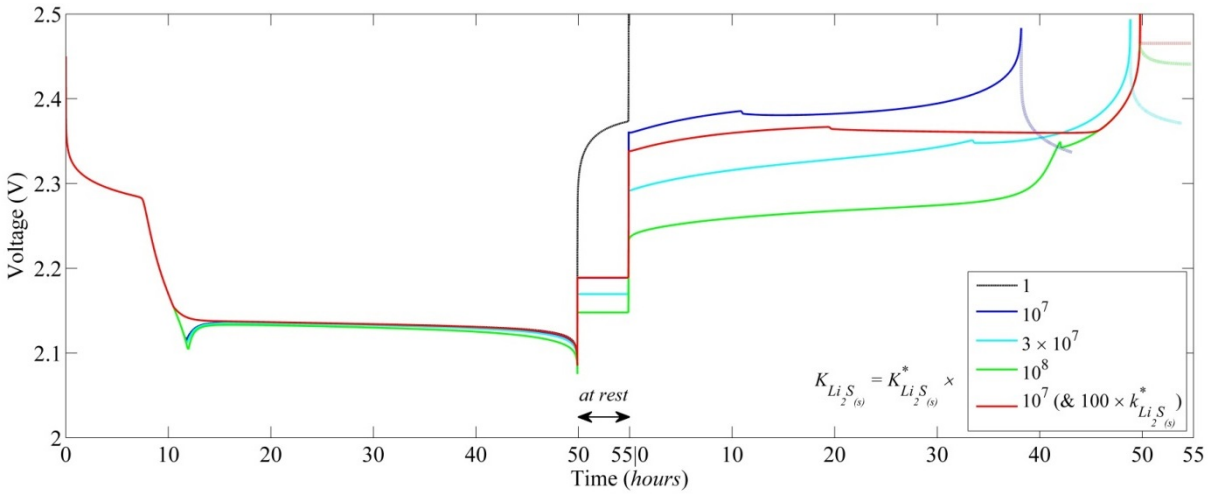

Figure 3.22: The cycle voltage plateau of Li-S cell at a current of $0.02C$, at different solubility of Li_2S. The cell is discharged completely first and the relaxed for 5 hours before being charge at constant current. At the end cell is left for 5 hours to relax to OCP.

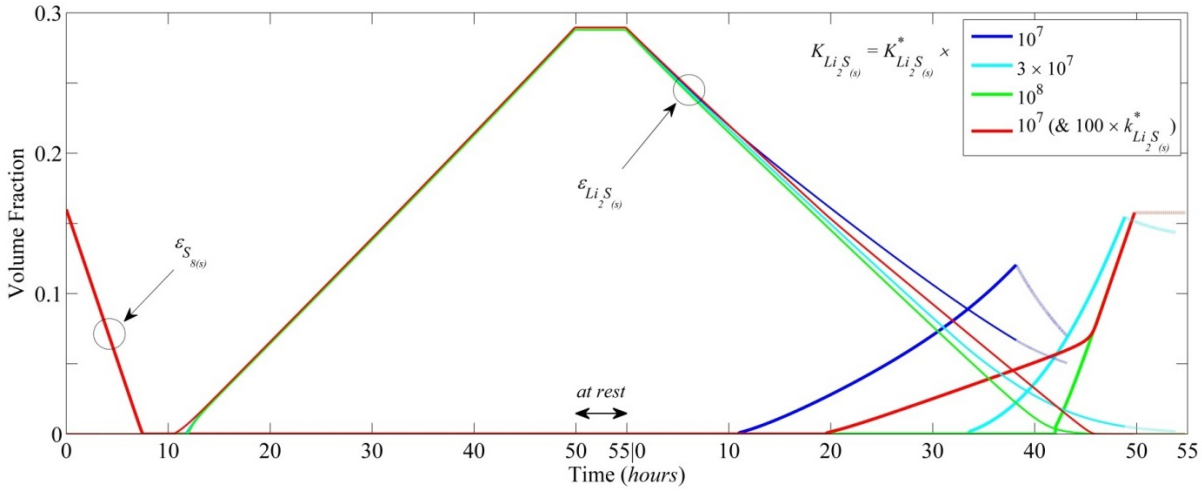

Figure 3.23: Volume fraction of elemental sulfur and Li_2S, during cycle.

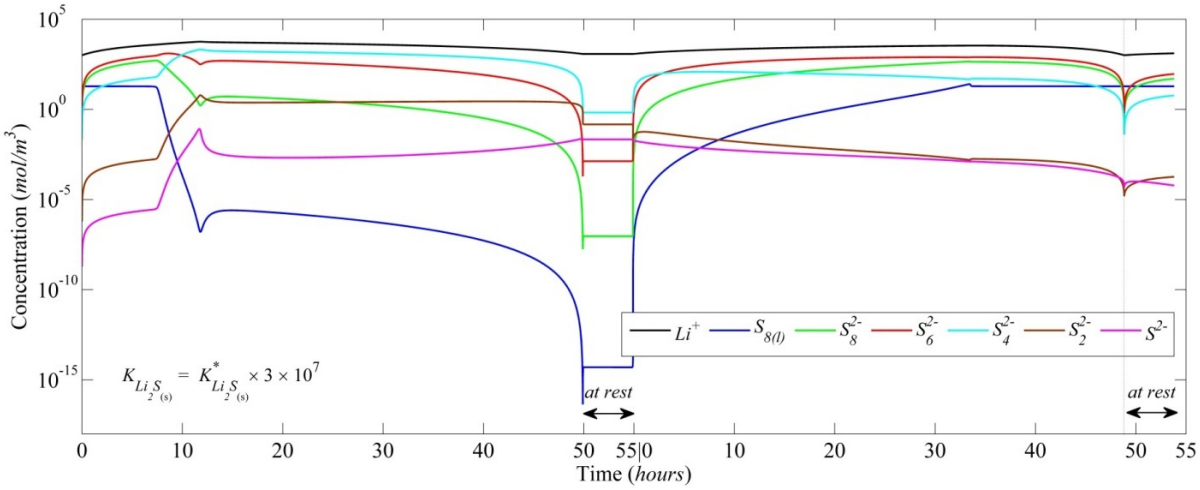

Figure 3.24: Concentration of species during cycle at $K_{Li_2S_{(s)}} = K^*_{Li_2S_{(s)}} \times 3 \times 10^7$.

OCP at the end of discharge and the discharge voltage plateau strongly depend on the value of $K_{Li_2S_{(s)}}$.

At low solubility of Li_2S, the model cannot be charged, as illustrated in the black dotted line in Figure 3.22. With the assumed parameters listed in Tables 2.4-2.7 and charge rate of $0.02C$, $K_{Li_2S_{(s)}}$ must increase, at least, by a factor of 10^7. Even in this case, it is not possible to charge the cell completely at a constant current. Because of low concentration of S_2^{2-}, a large polarization for oxidation is necessary. Therefore, as soon as the intermediate polysulfides form, they oxidize to high polysulfides and eventually to sulfur. Thus, solid phase of sulfur forms in the early stages of the charge. The small peak in the charge voltage plateau shows the starting point of sulfur precipitation. The volume fraction of elemental sulfur and Li_2S is also presented in Figure 3.23.

Increasing $K_{Li_2S_{(s)}}$ by a factor of 10^8, makes it possible to charge the model almost completely. High concentration of S^{2-} requires lower polarization for oxidation which is below the reference potential of high polysulfide electrochemical reactions. Therefore first, almost, the entire solid Li_2S is dissolved and oxidized before the high polysulfides and elemental sulfur form.

For the purpose of comparison, simulations are also performed for the case where solubility product and rate constant of Li_2S are both increased. The result is shown in the red lines in Figures 3.22 and 3.23. In this case, lower polarization is observed compared to the case with the same solubility product.

A large potential drop during the relaxation time at the end of charge is observed. The drop strongly depends on $K_{Li_2S_{(s)}}$ and the depth of the charge. During the relaxation time, dissolution of solid phases is also observed, except for the full charge cases. The change in the species concentrations and the availability of solid phases and their rate of precipitation/dissolution determine the speed of reaching OCP. To better understand the system, the concentration of species during the cycle for the case of $K_{Li_2S_{(s)}} = K^*_{Li_2S_{(s)}} \times 3 \times 10^7$ is shown in Figure 3.24. Low concentration of low polysulfides and high concentration of high polysulfides explains the large polarization during the charge process of the cell. During relaxation, however, the concentration of elemental sulfur remains almost constant, the concentration of polysulfides increase except for S^{2-}. As can be seen in Figure 3.24, concentration of S_6^{2-} shows the most rise. In fact the electrochemical reactions favour the formation of S_6^{2-}; thus higher polysulfides are reduced and lower ones oxidized to S_6^{2-}.

Although the model can reproduce the two typical voltage plateaus during charging [12, 55, 24] (when high solubility of Li_2S is assumed), it cannot reproduce the voltage peak at the beginning of the charge process. Also, to the best of our knowledge, no peak related to precipitation of sulfur has been seen in experiments. Therefore, because of these details, and also, because of high solubility of Li_2S which model requires for charging, we suggest that modification of the cell charge mechanism is necessary.

Chapter 4

Introduction to Aqueous Li-Ion Batteries

4.1 Large-scale energy storage batteries

During the past decades, the demands for innovative energy storage devices have been increased significantly in respond to energy technology evolution. New energy supplies must be cheap and sustainable. Wind, ocean waves and solar power have been considered possible sustainable natural sources, but require large-scale energy-storage devices too. For large-scale applications, energy storage technologies generally can be categorized under four different types: mechanical, electrical, chemical, and electrochemical [11]. Among all, pumped hydroelectric systems account for 99% of the worldwide storage capacity [11]. Figure 4.1 illustrates the characteristics of several energy storage systems. Methods such as pumped-hydro and compressed air are location dependent and suffer from relatively low energy efficiency.

As shown in Figure 4.1, a large variety of energy storage systems are based on electrochemical technology and indicate that batteries are the potential solution to the need for storing energy [11]. Their desirable features, such as pollution-free operation, high ef-

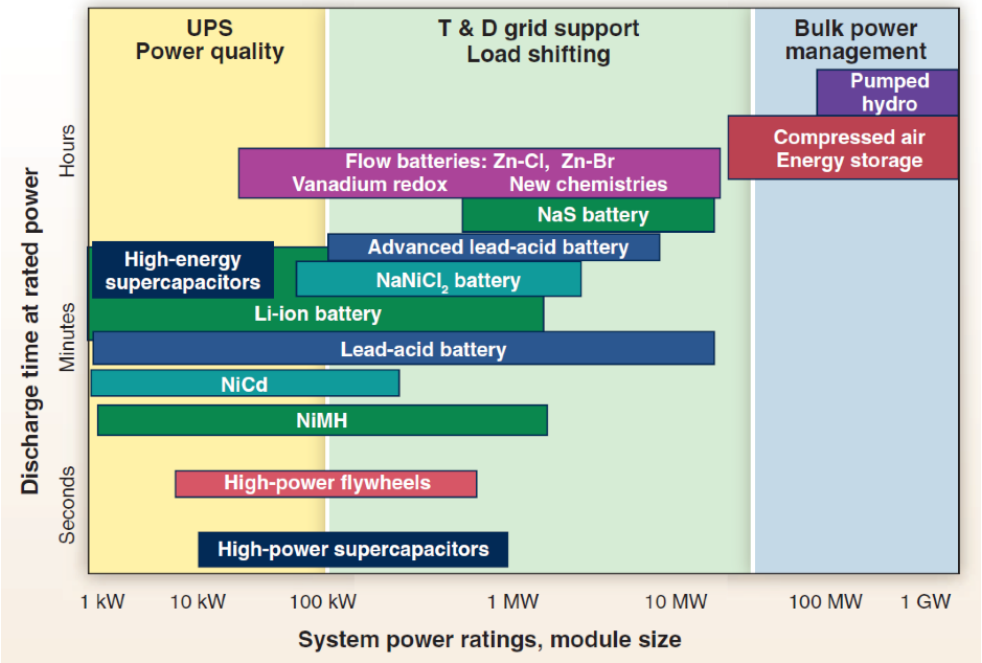

Figure 4.1: Comparison of several energy storage systems [11]

ficiency, flexible power and energy characteristics for different applications, long cycle life and low maintenance make them excellent energy storage systems [11].

Historically, the energy storage systems based on the technologies we have are very expensive. Table 4.1 summarizes some information about energy and power characteristics of different types of batteries being considered for grid energy storage applications. Table 4.2 also gives the approximate cost of different battery types.

As can be seen in Table 4.1, Li-ion batteries exhibit high specific energy and specific power. A Li-ion battery is based on the use of Li-intercalation materials. They benefit from high output voltages, a long cycle life and rate capability. The good cycling stability of Li-ion batteries is attributed to their ability to be reversibly intercalated into or deintercalated from electrodes without destroying the structure of the electrode material [11, 2].

Table 4.1: Energy and power characteristics of different types of batteries [11].

Battery Type	Voltage Range (V)	Energy Density (Wh/L)	Specific Energy (Wh/kg)	Specific Power (W/kg)	Cycleability
Lead acid	2.1 – 1.8	60 – 75	30 – 40	60 – 110	100 – 500
Nickel-Cadmium	1.3 – 0.8	130 -150	40 – 60	40 – 100	2000
Nickel-Metal Hydride	1.3 – 0.9	250 – 330	70 – 100	70 - 200	1000
Lithium Ion – $\boldsymbol{LI(TM)O_2}$– C TM = Ni, Co, Mn	4.2 – 2.5	200 – 250	120 – 160	200 – 300	300 - 1000
Lithium Ion - $\boldsymbol{LiFePO_4}$ – C	3.5 – 2.5	120 – 150	80 - 90	200 – 300	1500–2000
Lithium Metal- Polymer	4.0 – 2.4	100 – 110	100 – 110	130 – 170	600
Sodium- Sulfur	2.1 – 1.8	70 – 150	60 – 120	15 – 70	4000
Sodium-Metal Chloride	2.6	20 - 140	50 - 100	30 – 150	3000
Vanadium Redox Flow	1.6 – 1.1	10 – 20	10 – 20	1 – 4	5000

Table 4.2: The cost of various energy storage systems [11].

Technology option	Maturity	Capacity (MWh)	Power (MW)	Duration (hours)	% Efficiency (total cycles)	Total cost ($/kW)	Cost ($/kWh)
Compressed air Energy storage	Demo	250	50	5	(>10,000)	1950-2150	390-430
Advanced Pb-acid	Demo	3.2-48	1-12	3.2-4	75-90 (4500)	2000-4600	625-1150
Na/S	Commercial	7.2	1	7.2	75 (4500)	3200-4000	445-555
Zn/Br flow	Demo	5-50	1-10	5	60-65 (>10,000)	1670-2015	340-1350
V redox	Demo	4-40	1-10	4	65-70 (>10,000)	3000-3310	750-830
Fe/Cr flow	R&D	4	1	4	75 (>10,000)	1200-1600	300-400
Zn/air	R&D	5.4	1	5.4	75 (4500)	1750-1900	325-350
Li-ion	Demo	4-24	1-10	2-4	90-94 (4500)	1800-4100	900-1700

4.2 Organic electrolytes benefits and challenging issues

The organic electrolytes used in Li-ion batteries provide a large operating voltage window, enabling the use of electrodes with a large difference in chemical potential and so producing high energy density battery. Furthermore, the liquid electrolytes have the ability to form a good contact with electrodes and allow the development of nanostructured electrodes in order to benefit from their high specific surface area. Moreover, compatible organic electrolytes and electrodes can form a stable solid-electrolyte interface (SEI) and thus further improve the cycleability of the cell. These attractive properties have enabled them to be extensively used in portable electronic devices. Li-ion batteries have also been used in hybrid electric and electric vehicles [11].

Although a long life cycle, high energy density, safety and low cost are all essential in developing batteries for different applications, their importance differs from case to case. For large-scale energy storage systems, emphasis is more on cost and less on energy density. A long cycle life is another essential for grid applications [11].

Despite all the positive properties of Li-ion batteries, cost-effectiveness, safety, and super-fast charging performance are challenging issues that must be resolved for large-scale energy-storage applications [2, 8]. Organic electrolytes are toxic, flammable and expensive. They also require the use of expensive separators, especially for high power and high energy batteries. Furthermore, the strict fabrication process is costly because it necessitates using a glove box to avoid the reaction between moisture and organic electrolyte [2, 8].

Various causes such as overcharging, overheating or short circuiting may cause thermal runaway, fire or explosion of Li-ion batteries made with organic electrolytes. To avoid thermal runaway, Li-ion batteries must come with a protective battery management system that controls the temperature and cooling system. This additional requirement increases the cost of batteries [2].

4.3 Aqueous electrolytes

Water-based electrolytes have been used in commercially available secondary batteries, e.g., Pb-acid, nickel-cadmium (Ni-Cd) and nickel-metal hydride (Ni-MH), for a long time. But none of them have as long a cycling stability as Li-ion batteries with organic electrolytes [11, 2, 8]. The Pb-acid batteries suffer from low cycleability and low energy density [11, 2]. In addition, lead is a toxic element. Likewise, Ni-MH batteries degrade rapidly, which hinders their utilization for large scale energy storage. The cadmium used in Ni-Cd batteries is also toxic [2].

The first aqueous rechargeable lithium ion battery was demonstrated by Dahn's group in 1994, pairing $LiMn_2O_4$ and VO_2 in concentrated lithium nitrate [32, 31, 30]. The cell had a specific energy density of 75 $W\ h\ kg^{-1}$ (based on the total weight of both electrode materials), operating at an average voltage of $\sim 1.5V$. Since then, several aqueous rechargeable lithium ion batteries (ARLBs) have been developed using various intercalating host materials. Early ARLBs suffered from fast capacity loss during cycling and so their performance developments were very limited [2, 8]. But since 2007, ARLBs using cathode electrode materials from commercial Li-ion batteries have attracted extensive attention, because of their low cost, safety and environmental friendliness [8].

The potential range for intercalation of the cathodes and anodes in ARLBs must lie within the electrochemical stability window of the aqueous electrolyte. Pure water is electrochemically stable within a potential window of 1.23 V. [2]. However, usually kinetic effects significantly hinder water decomposition beyond the stability window so that aqueous electrolytes may operate in a larger voltage window without dramatic decomposition of the electrolyte. For instance, Pb-acid batteries operate in a $\sim 2V$ voltage window [2, 49] owing to the high overpotential needed for hydrogen evolution on the surface of Pb as well as the electronically insulating but ionically conductive nature of $PbSO_4$ [10].

4.3.1 Aqueous electrolytes benefits

Aqueous electrolyte solutions reduce the cost of Li-ion batteries by replacing expensive salts like $LiPF_6$ with cheap salts such as $LiNO_3$, $LiOH$, and Li_2SO_4. Furthermore, expensive separators can be replaced with cheaper ones appropriate for aqueous electrolytes and a glove box is not necessary in the fabrication process [2, 8].

Since water has a very high thermal capacitance, the use of aqueous electrolyte for Li-ion batteries offers a natural solution to the thermal runaway problem: water is in direct contact with the electrodes and absorbs a large amount of heat, acting as a cooling system. Thus, the temperature of the system will be kept lower than that in commercial Li-ion batteries with organic electrolytes [2]. Moreover, aqueous electrolytes are not flammable.

Another benefit of aqueous electrolytes is their ionic conductivity, which is almost two orders of magnitude higher than that of organic electrolytes [2, 8, 49]. Therefore, the ARLBs can be made using thicker electrodes. In addition, the interfacial charge transfer resistance at the surface of an electrode and aqueous electrolyte is lower than the one at the surface of an electrode and organic electrolyte. This phenomenon is due to smaller activation energy needed for interfacial Li^+ ion transfer reactions in aqueous electrolytes compared to that in organic electrolytes [2, 49]. Thus, ARLBs exhibit lower cell resistance compared to Li-ion batteries with organic electrolytes. Lower cell resistance is essential for high-power battery production. In support of this fact, cyclic voltammetry experiments show that the current response and reversibility of $LiMn_2O_4$ electrode in an aqueous electrolyte solution is better than those in organic electrolyte ones, indicating great promise for super-fast charge and discharge capabilities [8, 43].

4.3.2 Aqueous electrolytes challenging issues

Despite all the benefits of aqueous electrolytes, challenges in using them in batteries must be resolved. In general, the chemical and electrochemical mechanism of the active materials in aqueous electrolytes is much more complex than that in organic electrolytes [2, 33].

The performance of the ARLBs is influenced by many side reactions, including those of the electrode material with water or oxygen, hydrogen and oxygen evolution reactions, proton intercalation into the electrode material alongside that of Li^+ and the dissolution of electrode materials in the electrolyte [2, 8, 49, 33].

The first problems with the use of aqueous electrolytes are hydrogen and oxygen evolution. As mentioned previously, aqueous electrolytes have a thermodynamic stability window of 1.23V. Figure 4.2 shows the intercalation potential of some electrode materials and the electrochemical stability window of an aqueous solution with $1M$ Li_2SO_4 at different pH values. If the intrinsic intercalation potential of a Li^+ ion inside the cathode active material exists above or around the oxygen evolution level, O_2 evolution inevitably occurs. In the same way, if the intrinsic intercalation potential of a Li^+ ion inside the anode is below or around that of hydrogen evolution, H_2 evolution inevitably occurs. Due to these reactions, the pH value close to the electrodes will change, usually influencing the stability and performance of the active material [49]. Although the decomposition of electrolyte materials in organic electrolyte solutions is also reported [49], the formation of a protective layer (an SEI layer) on the surface of the active material due to the decomposition of some of the organic electrolytes will prevent further decomposition of the electrolyte. However, with aqueous electrolytes this is not the case; the decomposition products of aqueous electrolytes are gases, which cannot form a protective layer on the surface of the active material [49].

Usually, materials for ARLB cathodes are more stable than the anode materials in aqueous solutions. A variety of materials such as $LiCoO_2$, $LiMn_2O_4$, and $LiFePO_4$ can be used as the cathodes in ARLBs. The spinel $LiMn_2O_4$ is considered an excellent candidate because of its low cost, high stability and electrochemical performance in water-based electrolytes [8].

As for ARLB anode, materials such as vanadium oxide, molybdenum oxide and some other intercalation compounds have been used. However, finding suitable negative electrodes has been more challenging due to dissolution of the active material inside the aque-

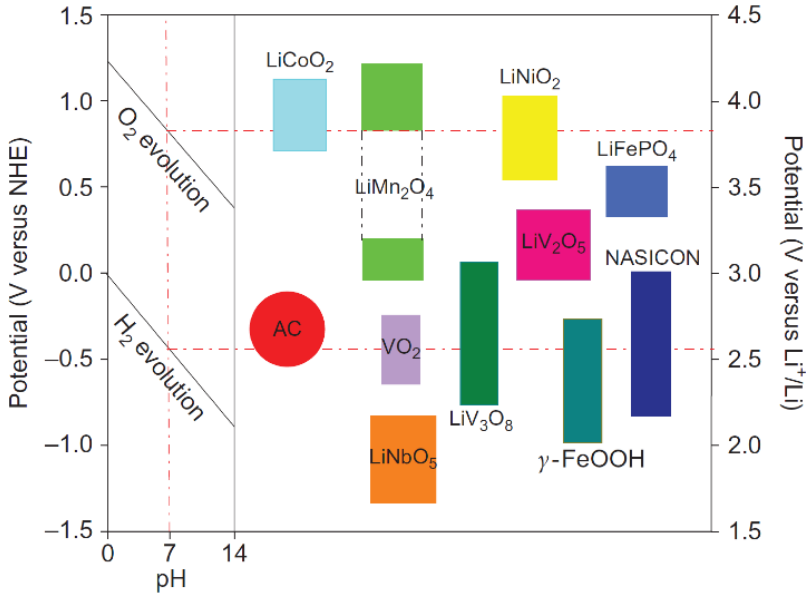

Figure 4.2: The intercalation potential of some electrode materials and the stability voltage window of an aqueous solution with $1MLi_2SO_4$ at different pH values [33]

ous electrolyte [8, 33] and the reaction with oxygen and water [33]. Basically, the negative electrode materials with a voltage of greater than 3.3V versus Li/Li^+ are stable in a water-based environment. However, the intercalation potential of Li^+ is generally lower than 3.3V versus Li/Li^+. Thus, the full intercalated anode material will be oxidized by the presence of water or oxygen [49, 33].

Theoretical studies have been done to investigate the stability conditions of intercalating compound in aqueous electrolytes. In the first theoretical attempt, Dahn's group [32] investigated the equilibrium conditions of an intercalation compound immersed in water. Assuming that the intercalation compound $Li_x(Host)$ contains lithium at some electrochemical potential of $\mu_{Li}^{int}(x)$, it was shown that the voltage $V(x)$ of a cell versus Li/Li^+ can be given by

$$V(x) = -\frac{1}{e}(\mu_{Li}^{int}(x) - \mu_{Li}^{0}) \tag{4.1}$$

where μ_{Li}^{0} is the chemical potential of Li in lithium metal, e is the electric charge of an

electron and x is the fraction of intercalated Li^+ to the total capacity of the compound. They assumed no significant change in x occurs when the compound reacts with water so that $\mu_{Li}^{int}(x)$ does not vary. During the reaction of the compound and water, some Li^+ deintercalates from the compound and dissolves in water, raising the pH as more OH^- forms. Eventually, if the compound is stable in water, the system must reach equilibrium at a certain pH value. In the absence of oxygen, the following equilibrium reaction is presumed to hold:

$$Li(intercalated) + H_2O \rightleftharpoons Li^+ + OH^- + \frac{1}{2}H_2 \tag{4.2}$$

If hydrogen and water are at standard state, the chemical potentials must satisfy the following equation when equilibrium is reached:

$$\mu_{Li}^{int}(x) + \mu_{H_2O}^0 = \mu_{OH} + \mu_{Li^+} + \frac{1}{2}\mu_{H_2}^0 \tag{4.3}$$

where $\mu_{H_2O}^0$ and $\mu_{H_2}^0$ are the chemical potential of water and hydrogen in their standard states, respectively, and μ_{OH} and μ_{Li^+} are the chemical potentials of OH^- and Li^+ in solution, respectively. Considering that compound is initially added to pure water, then

$$[Li^+] \cong [OH^-] \tag{4.4}$$

The chemical potentials of OH^- and Li^+ in solution are given by Nernst equation, i.e.

$$\mu_{Li^+} = \mu_{Li^+}^0 + kT\ ln[Li^+] \tag{4.5}$$

$$\mu_{OH} = \mu_{OH}^0 + kT \ln[OH^-] \tag{4.6}$$

where μ_{OH}^0 and $\mu_{Li^+}^0$ are the chemical potentiasl of OH^- and Li^+ in $1M$ solution, respectively. k is the Boltzmann's constant and T is the temperature in Kelvin. Therefore,

$$2kT \ln[OH^-] = \mu_{Li}^{int}(x) + \mu_{H_2O}^0 - \mu_{OH}^0 - \mu_{Li^+}^0 - \frac{1}{2}\mu_{H_2}^0 \tag{4.7}$$

At 25℃, $kT = 0.0257eV/atom$, and the pH is given by

$$pH = -\log[H^+] = 14 + \log[OH^-] \tag{4.8}$$

Thus we find that

$$0.118pH = 1.657 + \mu^{int}_{Li}(x) + \mu^0_{H_2O} - \mu^0_{OH} - \mu^0_{Li^+} - \frac{1}{2}\mu^0_{H_2} \tag{4.9}$$

Combining Equation 4.1 and Equation 4.9 gives

$$0.118pH = 1.657 - e\ V(x) + \mu^0_{Li} + \mu^0_{H_2O} - \mu^0_{OH} - \mu^0_{Li^+} - \frac{1}{2}\mu^0_{H_2} \tag{4.10}$$

From the partial molar energy change in the reaction of lithium metal with water in the standard state, i.e.

$$Li_{(s)} + H_2O \rightarrow LiOH_{(aq,1M)} + \frac{1}{2}H_{2(g,STP)} \tag{4.11}$$

we know

$$\mu^0_{Li} + \mu^0_{H_2O} - \mu^0_{OH} - \mu^0_{Li^+} - \frac{1}{2}\mu^0_{H_2} = 51.23\ kcal/mol = 2.228\ eV/atom \tag{4.12}$$

Thus,

$$V(x) = 3.885 - 0.118pH \tag{4.13}$$

Equation 4.13 indicates that if $Li_x(Host)$ immersed in water has voltage $V(x)$ vs Li, it will react and the pH will rise to the amount given by Equation 4.13 when equilibrium is re-established. For example, $LiMn_2O_4$ which has a potential of $\sim 4V$ vs Li does not react with water; that is, the deintercalation of Li^+ will not occur. While $Li_2Mn_2O_4$ which has $V = 2.97V$ vs Li metal, is stable in a solution of $LiOH$ with a pH greater than 8. This result shows that a high concentration of $LiOH$ may increase the stability of the host material [32].

In the same way, J.-Y. Luo et al.[33] investigated the stability of host intercalating material in the presence of oxygen. In the presence of water and oxygen, the following reaction may occur:

$$Li(intercalated) + \frac{1}{4}O_2 + \frac{1}{2}H_2O \rightleftharpoons Li^+ + OH^- \tag{4.14}$$

They considered that the intercalating host material is in contact with an aqueous electrolyte containing 2M of Li^+; i.e. $(Li^+) = 2M$. For this case they derived the following equation for the equilibrium condition

$$V(x) = 4.268 - 0.059pH \tag{4.15}$$

According to Equation 4.15, no intercalating material can be used as the negative electrode for aqueous lithium ion batteries in the presence of O_2, regardless of the pH of the electrolyte because the Li^+ intercalation potential of the negative electrodes for aqueous Li-ion batteries is in general below 3V vs Li. The equilibrium voltage is 3.442V at a pH of 14 [33].

In the absence of oxygen, they considered reaction 4.2 to occur, for the same electrolyte containing 2M Li^+. The equilibrium equation with water is shown to be governed by

$$V(x) = 3.039 - 0.059pH \tag{4.16}$$

Comparing Equation 4.15 and Equation 4.16, one may conclude that by eliminating oxygen from a solution and adjusting its pH, some intercalating material with a potential above 2.2V vs Li metal may be made stable in aqueous electrolytes. J.-Y. Luo et. al. managed to improve the cycling stability of a aqueous Li-ion battery in Li_2SO_4 aqueous electrolytes by eliminating the oxygen adjusting the pH value of the electrolyte and carbon coating the electrode material [33]. The cell exhibited better stability in the absence of oxygen, with only 10% capacity loss after 1000 cycles at 6C, and 15% capacity loss at a very low current rate of C/8.

Since the stability and electrochemical performance of electrodes in aqueous electrolyte solution varies with pH, it may be challenging to find active materials as cathodes and anodes [2]. On the other hand, the type of salt used in aqueous electrolyte also affects the electrochemical performance of ARLBs. Thus electrodes in contact with different aqueous electrolytes may show different electrochemical performance even when the pH is the same [2].

The co-intercalation of protons into lithium host materials has been reported as another reason for the fading capacity of aqueous Li-ion batteries [49, 33]. In aqueous electrolytes, other cations such as protons may intercalate into the electrode materials. Significant concentrations of protons in the lattices of layered structures such as $LiCoO_2$ have been reported. In contrast, no sign of H^+ insertion has been seen in spinel $LiMn_2O_4$ and olivine $LiFePO_4$ crystal structures [49]. Further investigation using first principle calculations have confirmed that proton insertion is most favorable energetically in layered lattice structures, but less favorable in spinel structures and unfavorable in olivine ones [49]. The increase in the concentration of the intercalated H^+ increases the energy barrier for diffusion of Li^+ in the active material and may block the diffusion channels. This issue can be resolved by adjusting the pH to control proton intercalation [49].

Another problem is the dissolution of metal ions in aqueous electrolytes. For example, the dissolution of Mn from $LiMn_2O_4$ has been reported [8, 33]. Therefore, for many electrodes, less surface area is preferred in ARLBs since the dissolution of active material scales with the surface area [8, 33].

4.4 Hybrid aqueous batteries

The main disadvantage of aqueous electrolytes is that the output voltages of ARLBs are much lower than that of conventional Li-ion batteries. Thus, the energy density of ARLBs is lower than that of Li-ion batteries with organic electrolytes [2, 8]. On the other hand, as mentioned before, the choice of negative electrode material is challenging in ARLBs. To overcome this issue, protected lithium metal has been introduced as the anode in aqueous electrolyte [48]. The surface of lithium metal is first covered by a layer of polymer with an organic electrolyte. Then, a layer of lithium-super-ionic-conductor (LISICON) film is used on top of this polymer. These layers make the lithium metal stable in aqueous electrolytes by preventing direct contact between water and the lithium metal.

Another strategy is to use another kind of anode material rather than a lithium inter-

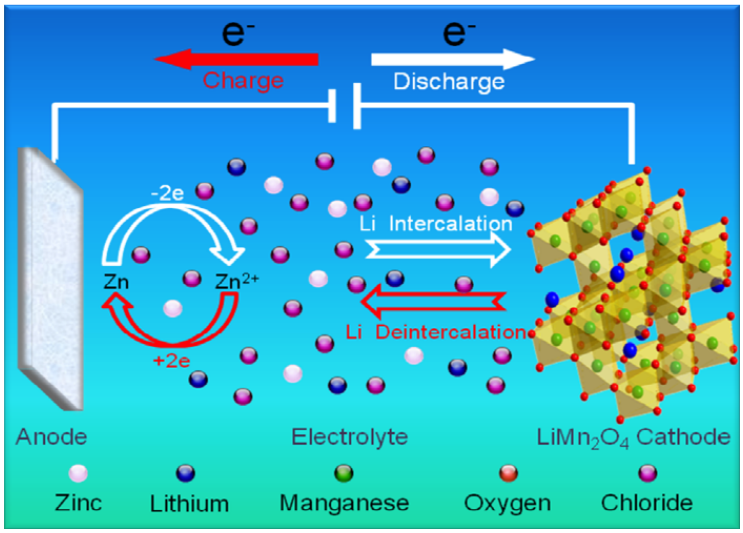

Figure 4.3: Schematic view of ReHAB. Taken from Ref. [52]

calating material. Thus, Li^+ may be eliminated from the anode electrochemical reactions, and other anions or cations in aqueous electrolyte may react on the anode side. For instance, metal anodes such as Zn and Sn have been used in ARLBs [36, 35, 37, 54]. These so-called hybrid batteries use two active ions (Li^+ and another ion such as Zn^{2+}) in the reversible electrochemical reactions. On the cathode side, the electrochemical reaction involves only the reversible intercalation into and deintercalation of Li^+ from an intercalating material; on the anode side, only the other ion is involved in the electrochemical reactions.

Prof. Chen's group has developed a rechargeable hybrid aqueous battery, the so called ReHAB, which consists of a $LiMn_2O_4$ electrode as the cathode and zinc metal as the anode [52]. The aqueous electrolyte solution contains a salt of lithium and another salt of zinc such as $LiCl/ZnCl_2$ or $Li_2SO_4/ZnSO_4$. Figure 4.3 represents a schematic of the ReHAB cell.

Chapter 5

Zinc Electrochemistry

Zinc ranks fourth among the most-used metals worldwide, after iron, aluminum, and copper [56]. Numerous applications of zinc, such as zinc batteries and zinc coatings and anodes for corrosion protection, are fundamentally based on electrochemical processes. Therefore, the electrochemistry of zinc has been the subject of research for a long time. Due to formation of a high corrosion resistance layer on the surface in the atmosphere and other environments, zinc is widely used in protective coating for steel structures, as it provides a barrier between the steel and the environment. Furthermore, if discontinuities in the coating occur, zinc provides a sacrificial anode that protects the steel from corrosion because of its position in the electromotive series of metals[56]. Zinc is also a favored anode material in various types of batteries such as Ni/Zn and zinc-air batteries, because of its reversible dissolution behavior in alkaline solutions and its well-placed position in the galvanic series [56].

5.1 Thermodynamic stability

Compounds of monovalent zinc do not naturally exist and zinc is divalent in all its compounds [56]. The radius of the zinc ion is 0.74-0.83 Å. Because of the electronic con-

Table 5.1: Zinc reactions in aqueous solutions and their equilibrium conditions [39, 56]

	Reaction	Standard potential or equilibrium condition
Two dissolved substances		
1	$Zn^{2+} + H_2O \rightleftharpoons ZnOH^+ + H^+$	$log(ZnOH^+/Zn^{2+}) = -9.67 + pH$
2	$ZnOH^+ + H_2O \rightleftharpoons HZnO_2^- + 2H^+$	$log(HZnO_2^-/ZnOH^+) = -17.97 + 2pH$
3	$Zn^{2+} + 2H_2O \rightleftharpoons HZnO_2^- + 3H^+$	$log(HZnO_2^-/Zn^{2+}) = -27.63 + 3pH$
4	$HZnO_2^- \rightleftharpoons ZNO_2^{2-} + H^+$	$log(ZnO_2^{2-}/HZnO_2^-) = -13.17 + pH$
Two solid substances		
5	$Zn + H_2O \rightleftharpoons ZnO + 2H^+ + 2e^-$	$E_0 = -0.439 - 0.0591\ pH$
One solid and one dissolved substance		
6	$Zn^{2+} + H_2O \rightleftharpoons ZnO + 2H^+$	$log(Zn^{2+}) = -10.96 - 2pH$
7	$ZnO + H_2O \rightleftharpoons HZnO_2^- + H^+$	$log(HZnO_2^-) = -16.68 + pH$
8	$ZnO + H_2O \rightleftharpoons ZnO_2^{2-} + 2H^+$	$log(ZnO_2^{2-}) = -29.78 + 2pH$
9	$Zn \rightleftharpoons Zn^{2+} + 2e^-$	$E_0 = -0.763 + 0.0295 \log(Zn^{2+})$
10	$Zn + 2H_2O \rightleftharpoons HZnO_2^- + 3H^+ + 2e^-$	$E_0 = 0.054 - 0.0886pH + 0.0295 \log(HZnO_2^-)$
11	$Zn + 2H_2O \rightleftharpoons ZnO_2^{2-} + 4H^+ + 2e^-$	$E_0 = 0.441 - 0.1182pH + 0.0295 \log(ZnO_2^{2-})$
Stability of water		
(a)	$H_2 \rightleftharpoons 2H^+ + 2e^-$	$E_0 = 0.000 - 0.0591pH$
(b)	$2H_2O \rightleftharpoons O_2 + 4H^+ + 4e^-$	$E_0 = 1.228 - 0.0591pH$

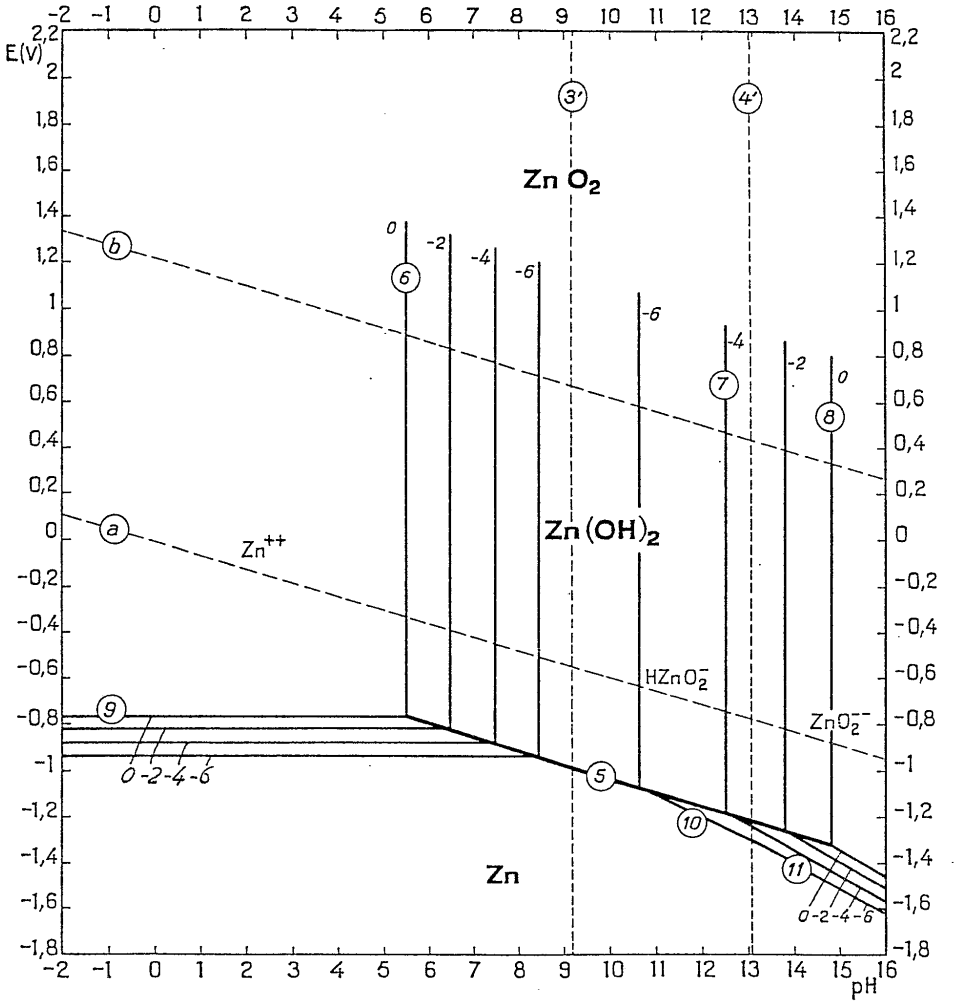

Figure 5.1: Potential-pH equilibrium for zinc-water system at 25°C [39, 56]

figuration of this atom, zinc ions have a tendency to form sp^3-hybridized tetrahedrally coordinated complexes in solutions. Thus, additional to Zn^{2+}, complexes of ZnX^{2-n}, ZnX_2^{2-2n}, ZnX_3^{2-3n}, and ZnX_4^{2-4n} may form, where X^{n-} is the complexing agent [56]. In particular, $Zn(OH)^+$, $Zn(OH)_2$, $Zn(OH)_3^-$, $Zn(OH)_4^{2-}$, $HZnO_2^-$, and ZnO_2^{2-} can form in aqueous solutions [39].

The equilibrium conditions of the chemical and electrochemical reactions of zinc and its compounds in aqueous solutions in the absence of complex formation are listed in Table 5.1, and represented by the Pourbaix diagram in Figure 5.1 [39, 56]. The equilibrium conditions of the reactions given in the table are represented by lines labeled to correspond with the reaction number. In particular, the equilibrium conditions for the reduction of water to gaseous hydrogen and the oxidation of water to gaseous oxygen are represented, respectively, by lines a and b, when the partial pressure of the gaseous phase is 1 atm at $25°C$. The Pourbaix diagram shown in Figure 5.1 is valid only in the absence of chemical species (other than OH^-) with which zinc can form soluble complexes or insoluble compounds.

According to Figure 5.1, zinc has no domain of stability in common with that of water. thus, over the entire pH range, the stable region of zinc metal is below the stability line of water represented by line a. Therefore, zinc is thermodynamically unstable in water and aqueous solutions and has a tendency to dissolve with the evolution of hydrogen. This reaction occurs extremely slowly when zinc is very pure due to the large hydrogen overpotential of zinc [39]. In fact, this large overpotential has made it possible not only to produce metallic zinc by the reduction of an aqueous solution of zinc salts, but also to use zinc as the anode material in various aqueous batteries.

In the region of moderately alkaline solutions of pH between approximately 8.5 and 12, a film of hydroxide can cover the surface of zinc metal, thus inhibiting further dissolution of zinc [39, 56]. Experimental results on the influence of pH on the corrosion rate of zinc, represented in Figure 5.3, indicate that the corrosion rate is actually minimum at these pHs.

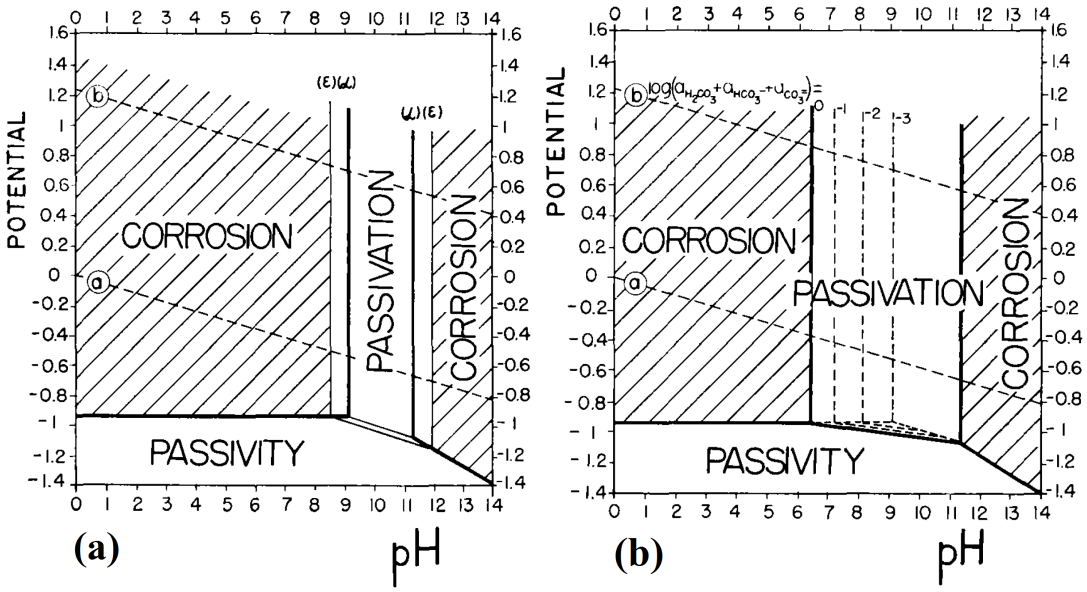

Figure 5.2: Theoretical conditions of corrosion, passivity and passivation of zinc, (a) for solutions free from CO_2, and (b) for solutions containing CO_2 [39]

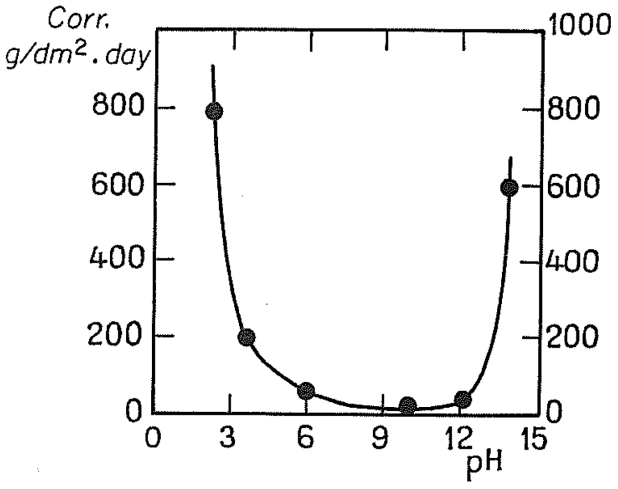

Figure 5.3: Influence of pH on the corrosion of zinc [39]

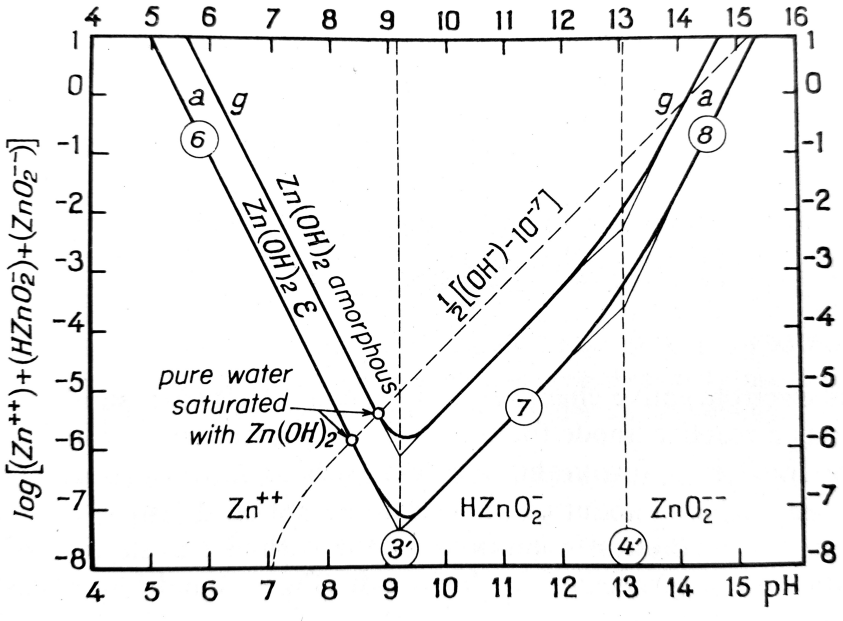

Figure 5.4: Influence of pH on the solubility of zinc hydroxides, at 25°C [39]

Zinc can react with many chemical agents to form insoluble compounds. In fact, the solubility of these complexes has been found to significantly affect corrosion resistance of zinc in many environments. Of particular importance, when zinc comes in contact with solutions containing carbonates and bicarbonates is the formation of zinc carbonate. Zinc carbonate is known to be responsible for the high corrosion resistance of zinc in an atmospheric environment [56]. Figure 5.2 represents the theoretical conditions of corrosion, immunity and passivation of zinc for the case in which the metal is passivated by a film of $\varepsilon - Zn(OH)_2$. Figure 5.2 represents these conditions for zinc in the presence of solutions containing bicarbonate [39].

The influence of pH on the solubility of zinc oxides and hydroxides is represented in Figure 5.4. The two curves (a) and (g) refer respectively to $\varepsilon - Zn(OH)_2$ and amorphous $Zn(OH)_2$, which are, respectively, the least soluble and the most soluble of the seven varieties of zinc hydroxides [39, 56]. Hydroxides dissolve in acidic solutions to produce

Zn^{2+} ions, and in moderately or highly alkaline solutions to produce $HZnO_2^-$ and ZnO_2^{2-}, respectively.

5.2 Kinetics of electrochemical reactions

Many studies have been dedicated to understanding the zinc electrochemical reaction processes such as dissolution, deposition, hydrogen evolution, passivation, etc. These studies are typically related to the most commercial application of zinc, i.e., galvanization and corrosion protection of steel.

5.2.1 Dissolution

The dissolution of zinc takes place near its equilibrium potential. The dissolution product is basically Zn^{2+} in acidic solutions. Different complexes may form in alkaline solutions; however, tetrahedral $Zn(OH)_4^{2-}$ has been identified as the predominant zinc species [56].

Many electrochemical studies have been performed to measure the exchange current density and Tafel slopes for zinc dissolution in various solutions. It has been observed that many factors affect the electrochemistry of zinc. For instance, in KOH solutions, the exchange current density of zinc increases with the KOH concentration, before reaching a maximum at a concentration of about $8M$ [56]. The type of species in the solution has also been found to be a potential factor affecting the dissolution process significantly. A solid film may or may not form during zinc dissolution depending on the type of species in the environment. These solid films may have different compositions and, thus, different morphologies and various degrees of compactness. On the other hand, dissolution may change the surface area, morphology and other properties of zinc electrode surfaces. In solutions containing no species with which zinc can form insoluble compounds, e.g., $NaCl$ and Na_2SO_4, the zinc electrode maintains a plain surface during dissolution at pH values below 3.8 [56]. At a higher pH value of about 5.8 in 3 M $NaCl$ or Na_2SO_4, an oxide film

covers the zinc electrode, affecting electrochemical processes, but this film is not passivating [56]. The solid surface films formed in solutions of carbonate, nitrate, and phosphate have been found to greatly inhibit the electrochemical processes of zinc electrodes [56].

The dissolution mechanism changes with the pH value and is different for complexing and non-complexing solutions. In non-complexing neutral solutions, the overall zinc dissolution reaction is

$$Zn \rightarrow Zn^{2+} + 2e^{-} \tag{5.1}$$

However, the reaction in Equation 5.1 is not a simple elementary reaction. The dissolution process has been reported to take place in two successive one-electron-charge-transfer steps [56], i.e.:

$$Zn \rightarrow Zn^{+}_{ads} + e^{-} \tag{5.2}$$

$$Zn^{+}_{ads} \rightarrow Zn^{2+} + e^{-} \tag{5.3}$$

where Zn^{+}_{add} is an unstable adsorbed ion or a solution-soluble intermediate. The reaction in Equation 5.3 is the rate-determining step. Because the reaction in Equation 5.2 is fast, the concentration of adsorbed intermediate is small at low overpotentials, and the zinc metal and adsorbed Zn^{+}_{add} are in pseudo-equilibrium. Thus, the overall reaction can be treated as a pseudo-one-step reaction. At high overpotentials, the concentration of adsorbed species is relatively high and, consequently, they contribute in the overall reaction rate [56]. This simple reaction scheme is also thought to occur in alkaline solutions or other electrolytes where zinc complexes can form. However, it is observed that the rate-determining step for zinc dissolution depends on the type of anions in the electrolyte [56].

Another reaction scheme (Equations 5.4-5.6) for zinc dissolution was proposed by Johnson et al. [25] to describe the mechanism of the dissolution in neutral solutions containing various anion species which are not reducible by zinc. The desorption of ZnO_{ads}, i.e., Equation 5.6, is the rate-determining step in this scheme, i.e.,

$$Zn + H_2O \rightleftharpoons Zn(OH)_{ads} + H^{+}_{sol} + e^{-} \tag{5.4}$$

$$Zn(OH)_{ads} \rightleftharpoons ZnO_{ads} + H^{+}_{sol} + e^{-} \tag{5.5}$$

$$ZnO_{ads} + H_2O \rightarrow Zn^{2+}_{sol} + 2OH^- \tag{5.6}$$

For zinc dissolution in chloride solutions, Cachet and Wiart [6] proposed the reaction scheme in Equations 5.7-5.10. The proposed mechanism involves two parallel paths. In the major autocatalytic reaction (Equation 5.8), Zn^+_{ads} acts as a catalyst. The chemical oxidation of zinc by electrolytes is considered as a side reaction, producing $Zn(OH)_{ads}$ in Equation 5.10.

$$Zn \rightleftharpoons Zn^+_{ads} + e^- \tag{5.7}$$

$$Zn^+_{ads} + Zn \rightarrow Zn^+_{ads} + Zn^{2+}_{sol} + 2e^- \tag{5.8}$$

$$Zn^+_{ads} \rightarrow e^- + Zn^{2+}_{ads} \rightarrow Zn^{2+}_{sol} \tag{5.9}$$

$$Zn(OH)_{ads} \rightleftharpoons Zn(OH)^+_{sol} + e^- \tag{5.10}$$

Cachet et al. [5] investigated zinc dissolution in aerated sulfate medium with a pH value of 5.5. They used a reaction scheme involving two different paths of dissolution given by reactions in Equations 5.7-5.9. Furthermore, they included a chemical reaction between zinc and water before the reaction 5.10 to produce a third path way of zinc dissolution. The zinc-water reaction was given by:

$$Zn + H_2O \rightarrow Zn(OH)_{ads} + 1/2H_2 \uparrow \tag{5.11}$$

Several reaction mechanisms for zinc dissolution in alkaline solutions have been proposed [56]. However, the details of those studies are beyond the scope of this research, which focuses on the electrochemical mechanism of zinc electrodes in acidic solutions. In this part of the thesis, we attempt to model and analyze the zinc anode in a ReHAB battery system, in which the aqueous electrolyte contains $ZnSO_4$ and Li_2SO_4 salts, at pH 4.

It worth emphasizing that, in different experiments, the dissolution of zinc can follow different mechanisms depending on the experimental conditions. The differences in mechanisms essentially arise not only with respect to the final dissolution products and their properties, but also the type and numbers of intermediate species and their physicochemical properties, e.g., their state of adsorption and solvation [56].

5.2.2 Deposition

Zinc deposition and hydrogen evolution both occur at potentials negative to the zinc reversible potential in aqueous solutions. At these negative potentials (vs Zn/Zn^{2+} potential), hydrogen evolution is, thermodynamically, more favoured due to its more positive equilibrium potential. However, when the concentration of zinc species in an electrolyte is higher than $10^{-4}M$, zinc deposition occurs near its reversible potential and is kinetically more facile than hydrogen evolution. This is due to a large Tafel slope and the small exchange current density of hydrogen evolution on zinc surfaces [56].

Wiart and coworkers [13] proposed that the deposition of zinc in acidic sulfate involves the formation of adsorbed species of H_{ads}, Zn^{+}_{ads} and anions. The monovalent intermediate is also presumed to be involved in a self-catalytic step. Furthermore, the presence of H_{ads} is also considered as another possible catalytic site for zinc deposition. Their proposed scheme of reactions is summarized in Equations 5.12-5.18. The adsorption of H_{ads} acts as an inhibitor for zinc deposition by competing for surface sites. The authors ignored the reverse reactions in their calculations, except for the autocatalytic reaction of Zn^{+}_{ads} and adsorption of the anion.

$$H^{+} + e^{-} \rightarrow H_{ads} \tag{5.12}$$

$$H^{+} + H_{ads} + e^{-} \rightarrow H_2 \tag{5.13}$$

$$Zn^{2+} + Zn^{+}_{ads} + e^{-} \rightleftharpoons 2Zn^{+}_{ads} \tag{5.14}$$

$$Zn^{+}_{ads} + H_{ads} \rightarrow Zn + H^{+} \tag{5.15}$$

$$Zn^{+}_{ads} + e^{-} \rightarrow Zn \tag{5.16}$$

$$Zn^{2+} + H_{ads} + e^{-} \rightarrow Zn^{+}_{ads} + H_{ads} \tag{5.17}$$

$$Zn + A^{-} \rightleftharpoons ZnA_{ads} + e^{-} \tag{5.18}$$

In another study, Wiart and coworkers [14] removed Equations 5.17 and 5.18 from the reactions scheme, and proposed the following elementary steps:

$$Zn^{2+} + e^{-} \rightarrow Zn^{+}_{ads} \tag{5.19}$$

$$Zn^{+}_{ads} + e^{-} \rightarrow Zn^{*} \tag{5.20}$$

$$Zn^{*} + Zn^{2+} + 2e^{-} \rightarrow Zn + Zn^{*} \tag{5.21}$$

$$Zn^{*} \rightarrow Zn \tag{5.22}$$

They proposed that the Zn^{*} sites attributed to the growth steps of a perfect lattice, form through the reaction represented in Equation 5.20. These sites act as catalysts via Equation 5.21, which is a two-electron-transfer reaction. Equation 5.22 is related to the possibility that some Zn^{*} may lose its activity. Furthermore, they assumed that the adsorbed Zn^{+}_{ads} is weakly linked to the metal and is able to diffuse along the electrode surface.

In another study of zinc deposition in concentrated chloride electrolyte, Ganne et al. [17] (Cachet and Wiart group) used the same scheme of reactions, but disregarded the auto-catalytic reactions of Zn^{+}_{ads} and H_{ads} (Equation 5.14, Equation 5.17).

5.2.3 Hydrogen evolution

The hydrogen evolution reaction in aqueous solutions, in general, depends on the activity $a_{H^{+}}$ of hydrogen ions and the hydrogen gas partial pressure, p_{H_2}. Its reversible potential is given by

$$E_H = E^0_H - RT/2F \log p_{H_2} + RT/F \log a_{H^{+}} \tag{5.23}$$

where E^0_H is the standard hydrogen potential, which is conventionally set to zero.

The solubility of hydrogen gas in water has been found to be very low. At a hydrogen pressure of 1 atm, aqueous solutions contain approximately $0.8 \times 10^{-3} M$ H_2. The solubility of hydrogen as well as its diffusion coefficient, decreases with an increasing salt concentration in the aqueous solutions [56].

The Tafel slope and exchange current density for hydrogen evolution on zinc electrodes have been measured in various solutions. In most cases, the Tafel slope has a value of about 120 mV. In the presence of chloride, the Tafel slope increases to about 200 mV

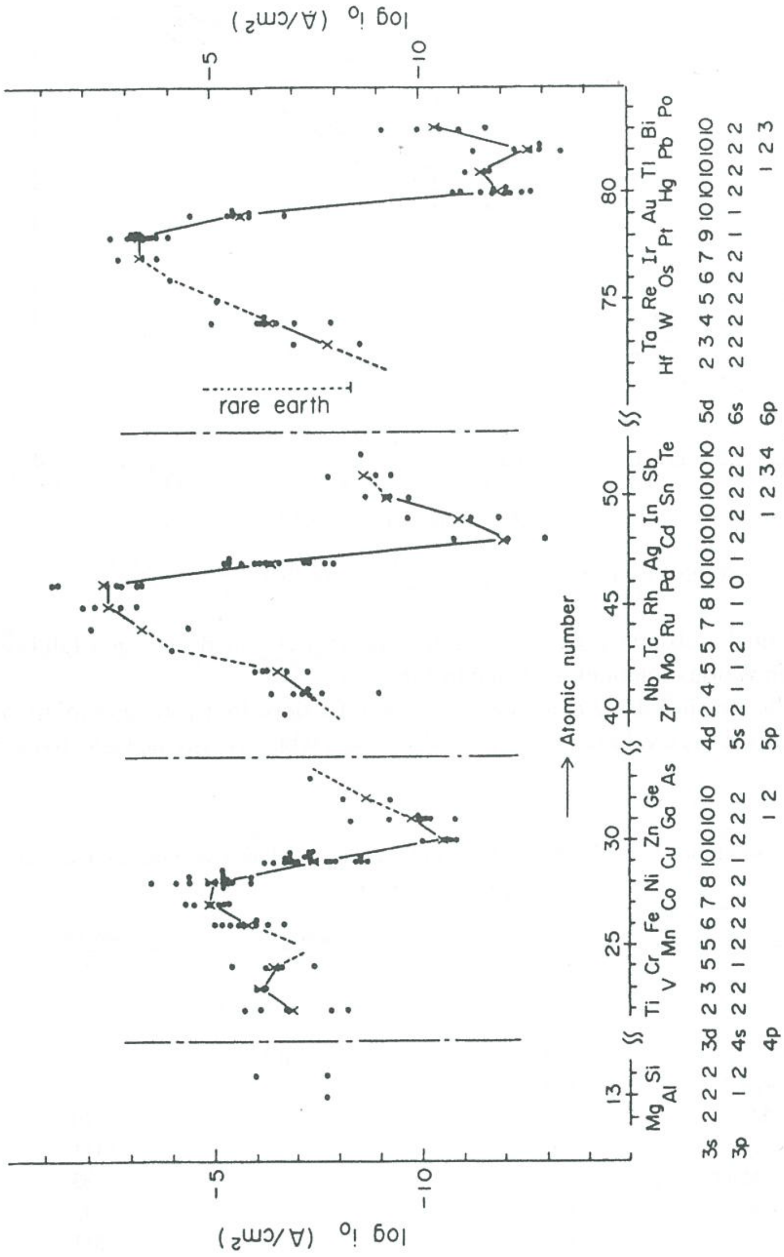

Figure 5.5: Values of hydrogen exchange current density, $\log i_0$, on various metals in acid solutions [27].

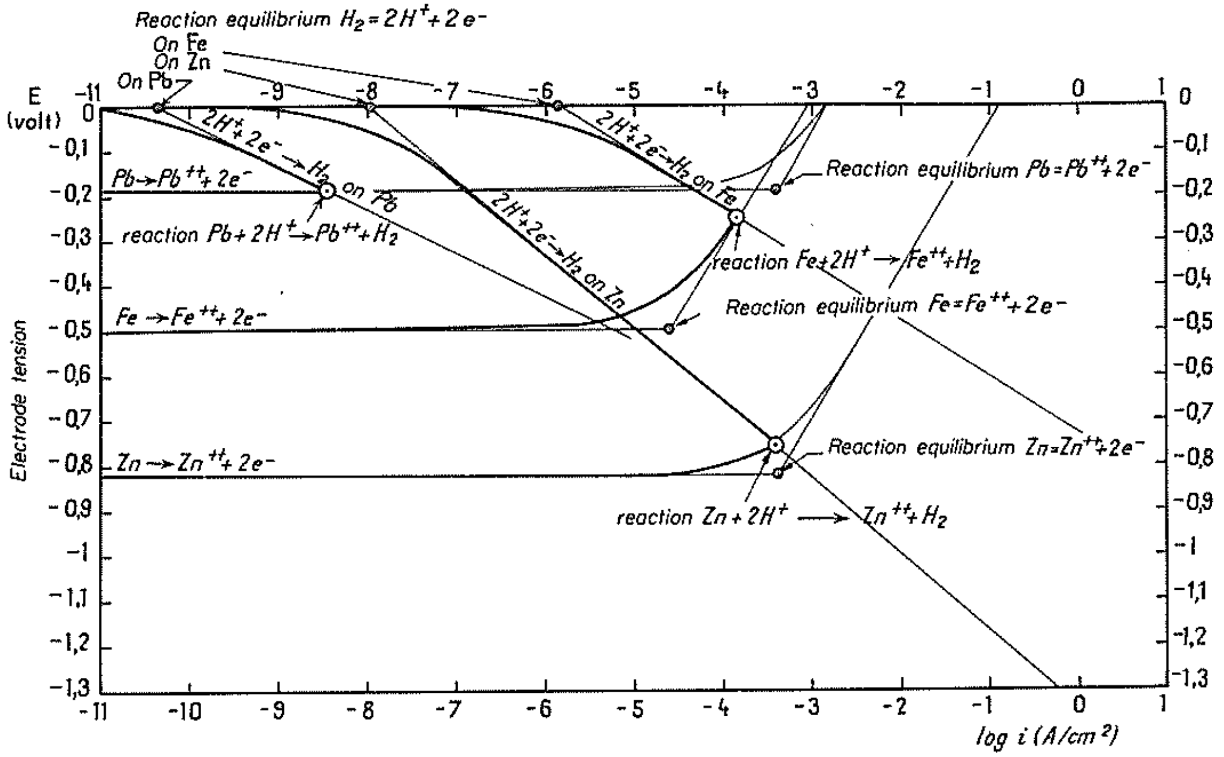

Figure 5.6: Corrosion of metals (Fe, Zn, Pb) with the evolution of hydrogen in the presence of a solution of $pH = 0$ containing 0.01 $mol/liter$ of dissolved metal [39].

[56]. The exchange current density of hydrogen evolution on zinc is found to be almost independent of pH, except for very acidic or basic solutions [56].

Figure 5.5 compares the exchange current density for hydrogen reaction on various metals. Based on the graph, the low exchange current density is the main reason for the high overpotential for hydrogen evolution on zinc, compared to that on the other metals. It has been proposed that the low exchange current density itself is the result of weak interaction between zinc and hydrogen [56].

For comparison, the characteristics of hydrogen evolution, metal dissolution, and overall corrosion reactions of Fe, Zn, and Pb are shown via Tafel graphs of the reactions in Figure 5.6. The metals are immersed in solutions of $pH = 0$ that contain 0.01 $mol/liter$

Table 5.2: Characteristics of hydrogen evolution, metal dissolution and corrosion of Fe, Zn and Pb in the presence of a solution with $pH = 0$ containing 0.01 mol/lit of dissolved metal [39].

	Fe	Zn	Pb
Characteristics of the hydrogen evolution reaction, i.e., $2\,H^+ + 2e^- \rightarrow H_2$			
Equilibrium potential ($E_0\ volt$)	0.000	0.000	0.000
Log exchange current $i_0(A/cm^2)$	-5.85	-7.95	-10.35
Tafel formula	$-0.72 - 0.123 \log i$	$-1.34 - 0.169 \log i$	$-0.74 - 0.0715 \log i$
Characteristics of the metal dissolution reaction, i.e., $M \rightarrow M^{2+} + 2e^-$			
Equilibrium potential ($E_0\ volt$)	-0.500	-0.822	-0.185
Log exchange current $i_0(A/cm^2)$	-4.60	-3.40	-3.40
Tafel formula	$1.49 + 0.328\ \log i$	$1.12 + 0.340\ \log i$	$0.80 + 0.246\ \log i$
Characteristic of the overall corrosion reaction, i.e., $M + 2\,H^+ \rightarrow M^{2+} + H_2$			
Corrosion affinity ($V/mol\ of\ M$)	0.500	0.822	0.185
Corrosion potential ($E_h\ volt$)	-0.250	-0.755	-0.185
Corrosion rate: $\log i\ \ (A/cm^2)$	-3.83	-3.43	-8.45
Corrosion rate: ($mm/year$)	80	166	0.003

of dissolved metal. The detailed information of the graph is gathered in Table 5.2 [39].

The overall hydrogen evolution reaction in acidic solutions can be described by the following equation:

$$2H_3O^+ + 2e^- \rightleftharpoons H_2 + 2H_2O \tag{5.24}$$

and in alkaline solutions by the following equation:

$$2H_2O + 2e^- \rightleftharpoons H_2 + 2OH^- \tag{5.25}$$

Furthermore, the charge transfer coefficient, α, remains almost consistent in acidic and

alkaline solutions, with a value of about 0.5. Thus, voltage polarization has the same influence on the electron-transfer reactions involving H_3O^+ and H_2O. Based on a Tafel slope of $120mV$ and a charge transfer coefficient of 0.5, it has been concluded that among the elementary steps of hydrogen evolution, namely,

$$H_3O^+ + e^- \rightarrow H_{ads} + H_2O \tag{5.26}$$

$$H_2O + e^- \rightarrow H_{ads} + OH^- \tag{5.27}$$

$$2H_{ads} \rightarrow H_2 \tag{5.28}$$

the charge transfer steps (Equations 5.26 and 5.27) are the rate-determining steps [56].

Depending on the electrolyte and overpotential, different processes may be involved in hydrogen evolution. For instance, it has been reported that in acidic solutions with a pH value of about 3.8, hydrogen evolution occurs via reduction at low overpotentials and water reduction at high overpotentials. Moreover, the presence of ions in the solution strongly affects hydrogen evolution. The presence of Fe^{2+}, Cu^{2+}, Ni^{2+}, As^{3+}, Sn^{2+} and Sb^{3+} has been found to promote hydrogen evolution on zinc, because these elements have more positive reversible potentials as well as lower hydrogen overpotentials than zinc. In contrast, Pb^{2+} ions act as hydrogen evolution inhibitors [56].

Chapter 6

Zinc Anode in ReHAB

As mentioned before, zinc is a favored anode material in batteries. However, to achieve reversibility, an electrolyte with a pH value either higher than 12 or lower than 6 must be used, because a passivating layer forms on the surface of the zinc in atmospheric environments with a pH value of approximately 6 to 12 (see Figures 5.2 and 5.3). Prof. Chen's group has used zinc in a rechargeable hybrid aqueous battery (ReHAB). $LiMn_2O_4$ performs as the cathode material. Because of the high lithium-intercalation-potential of $LiMn_2O_4$ (around 4V) the pH value of the aqueous solution must be sufficiently low to avoid decomposition of water and oxygen evolution. The aqueous electrolyte used in ReHAB contains two salts, i.e., Li_2SO_4 and $ZnSO_4$. During discharge, Li^+ ions intercalate into the cathode material and, at the same time, Zn^{2+} dissolves into the electrolyte, maintaining the charge neutrality of the electrolyte. In contrast, during charge, Li^+ ions deintercalate from the cathode to the electrolyte and zinc deposits on the zinc metal. Therefore, the concentrations of lithium and zinc ions in the solution vary dramatically during a cycle.

In this research, we focus on the electrochemistry of zinc during charge and discharge in ReHAB. Polarization of the anode was measured in three electrode cells. The experimental results were provided through the courtesy of Doan The Nam Long.

6.1 Experimental

6.1.1 Electrolyte, anode, and cathode preparation

The electrolyte solution used contains 1 M Li_2SO_4 (Sigma Aldrich, 99% purity) and 2 M $ZnSO_4$ (Alfa Aesar, 99% purity). The pH of the electrolyte was adjusted to 4.00 ± 0.05 by 1 M H_2SO_4 solution.

Commercial zinc foil (Rotometals, 99.6% purity) was polished using 0.3 μm polishing powder (Buehler) dispersed in de-ionized water and a nano-cloth (Buehler). The polished zinc foil was then washed with soap and deionized water, followed by rinsing with ethanol and drying at 60 $^{\circ}C$ under vacuum for 30 minutes. Disks of 12 mm-in-diameter were cut from the polished zinc foil and served as the zinc electrodes.

$LiMn_2O_4$ (MTI Co.), KS-6 (Timcal) and polyvinylidene fluoride (PVDF, Kynar) (86:7:7 wt.%) in n-methyl-2-pyrrolidinone (NMP, Sigma Aldrich Co.) were mixed thoroughly and then spread on graphite foil (Alfa Aesar) using Doctor Blade technique. After vacuum drying at 60 $^{\circ}C$ for 6 h, they were cut into disks of 12-mm-diameter (typical active material load of $5-6\ mg \cdot cm^{-2}$) and soaked in the electrolyte solution under reduced pressure before battery assembly.

6.1.2 Electrochemical characterizations

Polarization of the anodes and cathodes during the charge and discharge stages were investigated using three-electrode-Swagelok-type cells. Each cell was composed of a zinc metal negative electrode, a zinc metal reference electrode and a $LiMn_2O_4$/KS-6/PVDF composite positive electrode, separated by an Absorptive Glass Mat (AGM) separator. Four drops of liquid electrolyte were used to fully wet each separator (ca. 0.16 mL). The cells were tested galvanostatically with a multi-channel potentiostat (VMP3, Biologic) between 1.4 and 2.1 V at various charge-discharge current rates from 0.1 C to 4 C (1 C is defined

as 115 $mAh \cdot g^{-1}$). The potential of the positive and negative electrode vs. a zinc reference electrode were recorded. All electrochemical measurements were conducted at room temperature ($\sim 25\ ^{\circ}C$).

6.2 Results

Figure 6.1 show the polarization at the surface of a zinc anode during charge and discharge, in current rates of 0.2 C, 1 C and 4 C. The polarization curves exhibit a rather unusual profile. In the beginning of the charge of the cell, a negative overvoltage forms on the surface, forcing the electrochemical reactions to begin; thus, the anode voltage drops. However, it reaches a minimum and then increases back to a smaller negative overvoltage, and remains nearly constant until the end of charge process. This behavior is well-known in the deposition of zinc and some other metals, and has been accounted as the result of the activation and self-catalytic effect on the metal surface [50].

However, a close investigation reveals that the time scale of this phenomenon is of the order of an hour ($2500 - 3000 sec$) at discharge rate of 0.2 C, or ∼10 min in 1C; that is, almost 1/6 of the discharge duration time. Such a slow chemical/electrochemical process is quite surprising, since typical electrochemical reactions, in much shorter time scale, reach a quasi-steady-state of balance of species involved in the process. Astonishing as it may seem, the voltage reaches a minimum very slowly and remains at this level for a long time. These observations indicate that the self-catalytic effect is not a simple chemical or electrochemical reaction, and a complex scheme of reaction must account for that process. In particular, the large time scale of the relaxation process discloses the competition of different chemical/electrochemical reactions on the surface of zinc, as well as a large difference in the time scale of the reactions involved.

The discharge voltage profile at 4C is different from the ones at 1C and 0.2C. After the minimum at the beginning, since the self-catalytic effect is not fast enough to reach the quasi-steady-state, polarization decreases almost monotonically during discharge.Polarization

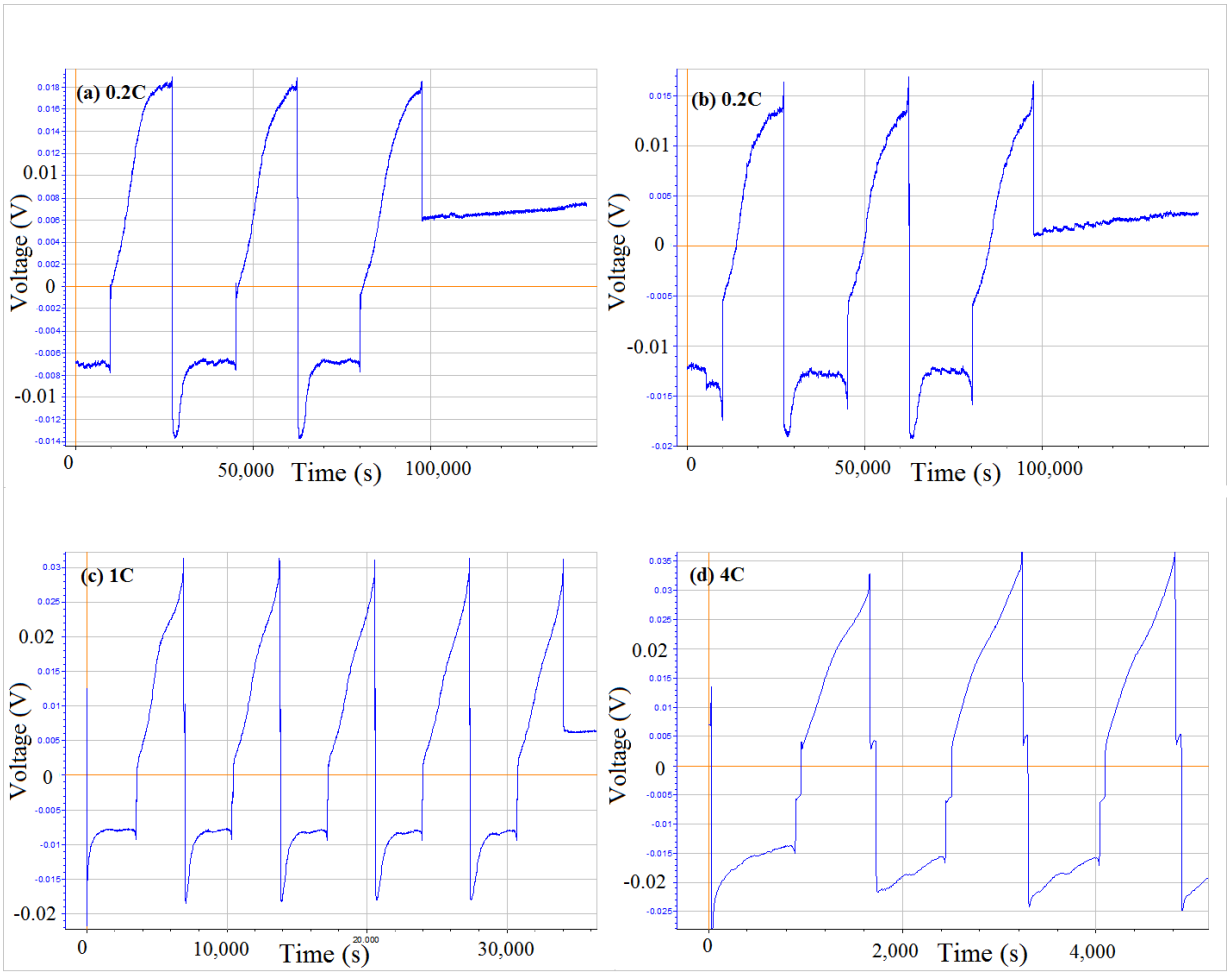

Figure 6.1: Polarization of zinc anode during charge and discharge of ReHAB with current rates of (a) 0.2C, (b) 0.2C, (c) 1C and (d) 4C.

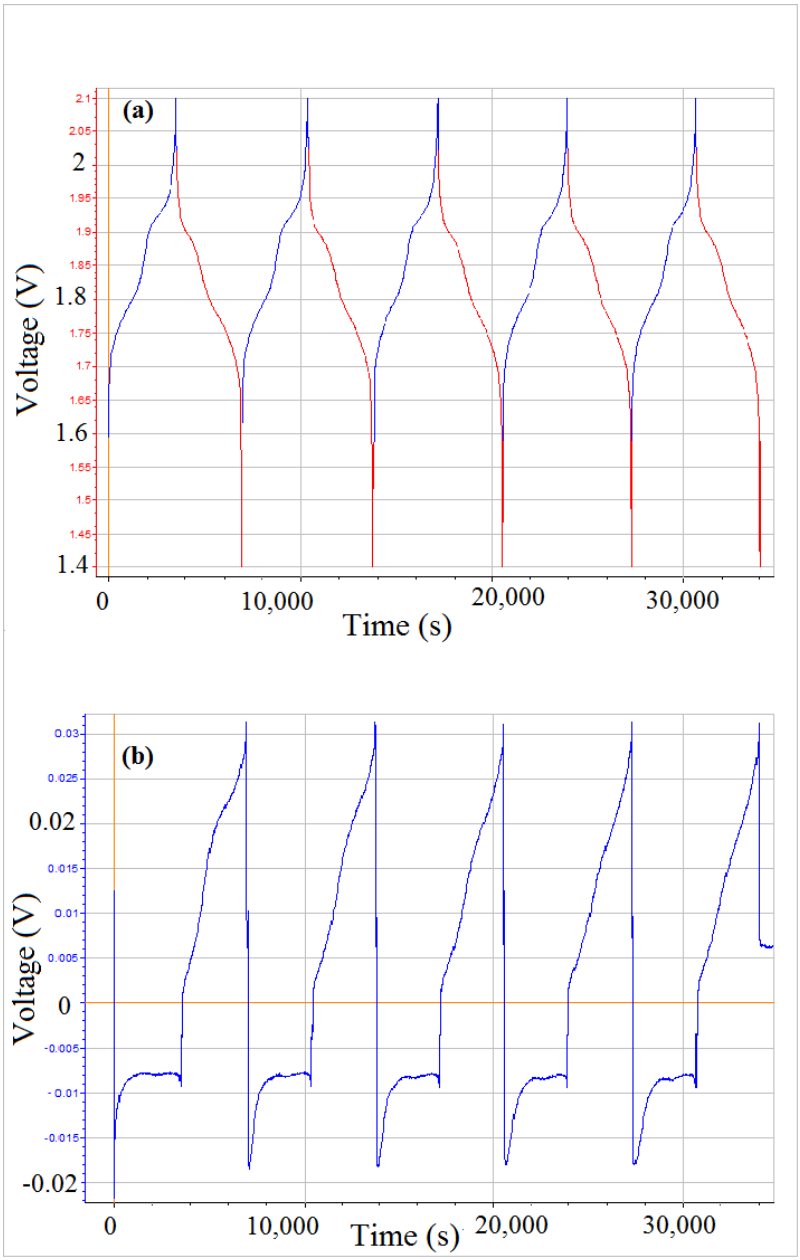

Figure 6.2: Voltage of (a) cathode and (b) anode vs reference electrode during charge and discharge at current rate of 1C.

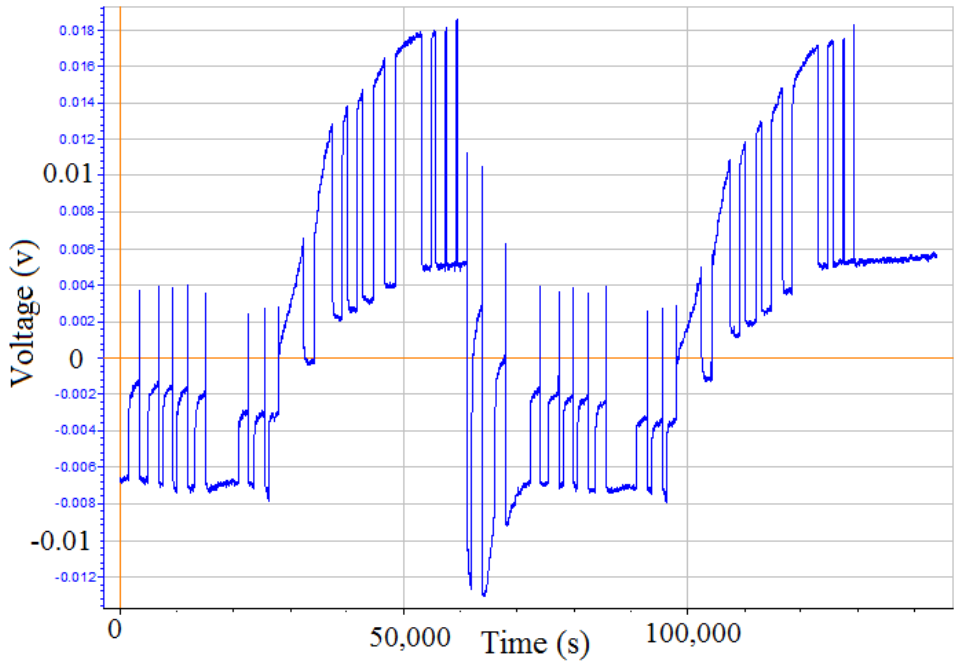

Figure 6.3: Measuring OCV of zinc anode vs reference electrode during charge and discharge in ReHAB.

during discharge displays an approximately linear increase at all the current rates. Thus, discharge overvoltage is almost proportional to the time since the discharge began. Only at 0.2C does a sign of a quasi-steady state appear. Typically, based on the Nernst equation, in electrochemistry, overvoltage is expected to change by $\log t$ due to increase of the concentration polarization.

Yet, once again, the zinc electrode charms us with his magic: the zinc electrode can see the polarization on the cathode side. The position of the phase-transition curves in the voltage plateau of the cathode matches the ones of the zinc polarization plateau (if one compares the voltage profile of anode and cathode at 1C). Furthermore, a sudden increase in the zinc polarization is observed at the end of both charge and discharge (here,

by "sudden", we mean compared to the whole time scale of charge or discharge; the actual process is of the order of minuets).

Although we have such an impressive experimental result, it should be noted that the accuracy of the experiment result is very low, as is obvious from the fluctuation in the voltage profile of the zinc. Therefore any attempt to interpret the experimental result must be done with extra caution.

It must be emphasized that the zinc metal which served as the reference electrode in these experiment is not an ideal reference electrode. Zinc metal is not at equilibrium with an aqueous electrolyte, i.e., zinc reacts continuously with protons and water, realizing hydrogen gas and producing soluble and insoluble species. Due to the corrosion of zinc, its surface morphology will change, and furthermore, the type and concentration of species adsorbed on the surface will vary over time. As a direct consequence, the polarization of the zinc metal and aqueous electrolyte varies over time, too. Therefore, zinc, as the reference electrode, has a memory. In other words, two zinc electrodes in contact with the same electrolyte may exhibit different polarization due to different history, in particular, if they have experienced a different current passing through the surface. This phenomenon is obvious in Figure 6.3 which presents the experimental result of Galvanostatic Intermittent Titration Technique (GITT). The GITT technique consists of a sequence of current pulses, each followed by a relaxation time, in which no current passes through the cell. We implemented this technique to measure the open circuit polarization of the zinc anode in respect to the zinc reference electrode during charge and discharge process. Even though both electrodes, presumably, are in same conditions, i.e., both are in contact with the same electrolyte, and no net current is passing through their surface, a non-zero OCV is observed, a value that depends on both time and the state of charge/discharge.

Last, but not least, one may realize that zinc polarization is of the order of only 10mV, which is even, by orders of magnitude, smaller than the overpotential of the cathode (vs reversible potential). The dynamic of an electrochemical reaction is given by the net rate

of forward and backward reactions via Butler-Volmer equation, i.e.,

$$i_0 \propto \left[A \exp\left(\alpha \frac{F}{RT}\eta\right) - B \exp\left(-\beta \frac{F}{RT}\eta\right)\right]$$

where η is the polarization in volts. Therefore, in the domain of the zinc polarization, the rates of forward and backward reactions (given by the exponentials in Butler-Volmer equations) remain of the same order. That means, in this domain, one has to consider both forward and backward reactions to explain the dynamics of the reactions. This requirement is in total contrast with the theoretical studies of the zinc electrode in the literature. We could not find any study considering reversible reactions in their modeling of zinc electrodes. To the best of our knowledge, most studies were performed for high current rates of charge or discharge, which is generally the case in commercial applications of zinc, for instance, in galvanization. A high current rate produces a large polarization on the surface of electrodes; as a consequence, one of the exponential terms in Butler-Volmer equations approaches zero, and thus can be neglected.

Reviewing the literature, we did not find any study related or close to our study, that is, using the same electrolyte and low current rate domain. In particular, no solution containing Li_2SO_4 appears to have been studied, whereas, Na_2SO_4 for example has been the subject of several studies.

6.3 Modeling attempts

The mathematical details of implementing a continuum model for a series of chemical and electrochemical reactions within the bulk electrolyte and at the interface of an electrode-electrolyte will be discussed in the next chapter. However, since the reaction scheme in the model is remarkably complex, we present the first few attempts made to model a zinc anode, which are far simpler than the final one. It is hoped that showing these steps will help clarify the scheme. As will be seen, a simple reaction scheme, when considered reversible cannot describe all aspects of a full anodic/cathodic cycle at low currents.

The numerical solutions were carried out using Mathematics module of COMSOL Multiphysics. Unfortunately, none of the kinetic parameters found in the literature could help to replicate the experimental overvoltage profile using this model (and also in next models). On the other hand, because of the large number of variables and nonlinearity of the model, which leads to numerous local minima in the model phase space, optimization methods for finding appropriate kinetic parameters for the model did not work. For these cases, even if, optimization would be possible, it is extremely time-and CPU-consuming. Matlabs Genetic optimization algorithm failed to find a close answer to the experimental result after a week of computation.

6.3.1 Simplest scheme of reactions

In the first attempt, the model only includes the very simple one-electron-transfer and autocatalytic reactions of the zinc along with the hydrogen evolution reactions, namely,

$$Zn \rightleftharpoons Zn^{+}_{ads} + e^{-}$$

$$Zn^{+}_{ads} \rightleftharpoons Zn^{2+}_{sol} + e^{-}$$

$$Zn^{+}_{ads} + Zn \rightleftharpoons Zn^{+}_{ads} + Zn^{2+}_{sol} + 2e^{-}$$

$$H_{ads} \rightleftharpoons H^{+} + e^{-}$$

$$H_2 \rightleftharpoons H^{+} + H_{ads} + e^{-}$$

After a long run of searching, sets of kinetic parameters have been found for which the model perfectly matches calculated zinc polarization with the experimental one, in the first half of charge/discharge cycle, attributed to the deposition of zinc ions. However, no matter which set of parameter is chosen, model of this simple scheme of reactions predicts a very low polarization of zinc during dissolution, which is in total contrast with the experimental results. In the first half of the cycle, the model matches the experimental one, only if one assumes a large portion of the zinc's surface is covered by hydrogen atoms, i.e., 70% and

90% of surface is covered by H_{ads} using the first and second sets of parameters, respectively (Figure 6.4). At the beginning of the charge, even more hydrogen atoms are adsorbed on the zinc surface; but as time passes, hydrogen evolution reduces the surface concentration of H_{ads}, and thus, the fraction of vacant adsorption sites for zinc reduction increases, which results in the decrease of polarization. In the discharged state, less H_{ads} exists on the surface because of the drop in the protons concentration in the solution due to the previous hydrogen evolution. Therefore, zinc is easily oxidized due to large fraction of free space on the surface. On the other hand, this model predicts large amount of hydrogen evolution which causes a large increase in pH. Therefore, this simple scheme of reaction cannot cover the experimental results.

6.3.2 Second scheme including direct reactions of zinc and water

We added the following reactions of zinc and water to the first scheme

$$Zn + H_2O \rightleftharpoons Zn(OH)_{ads} + H_{ads}$$

$$Zn(OH)_{ads} \rightleftharpoons Zn(OH)^+ + e^-$$

The closest agreement of the model with the experimental data is shown in Figure 6.5. Model leads to a polarization trend similar to the experiment, i.e., a drop in voltage at the beginning of charge, relatively constant voltage afterward, and a monotonic increase in voltage during discharge. However, the model results in a larger polarization, almost $0.01V$ in value, over the whole cycle. Any attempt to decrease the polarization by modifying the kinetic parameters eliminates the initial drop in voltage and almost flattens the dissolution polarization. Again, to achieve the polarization close to the experimental one, a large fraction of the surface must be occupied by hydrogen atoms so that hydrogen evolution is predominant.

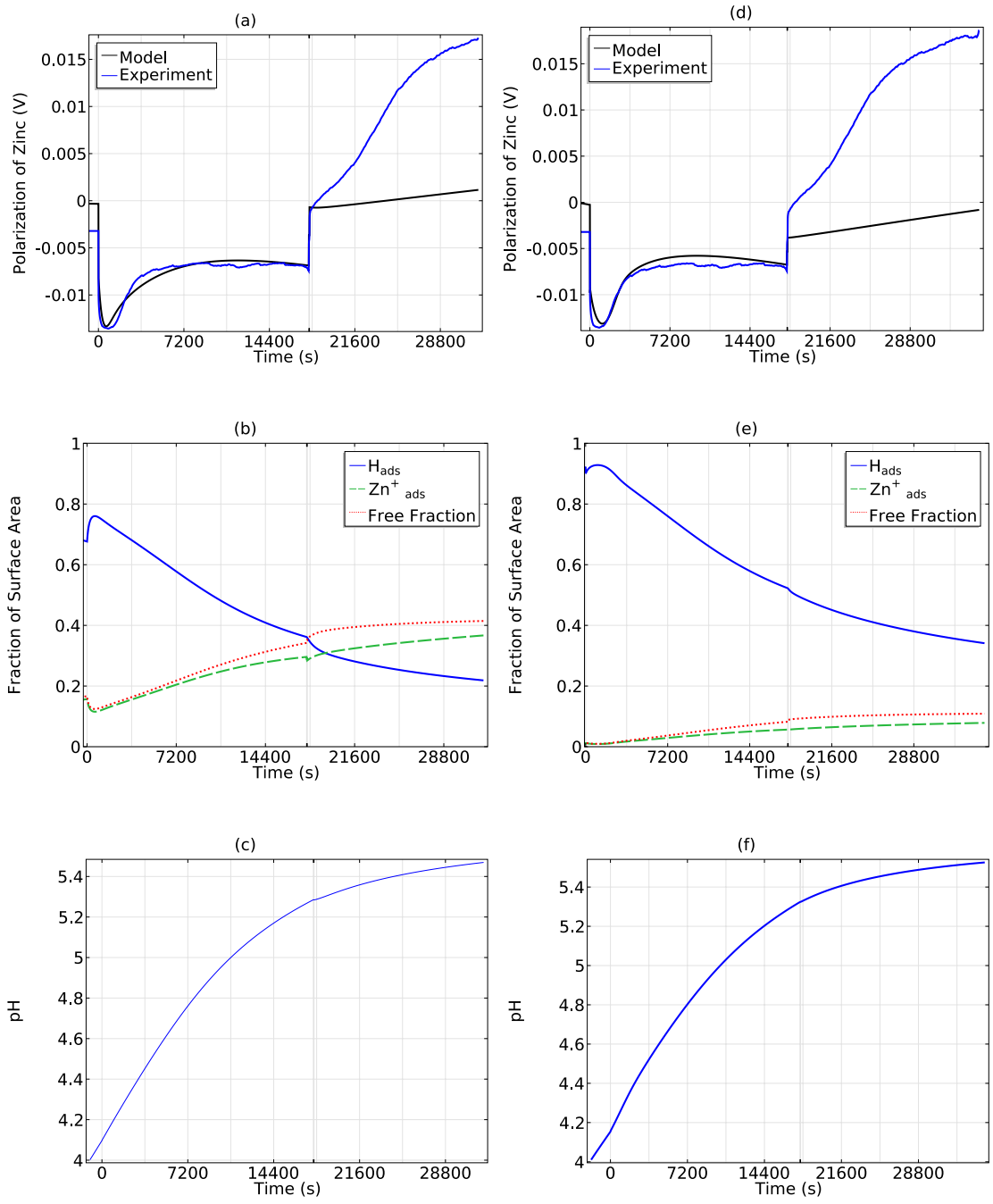

Figure 6.4: Modeling Results (a) Voltage, (b) Fraction of surface area occupied by species, (c) pH of the solution. (d), (e), and (f) same data for another set of kinetic parameters

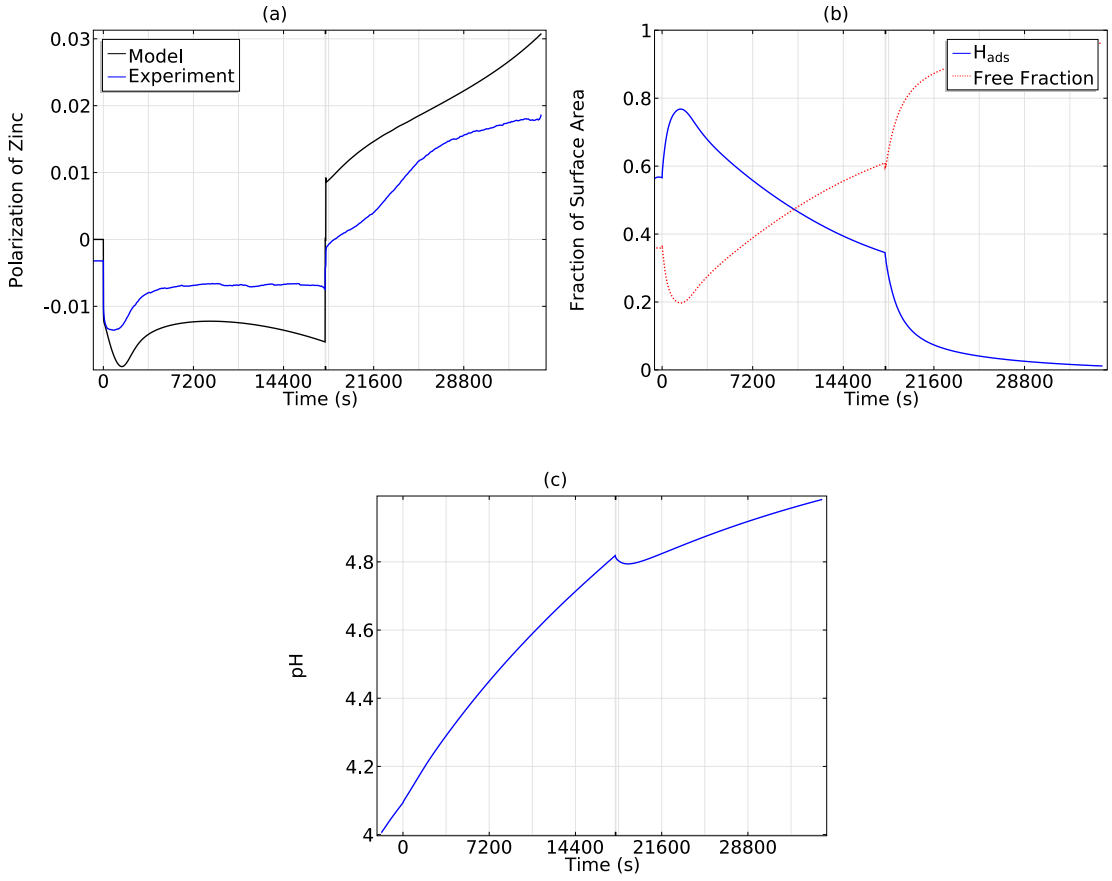

Figure 6.5: Modeling Results of second reaction scheme (a) Voltage, (b) Fraction of surface area occupied by species, (c) pH of the solution.

Chapter 7

Model Development of Zinc Half-Cell

The continuum model is employed to explain the electrochemical behavior of zinc electrodes. We simplified matters by disregarding the details of the electrochemical process at the cathode side. We assume a constant flux of lithium ions entering and leaving the solution medium at the cathode side during charge and discharge, respectively. Although the effect of the cathodic process, by some means, can be seen in the experimental results presented in the previous chapter, the order of their effects supports the validity of this approximation.

The model is based on the coupling between a series of homogeneous reactions which occur in the bulk of the aqueous electrolyte and heterogeneous reactions on the interface of the zinc electrode and electrolyte. The aqueous solution in this experiment contains 1 M Li_2SO_4 and 2 M $ZnSO_4$, with its pH adjusted to 4.00 by adding H_2SO_4. In $pH = 4$, all of these species have quite high solubility [39, 56]; therefore, we disregarded the possiblility of precipitation of the complex species.

7.1 Heterogeneous reactions

Although numerous studies have been done on the electrochemistry of zinc, it is still a subject of debate. Deposition is, generally, studied separately from dissolution. In both cases, irreversible electrochemistry is assumed (see Chapter 5). Typically, the theoretical studies done on zinc electrochemistry have focused on situations in which reactions occur at high rates. Therefore, irreversible electrochemical reactions are fairly feasible approximations. However, in batteries, the polarization of a zinc anode electrode is on the order of mV (see Chapter **??**) and thus, all electrochemical reactions must be considered to be reversible.

A list of assumed heterogeneous reactions that take place on the surface of a zinc anode is given in Table 7.1. Unbelievable as it may sound, complications arise by considering such a long, but unescapable list of reactions, and yet, this list is much simpler than the reality of zinc electrochemistry processes.

It is assumed that all the species and ions involved in the electrochemical reactions can be adsorbed on the surface. The significance of the assumption is that the surface of zinc would be mostly covered by the adsorbed species and ions, and thus, different reactions have to compete for free space on the surface if they are to occur. Moreover, each adsorbed species may act as a catalyst or inhibitor of the other reactions. On the other hand, the effect of these extra steps can be eliminated by setting a high rate for adsorption/desorption, i.e., Equations 7.3, 7.7, and 7.14.

Equations 7.1 and 7.2 are two 1-electron transfer steps, while Equation 7.3 accounts for adsorption and desorption of zinc ions. Since Zn^{+}_{ads} is unstable, the reaction in Equation 7.1 is considered fast, while the reactions in Equations 7.2 and 7.3 are rate-determining.

We disregarded the autocatalytic reaction:

$$Zn^{2+} + Zn^{+}_{ads} + e^{-} \rightleftharpoons 2Zn^{+}_{ads}$$

proposed by [13], because, the positively charged adion Zn^{+}_{ads}, naturally repels positively charged ions in general, and Zn^{2+}_{sol} ions in particular. Consequently, we consider that this reaction is not likey to occur.

Table 7.1: Set of assumed reactions on the surface of zinc anode.

Electrochemical reactions of zinc	
$Zn \rightleftharpoons Zn^{+}_{ads} + e^{-}$	(7.1)
$Zn^{+}_{ads} \rightleftharpoons Zn^{2+}_{ads} + e^{-}$	(7.2)
$Zn^{2+}_{ads} \rightleftharpoons Zn^{2+}_{sol}$	(7.3)
$Zn^{*} \rightleftharpoons Zn^{+}_{ads} + e^{-}$	(7.4)
$Zn + Zn^{*} \rightleftharpoons Zn^{*} + Zn^{2+}_{sol} + 2e^{-}$	(7.5)
$Zn^{*} + Zn^{+}_{ads} \rightleftharpoons Zn^{*} + Zn^{2+}_{sol} + e^{-}$	(7.6)
Hydrogen evolution reactions	
$H^{+}_{ads} \rightleftharpoons H^{+}_{sol}$	(7.7)
$H_{ads} \rightleftharpoons H^{+}_{ads} + e^{-}$	(7.8)
$H_2 \rightleftharpoons H^{+}_{sol} + H_{ads} + e^{-}$	(7.9)
$H_2 \rightleftharpoons 2H_{ads}$	(7.10)
Zinc-water reactions	
$Zn + H_2O \rightleftharpoons Zn(OH)_{ads} + H^{+}_{ads} + e^{-}$	(7.11)
$Zn(OH)_{ads} + H_2O \rightleftharpoons Zn(OH)_{2\ (ads)} + H^{+}_{ads} + e^{-}$	(7.12)
$Zn(OH)_{ads} \rightleftharpoons Zn(OH)^{+}_{ads} + e^{-}$	(7.13)
$Zn(OH)^{+}_{ads} \rightleftharpoons Zn(OH)^{+}_{sol}$	(7.14)
$Zn(OH)_{ads} \rightleftharpoons ZnO_{ads} + H_{ads}$	(7.15)
$Zn(OH)^{+}_{ads} + H_{ads} \rightleftharpoons Zn^{2+} + H_2O + e^{-}$	(7.16)

However, via Equation 7.4, we take into account the formation of perfect lattice growth sites Zn^* which act as catalysts, facilitating Zn^{2+}_{sol} reactions, through Equations 7.5 and 7.6. The two-electron-transfer reaction in Equation 7.5 is also proposed by Wiart's group [14]. Considering their proposed hypothesis of the diffusion of Zn^{+}_{ads} along the electrode surface, we raise the hypothesis of the possibility of dissociation of the complex $Zn^* - Zn^{+}_{ads}$ immediately after the the first electron-transfer, and before the occurrence of the second electron transfer in the deposition of Zn^{2+}_{sol}. On the other hand, upon the incidence of impact with a Zn^* site, Zn^{+}_{ads} can lose another electron and dissolve in the electrolyte easily. Therefore, we propose one more catalytic reaction via perfect site Zn^* by the reaction 7.6, which is a one-electron-transfer reaction. This reaction can be presumed to replace the autocatalytic reaction.

Hydrogen electrochemistry is described by the well-known reactions given in Equations 7.7 - 7.10. We assume a large overpotential for hydrogen evolution, but the reversible potential for Zn/Zn^{2+} is far below the equilibrium potential of hydrogen evolution; therefore, reactions 7.9 and 7.10 are taken to be almost irreversible.

After cycling of a ReHAB battery, black spots on the surface of its zinc electrode are observed, which are attributed to the corrosion products zinc oxides and zinc hydroxides. Johnson et al. [25] proposed the formation of zinc oxides as an intermediate species, namely ZnO_{ads}, to describe the dissolution of zinc in neutral solutions. An imprecise preliminary calculation based on the equilibrium conditions given in Table 5.1, and the initial concentrations of species in the solution of these experiments, reveals that a low amount of oxide complexes can exist in the electrolyte solution. Based on the information given in Table 5.1 as well as Figure 5.4, we consider the presence of $Zn(OH)_{2(ads)}$ and ZnO_{ads}, and also the intermediate species $Zn(OH)_{ads}$ in reversible electrochemical reactions on the surface of zinc electrodes. The significance of these reactions is, mostly, the fact that a large fraction of the zinc surface can be covered by hydroxide species, and thus inhibit other reactions. These reactions are very close to the ones proposed by Johnson et al. [25] (see chapter 5)

In this model, we assume that the activity of water is always 1 and also ignore the change

Table 7.2: Set of assumed reactions in the bulk of the aqueous solution.

$$Zn^{2+} + H_2O \rightleftharpoons Zn(OH)^+ + H^+ \tag{7.17}$$

$$LiSO_4^- \rightleftharpoons Li^+ + SO_4^{2-} \tag{7.18}$$

$$HSO_4^- \rightleftharpoons H^+ + SO_4^{2-} \tag{7.19}$$

in the amount of water in ReHAB due to decomposition of water. Since the batteries are not sealed, water evaporation also occurs. For simplicity, we ignore any water loss from the system.

7.2 Homogeneous reactions

Upon dissolving zinc and lithium salts in aqueous solution, various complexes form. Since the solution has a pH value of 4, from information in Table 5.1, the chance of the formation of solid phase complexes is pretty low. Therefore, we ignore precipitation reactions. Furthermore, we assume that the first dissociation of sulfate salts and sulfuric acid is complete, i.e.,

$$ZnSO_4 \rightarrow Zn^{2+} + SO_4^{2-}$$

$$Li_2SO_4 \rightarrow Li^+ + LiSO_4^-$$

$$H_2SO_4 \rightarrow H^+ + HSO_4^-$$

Among all complexes that zinc ion may form in aqueous solution at pH 4, $Zn(OH)^+$ has the highest concentration-of the order $10^{-5} mol/lit$. Thus, only the formation of $Zn(OH)^+$ is considered and other zinc complexes are discounted. The list of bulk reactions are given in Table 7.2. Therefore, the ions in solution are: Zn^{2+}, $Zn(OH)^+$, Li^+, $LiSO_4^-$, H^+, HSO_4^-, and SO_4^{2-}. The presence of other species, especially CO_2 and its complexes, is ignored.

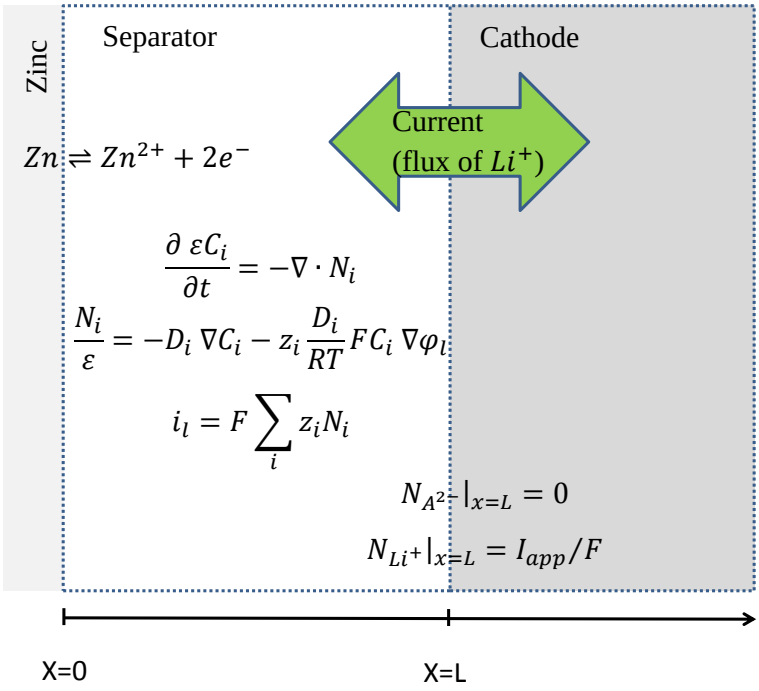

Figure 7.1: Schematic of the zinc-half-cell

7.3 Governing equations

Since the diameter of the zinc electrode is $12mm$ and the thickness of the separator is about $0.5mm$, we assume one-dimensional geometry. The schematic view of the zinc half-cell is presented in Figure 7.1. For simplicity, we ignore the cathode side and assume that a current carried by flux of Li^+ passes through the point $x = L$.

7.3.1 Governing equations in the bulk of the solution

In a porous medium, the governing equation for the material balance of an individual species is the continuity equation [26, 38]:

$$\frac{\partial \epsilon C_i}{\partial t} = -\nabla \cdot N_i + R_i \tag{7.20}$$

where ε represents the pore volume fraction of a porous electrode or separator and C_i is the concentration of Zn^{2+}, $Zn(OH)^{+}$, Li^{+}, $LiSO_4^{-}$, H^{+}, HSO_4^{-}, SO_4^{2-} and H_2. In a dilute electrolyte solution within the pores, the flux N_i of the species i is attributed to diffusion and migration as follows:

$$\frac{N_i}{\epsilon} = -D_i \nabla C_i - z_i \frac{D_i}{RT} F C_i \nabla \varphi_l \tag{7.21}$$

The diffusion coefficient D_i of species i is corrected based on Bruggeman's expression for porosity and tortuosity: $D_i = D_{i,0}\varepsilon^b$ and $b = 0.5$ [26], where $D_{i,0}$ is the diffusion coefficient in the bulk medium. z_i is the charge number of species i and φ_l is the liquid phase potential. The rate of production/consumption of species i due to all the reactions given in Table 7.2 can be written in the form

$$R_i = \sum_j s_{ij} \Re^j \tag{7.22}$$

where s_{ij} is the stoichiometric coefficient of species i in reaction j. The rate of reaction j, $\Re^j$, is given by

$$\Re^j = \prod_i C_i^{p_{ij}} k_f^j - \prod_i C_i^{q_{ij}} k_b^j \tag{7.23}$$

where k_f^j and k_b^j are the forward and backward rate constant of reaction j, respectively, and $p_{ij} = s_{ij}$ for forwards reactants, and $q_{ij} = -s_{ij}$ for backward reactants.

The liquid phase current density is given by

$$i_l = F \sum_i z_i N_i \tag{7.24}$$

we assume charge neutrality in the solution; therefore,

$$\nabla \cdot i_l = 0 \tag{7.25}$$

7.3.2 Dynamics of adsorption on the electrode surface

Let ϑ_s denote the fraction of unit area occupied by species s. Then the surface concentration Ω_s of that species is given by

$$\Omega_s = \lambda_s \vartheta_s \tag{7.26}$$

where λ_s represents the maximal surface concentration of the adsorbed species s. Let us call the smallest site on the surface u, in which only one of the smallest adsorbed species, i.e., Zn^* and H_{ads}, can reside. The ratio of the size of adsorbed species s to the site u is given by γ_s; that is, a single species s occupies γ_s sites. Then, the relation between λ_s and γ_s is given by

$$\lambda_s = \lambda_u / \gamma_s \tag{7.27}$$

where we set the value of λ_u to $2.72 \times 10^{-5} mol/m^2$, which is the concentration of zinc atoms in the compact plane (001) [13].

The rate of a heterogeneous reaction depends not only on the concentration of species in the immediate vicinity of the electrode surface, the surface concentration of adsorbed species and the overpotential, but also on the fraction of available free surface sites. Because the solution used is highly concentrated, the diffuse layer is very small and the concentration of species at the outer Helmholtz plane is, in very good approximation, equal to the ones beyond the diffuse layer [46, 38]. Therefore, we ignore the details of the double-layer structure. The rate of surface (heterogeneous) reactions is governed by the Butler-Volmer equation of the form [46, 38]

$$r_j = \lambda_u k_f^j \prod_{s,i} \vartheta_s^{p_{sj}} \; C_i^{p_{ij}} \vartheta_f^{\xi_j} \exp\big(\frac{\alpha_j F}{RT}\eta\big) - \lambda_u k_b^j \prod_{s,i} \vartheta_s^{q_{sj}} \; C_i^{q_{ij}} \vartheta_f^{\zeta_j} \exp\big(\frac{-\beta_j F}{RT}\eta\big) \tag{7.28}$$

where electrode potential is given by $\eta = \varphi_m - \varphi_l$, where φ_m and φ_l are the potential of the zinc metal and of the liquid phase in the immediate vicinity of the zinc metal, respectively. The terms $p_{s,j} = s_{sj}$ ($p_{i,j} = s_{ij}$) refers to anodic surface (bulk) species and $q_{i,j} = -s_{ij}$ ($q_{i,j} = -s_{ij}$) refers to cathodic surface (bulk) species. ϑ_f is the fraction of free sites on the

unit surface area, and ξ_j and ζ_j are the number of extra free sites needed for forward and backward reactions to happen, respectively, i.e.,

$$\begin{array}{ll} \xi_j = H\big(\sum_s s_{sj}\gamma_s\big) & \text{for forward reaction;} \\ \zeta_j = H\big(\sum_s -s_{sj}\gamma_s\big) & \text{for backward reaction.} \end{array} \tag{7.29}$$

where $H(\cdot)$ is the Heaviside function.

The rate of consumption or production of adsorbed surface species are

$$\frac{d\Omega_s}{dt} = \lambda_s \frac{d\vartheta_s}{dt} = \sum_s s_{sj} r_j \tag{7.30}$$

For simplicity, we assume charge neutrality on the surface; thus, upon the adsorption of a positively charged species an anion will be adsorbed too. Thus, the concentration of the adsorbed anions is given by

$$\Omega_{A^-} = \lambda_{A^-}\vartheta_{A^-} = \sum_s z_s \lambda_s \vartheta_s \tag{7.31}$$

On the other hand, the fraction of free sites on the surface is

$$\vartheta_f = 1 - \sum_{s,A} \vartheta_s \tag{7.32}$$

The current passing through the interface of the zinc electrode and electrolyte is the summation of all charge-transfers via the hetrogeneous reactions, i.e.,

$$I_{app} = \sum_j n_j r_j \tag{7.33}$$

where n_j is the number of electrons transferred by reaction j.

7.3.3 Boundary conditions

At the cathode side where $x = L$, we assumed the flux of each species to be zero, except for Li^+:

$$N_i|_{x=L} = \begin{cases} 0 & \text{if } i \not\equiv Li^+; \\ I_{app}/F & \text{if } i \equiv Li^+. \end{cases} \tag{7.34}$$

At the surface of the zinc anode, ODE BCs are coupled with the dynamic equations of species on the surface. The ingoing/outgoing flux of species depends on their contribution in the heterogeneous reactions, which is given by

$$N_i|_{x=0} = \begin{cases} -\frac{d}{dt}\Omega_{A^-} & \text{for } i \equiv LiSO_4^-; \\ \sum_j -s_{ij} r_j & \text{for the rest of species.} \end{cases} \tag{7.35}$$

Thus, for example, the fluxes of Li^+, HSO_4^-, and SO_4^{2-} are zero because they are not involved in the surface reactions. (For simplicity, we assumed that only $LiSO_4^-$, which has the highest concentration among all anions, can be adsorbed on the surface. After all, the numerical solution does not depend on this choice because the amount of anion species adsorbed on the surface is a very small fraction of their bulk concentration).

7.4 Summary of the assumptions and limits of the model

In this model temperature is assumed to be uniform and constant in the cell , so thermal effects on the system are ignored. We have also ignored the mechanical stresses in the solid phase. Considering the cell geometry, the model is developed in one dimension since the thickness of the cell is much smaller than its radius.

Because eight different type of species are dissolved in the electrolyte we employ the dilute solution theory in this model instead of concentrated solution theory is not applied. Also, the cathode side is totally replaced by a flux of Li^+ and its details are ignored. We also disregarded the surface morphology changes during desolation and deposition of zinc.

7.5 Model simulations

The governing equations are numerically solved using Mathematics module of COMSOL Multiphysics. The parameters used are listed in Tables 7.3-7.7.

Table 7.3: Diffusion Coefficients (D_i), taken from Ref. [56]. (*: assumed)

Transport parameters ($\times 10^9\, m^2/s$)	
D_{Li^+}	1.030
D_{H^+}	9.312
$D_{Zn^{2+}}$	0.71
$D_{SO_4{}^{2-}}$	1.065
$D_{HSO_4{}^-}$	1.33
$D_{LiSO_4{}^-}$	1.33 *
D_{ZnOH^+}	0.5 *
D_{H_2}	5.11

Table 7.4: Equilibrium conditions and kinetic parameters of the homogeneous reactions [39]

Equilibrium reaction	Equilibrium condition	Forward rate constant
$Zn^{2+} + H_2O = ZnOH^+ + H^+$	$log\left(\frac{[ZnOH^+][H^+]}{[Zn^{2+}]}\right) = -9.67$	0.54824 *
$HSO_4^- = H^+ + SO_4^{2-}$	$log\left(\frac{[SO_4^{2-}][H^+]}{[HSO_4^-]}\right) = -1.998$	0.51401 *
$LiSO_4^- = Li^+ + SO_4^{2-}$	$log\left(\frac{[SO_4^{2-}][Li^+]}{[LiSO_4^-]}\right) = -2$ *	0.025 *

*: Assumed.

Table 7.5: Assumed initial values for adsorbed species

Adsorbed species	γ_s	ϑ_s^0
Zn_{ads}^{+}	2	0.003
Zn_{ads}^{2+}	3	0.001
Zn^{*}	1	0.006
H_{ads}^{+}	2	0.01
H_{ads}	1	0.02
$Zn(OH)_{ads}$	2	0.07
$Zn(OH)_{2(ads)}$	3	0.2
$Zn(OH)_{ads}^{+}$	3	0.01
ZnO_{ads}	2	0.618
A^{-}	4	0.042

Table 7.6: Initial values of species' concentrations

Species	Concentration (mol/m^3)
Zn^{2+}	2000
H^{+}	0.1
$Zn(OH)^{+}$	0.0219
$LiSO_4^{-}$	1980.5
SO_4^{2-}	1014.6
HSO_4^{-}	9.87

Table 7.7: Kinetic parameters of the heterogeneous reactions

Reaction No.	Forward rate	Backward rate	α_j	β_j
1	700 [a]	93.3 [a]	0.5	0.5
2	1166.7 [a]	70 [a]	0.2	0.8
3	93.3 [a]	5.83 [b]	-	-
4	0.023 [a]	9.33×10^{-4} [a]	0.1	0.9
5	93.3 [a]	0.047 [b]	1	1
6	1.86×10^{5} [a]	700 [b]	0.2	0.8
7	2.52 [a]	641 [b]	0.5	0.5
8	0.007 [a]	0.45 [a]	0.5	0.5
9	0.0014 [b]	0.0746 [b]	0.5	0.5
10	0.07 [b]	0.37 [a]	-	-
11	8.75×10^{5} [a]	200 [a]	0.5	0.5
12	2250 [a]	0.63 [a]	0.5	0.5
13	7.15 [a]	0.126 [a]	0.5	0.5
14	0.001 [a]	55.8 [b]	-	-
15	0.0018 [a]	0.1 [a]	-	-
16	1400 [a]	875 [b]	0.5	0.5

[a]≡ s^{-1}, [b]≡ $m^3 mol^{-1} s^{-1}$

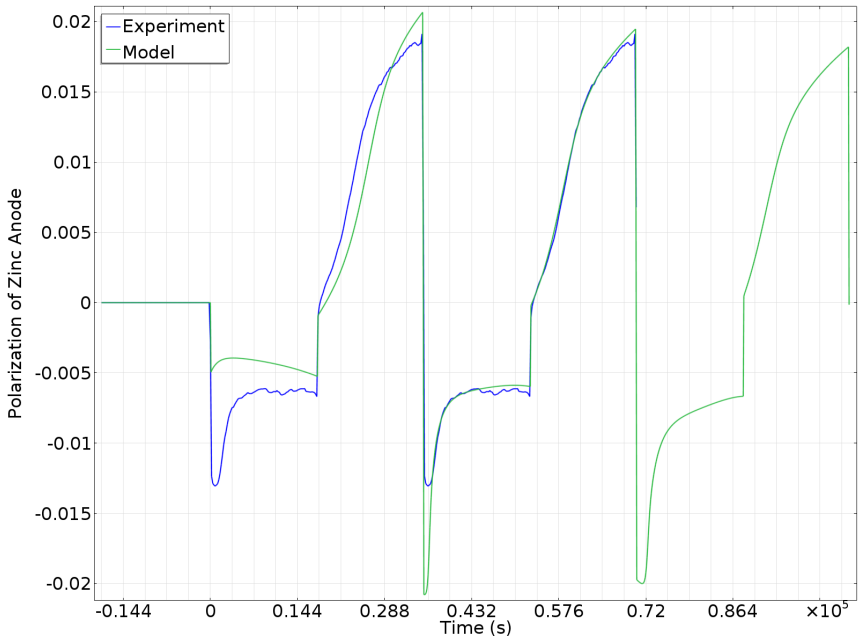

Figure 7.2: Polarization of zinc at 0.02C.

The initial values of species concentration in the solution are calculated based on the equilibrium conditions of homogeneous reactions given in Table 7.2. Upon placing zinc anode in ReHAB in contact with aqueous electrolyte, reactions of zinc corrosion and hydrogen evolution start to occur. As a result the concentrations of species, especially protons change over time. Therefore, in the modeling, we assumed the battery is left for 5 hour to relax before switching on the current.

The polarization profile of zinc anode obtained by our model at current rate of $0.2C$ is presented in Figure 7.2. The model result shows a perfect match with the experiment, in the second and third cycle, except for the minimum at the beginning of the charge. The voltage profiles for second and third cycle are very similar, but as we expect, small changes can be seen. This is because of continuous hydrogen evolution in the model that results in change of species concentration, especially the H^+ concentration, and as a consequence the voltage profile smoothly changes from cycle to cycle. In ReHAB, during charge, water

Figure 7.3: pH of the solution in the vicinity of zinc electrode.

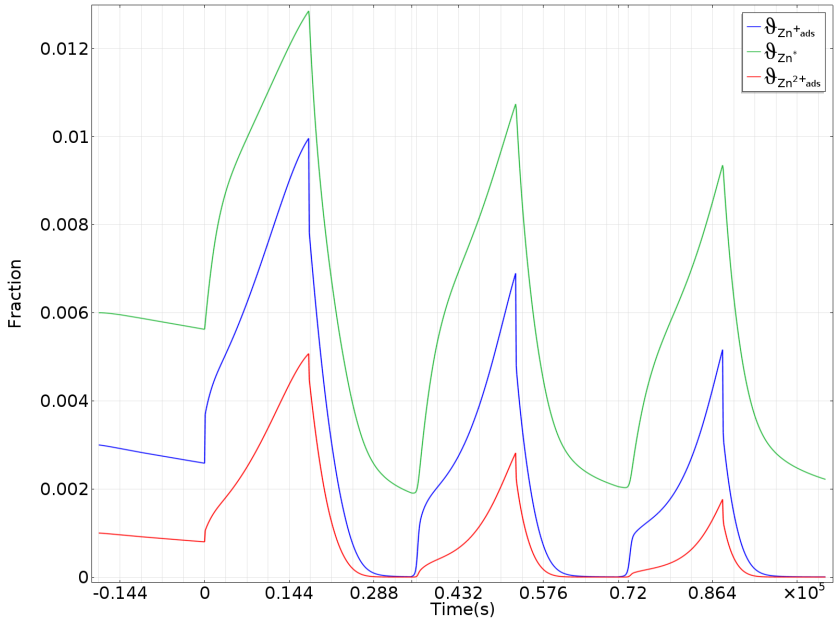

Figure 7.4: Fraction of adsorbed zinc ions on the electrode surface.

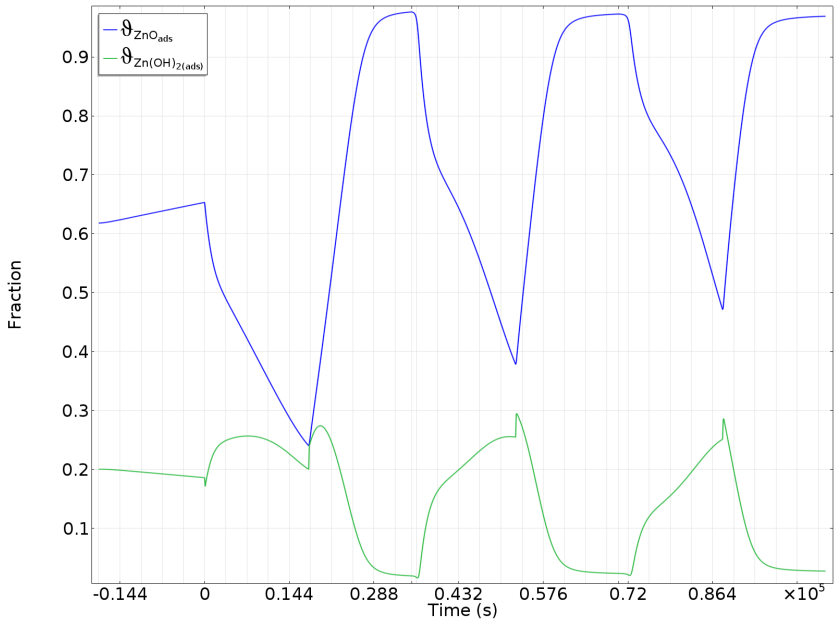

Figure 7.5: Fraction of zinc oxide and hydroxide on the electrode surface.

decomposes and oxygen evolves based on the following reaction

$$2H_2O \rightarrow O_2 + 4H^+ + 4e^-$$

Therefore, oxygen evolution decreases the pH locally. The produced H^+ diffuses in the electrolyte and thus, to some extent, compensates for the increase of pH at the anode side. Since this reaction obviously is not considered in our half-cell model, changes in the shape of voltage over cycling are expected.

The overall change in pH of the solution is obvious in Figure 7.3, which shows the pH of the solution at the immediate vicinity of the zinc electrode. During rest time, pH increases because of hydrogen evolution as expected. However, by the start of the charge, pH decreases from a value of ~ 4 to a value of ~ 3.7. At the same time, hydrogen evolution at the surface of the zinc electrode increases due to increase in polarization at the surface. During the discharge, pH increases to a value of ~ 4.3, higher than the starting value. The decrease in pH during discharge is attributed to the dissociation reaction of $LiSO_4^-$

given by Equation 7.18. By injection of Li^+ into the electrolyte, they are intended to form the complex of $LiSO_4^-$ with SO_4^{2-}; as a consequence of the consumption of SO_4^{2-} in this complex formation, HSO_4^- dissociates leading to release of H^+ into the electrolyte.

Figure 7.4 illustrates the variation of fraction of surface area occupied by zinc ions and also the prefect growth sites of Zn^*. This figure also explains the reason behind the big difference between the polarization of the first charge with the ones of the second and third. The initial values of the fractions are high at the beginning. As electrode experiences the discharge state, the fraction of adsorbed zinc ions and also Zn^* reduce very fast by dissolution and drops to much lower value compared to the initial value. Thus at the second and third charge state, polarization must increase to initiates the electrochemical reactions. The fraction of zinc oxide and hydroxide species (ZnO_{ads} and $Zn(OH)_{2(ads)}$) on the surface is presented in Figure 7.5. Despite of all the fluctuations and variation over time, the fraction of ZnO_{ads} increases over time.

The perfect growth site, Zn^*, plays an important role in determining the zinc polarization curve shape. Figure 7.6 illustrates the effect of Zn^* rate growth on polarization, that is controlled by the rate of the reaction in Equation 7.4. The rate constant of the reaction mostly affects the minimum in the polarization at the beginning of the charge, and almost the whole of the discharge. An increase in the rate of reaction causes Zn^* to dissolve faster during discharge, and consequently, not only the polarization during discharge increases, but also, because of lower concentration of perfect growth sites at the end of discharge, it has to increase at the beginning of the charge. While, after the minimum of voltage in charge, concentration of Zn^* grows fast and almost reaches semi-equilibrium with the Zn_{ads}^+ concentration. Therefore the rate of Zn^* product would be controlled by the concentration of Zn_{ads}^+. This phenomenon is obvious in Figure 7.7, which shows ϑ_{Zn^*} variation over time. As seen, different rate mostly causes variation of fraction at the end of the discharge.

To emphasize the importance of reactions of zinc and water, reaction 7.16 is turned off and the result is compared with the experiment in Figure 7.8. As a result the variation in

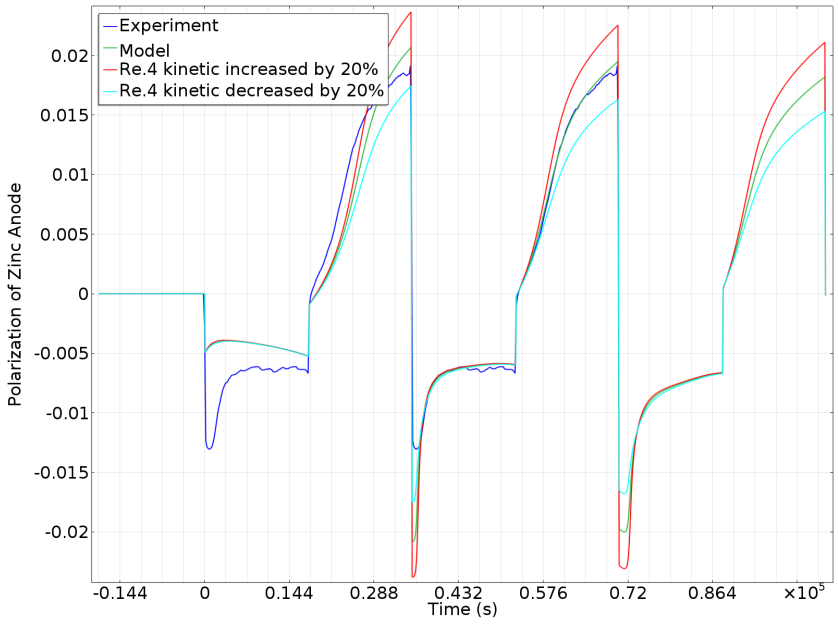

Figure 7.6: Polarization of zinc at 0.02C, for various kinetics of reaction 4.

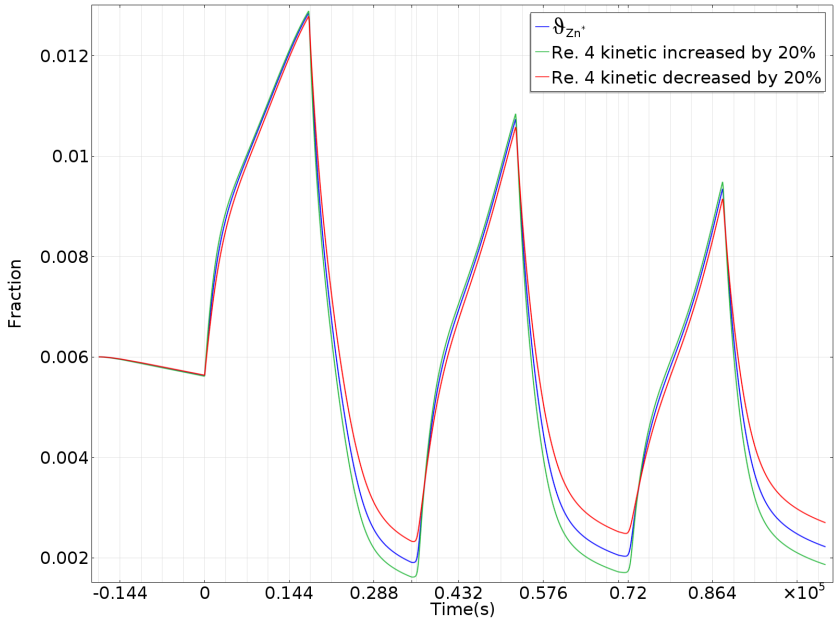

Figure 7.7: Fraction of perfect sites Zn^* on zinc surface, at various kinetics of reaction 4

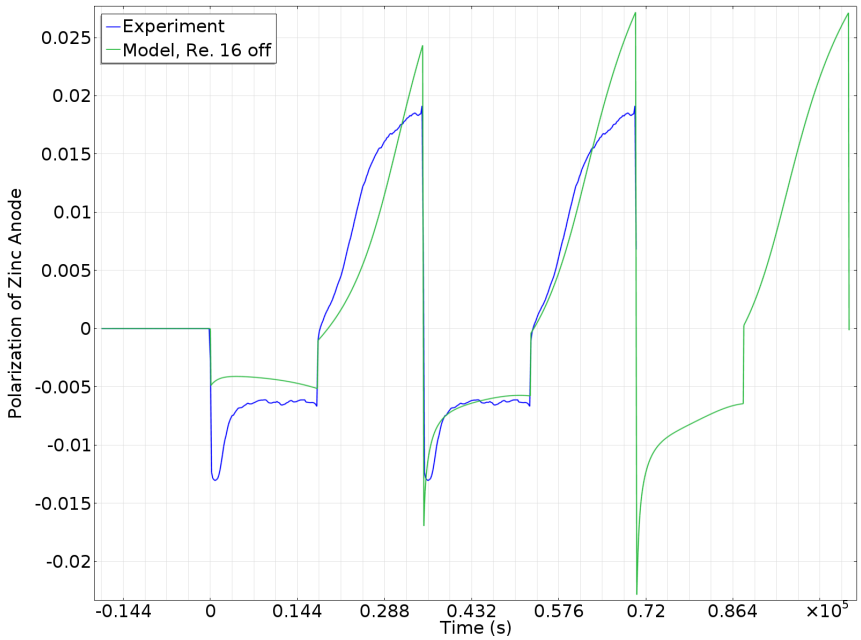

Figure 7.8: Polarization of zinc at 0.02C, when reaction 16 does not occur.

voltage becomes sharper, both in the beginning of the charge and at the end of discharge. Furthermore, overall shape of voltage is unstable, and changes by cycling. These are because reactions with water have two different roles. First, the intermediate species can occupy the surface and act as inhibitor to the other reactions; this results in widening the minimum of voltage at the beginning of the zinc deposition. Second, these reactions provide extra paths for zinc dissolution and deposition; as a consequence, the drop in voltage at the minimum decreases and more effectively, the polarization at the end of dissolution state decreases.

From the pH result shown in Figure 7.3, it is already known that the equilibrium constant of the homogenous reactions are very important on the behavior of the ReHAB. Figure 7.9 gives more details of the influence of the equilibrium conditions of homogenous reactions on the polarization of zinc electrode. Increasing in the equilibrium constant of the dissociation reaction of $LiSO_4^-$, given in Equation 7.18, by a factor of 10, results in

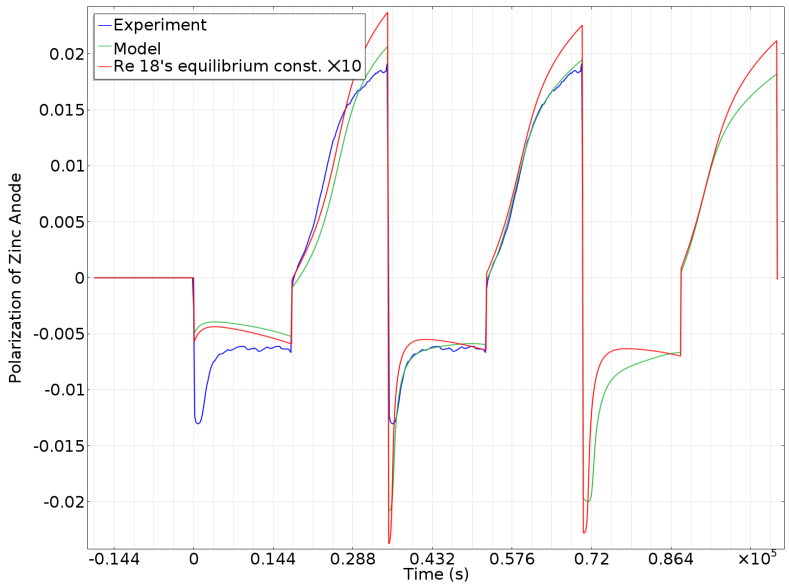

Figure 7.9: Polarization of zinc at 0.02C, when equilibrium constant of reaction 18 is increased by a factor of 10.

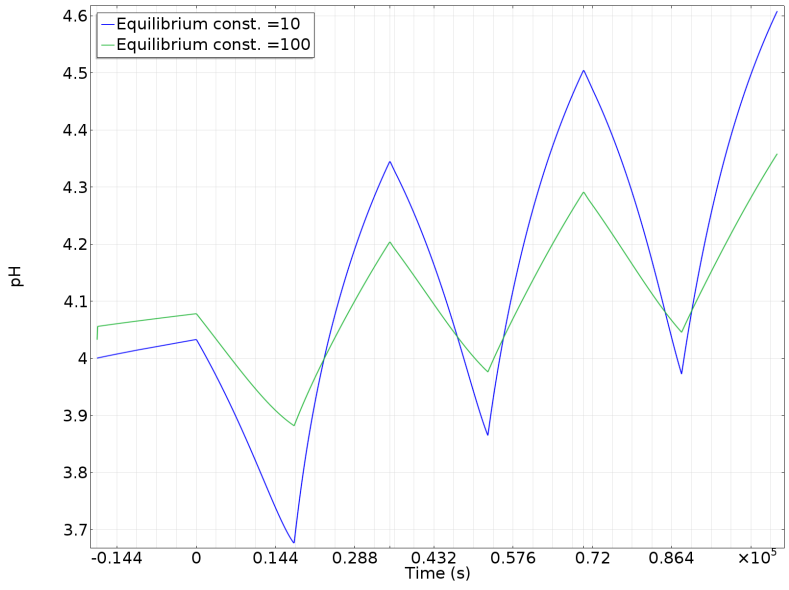

Figure 7.10: pH of the solution in the vicinity of zinc electrode, when equilibrium constant of reaction 18 is increased by a factor of 10.

deformation of voltage profile. Figure 7.10 compares the variation in pH over time due to the change in equilibrium constant. It is obvious that not only the initial pH is higher at higher equilibrium constant, but also less hydrogen evolution occurs, as the overall pH profile exhibits less raise by cycling. Higher pH is a direct consequence of increase in the concentration of SO_4^{2-} in the solution, which increase the intensity of formation of HSO_4^- complexes.

Chapter 8

Summary and Future Works

8.1 Summary of Li-S model

In this work, a summary of the possible electrochemical mechanism of rechargeable Li-S cell was presented. Furthermore, sensitivity analyses of a mathematical model of a Li-S cell for different parameters were made. In the first step, sensitivity analysis with respect to the discharge current rate and the conductivity of the cathode matrix was performed, the results of which provided details on the different characteristics of the cell. Depending on the discharge current (and the availability of dissolved sulfur), the relevant electrochemical reactions can occur either simultaneously or after the previous reactions are completed. The coincidence or non-coincidence of the electrochemical reactions determines the shape of the discharge plateau. Sharp changes in the voltage plateau are observed when the electrochemical reactions occur non-coincidentally, whereas a smooth plateau is expected in the coincidental case. In particular, if the first plateau does not appear, the first plateau can be made to re-appear by decreasing the discharge current. If the plateau appears at a low discharge rate, slow dissolution of elemental sulfur into the electrolyte causes a significant capacity loss. The simulation results also demonstrate that the active material can move into the separator during discharge.

Based on this model, it was shown that a minimum in the cathode conductivity is required (depending on the discharge current) below which the cell would not operate and above which no capacity loss is observed due to the conductivity. Low conductivity only causes a steeper deacrease in discharge voltage, particularly at the beginning and end of discharge.

The model predicts a very flat second plateau, which differs from the results of many experiments. This difference is a direct consequence of assuming that all the surfaces in the cathode are active for electrochemical reactions, ignoring the non-conductive nature of the solid sulfur and polysulfides. The model needs to be improved by including active surface loss due to the precipitation of polysulfides.

In this work, the behavior of a Li-S cell mathematical model was also investigated with respect to a wide mathematical range of the rate constants for the precipitation reactions. The rate of dissolution of elemental sulfur was observed to determine whether the discharge voltage has either one or two plateaus: more rapid dissolution than consumption by electrochemical reaction causes the two flat regions. In fact, k_k/I_{app} plays an important role in the behavior of the cell and its capacity. However, the model indicates a strong nonlinear behavior with respect to this ratio. More specifically, a "critical interval" for each rate constant exists whereby a tiny variation in the rate constant causes a large variation in the response of a cell, particularly in its capacity. The existence of these critical intervals suggests that the model requires modification in its formulation of the precipitation reactions.

Moreover, the model fails to reproduce the voltage plateau of the cases with capacity loss. In such cases, the final products in the cathode should consist of $Li_2S_{(s)}$, $Li_2S_{2(s)}$ and $Li_2S_{4(s)}$ and some un-utilized sulfur. Forcing the model to reflect this situation reforms the voltage plateau into shapes that are inconsistent with the experiment results. In other words, regardless of how well the model works in simulating a perfect battery that retains full capacity, it fails in the simulations of typical batteries that lose capacity. However, the model still provides a considerable amount of valuable information. For example, the

model indicates that for slow precipitation, more material diffuses to the separator, leading to a decreased cycle life. Specifically, this decreased cycle life phenomenon is stronger if the precipitant is one of the high polysulfides.

Most of the phenomena which are ignored in the model (such as the isolating nature of sulfur and polysulfides), can reduce the predicted discharge capacity; therefore, the model is also able to determine an upper limit on the optimal sulfur content. For low discharge rates, the model predicts that the discharge capacity percentage is reduced rapidly by increasing the sulfur content compared to that at high rates. This phenomenon is related to the assumed sequence of the reduction reaction chain. Thus, some modification to this assumption should be implemented in future models.

More importantly, the model cannot be charged unless we assume a large solubility of Li_2S, whereas the low lithium sulfides are known to have low solubility. For very large solubility, a typical two-voltage plateau during charging is reproduced, however the details of the model need modification to improve and shed light on charging mechanism

8.2 Future work on Li-S model

We suggest the following modifications to improve the model:

1. Adding other possible pathways of reduction of sulfur. In this model, a chain-like series of reduction reactions of sulfur was assumed, i.e. $S_{8(l)} \rightleftharpoons S_8^{2-} \rightleftharpoons S_6^{2-} \rightleftharpoons S_4^{2-} \rightleftharpoons S_2^{2-} \rightleftharpoons S^{2-}$. It was shown that this sequence cannot simulate the cases with capacity loss. On the other hand in experiments, other polysulfides have been detected in the discharge process, e.g. S_3^{2-} [4]. Therefore S_3^{2-} should be included in the model, and other pathways of reductions must be introduced. For example, $S_4^{2-} + 3e^- \rightleftharpoons S_2^{2-} + 2S^{2-}$ as the possible reduction reaction of S_4^{2-} can simultaneously produce S_2^{2-} and S^{2-} and help to include simultaneous precipitation of both low polysulfides.

2. A solid-solid electrochemical reaction, i.e., $Li_2S_{2(s)}+2e^-+2Li^+ \rightleftharpoons 2Li_2S_{(s)}$ is suspect of being the reason for the potential drop at the end of discharge [12]. Since low-lithium sulfides have negligible conductivity and no intercalation of Li is possible in the solid phase, such a reaction on limited areas of the interface of the solid particles and electrolyte extremely close to the conductive matrix of the cathode (intersection of three phases), can occur.

3. A solid-liquid oxidation, e.g., $2Li_2S_{(s)} \rightleftharpoons 4Li^+ + S_2^{2-} + 2e^-$, might happen in the same area explained above. However, unlike the solid-solid oxidation, solid-liquid oxidation continues as long as intersection of three phases exists.

4. Inclusion of equilibrium reactions between polysulfides. These reactions, however, are not electrochemical since no electron transfer occurs through the external circuit; they play important role in the performance of Li-S batteries. Various possible reactions have been proposed in the literature (e.g. [55, 21, 4]). Such reactions can facilitate the operation of the cell if they involve the different solid and liquid polysulfides phases, because they can compensate for the slow dissolution of the solid phases.

5. Modifying the governing equation of morphology changes during dissolution and precipitation reactions. Liquid phase electrochemical reactions occur at the interface of electrolyte and conductive matrix (porous carbon), while dissolution-precipitation reactions occur at the interface of electrolyte and solid polysulfides particles. Solid-solid or solid-liquid electrochemical reactions must occur at the interface of the solid polysulfide particles and electrolyte, which are close to intersection of three phases.

The model can be applied to other electrochemical cells which include multiple reactions and phases. Especially a comprehensive modeling of morphology changes, which involves in phase changes in the battery systems, is greatly useful in research and development of various battery systems.

8.3 Summary and future work on zinc model

A new model has been presented that can cover the low polarization regime for a zinc electrode in battery systems. Moreover, the reactions are assumed to be reversible. Even though the model is complicated, it gives an excellent match with the experimental result of the polarization of zinc in a ReHAB. The model explains the activation and self-catalyst effect seen in the deposition of zinc ions via the catalytic effect of perfect sites Zn^*. Two catalytic reactions are proposed for these sites to give the flexibility of both one-electron and two-electron charge-transfer reactions. The model can also explain the mystery of the monotonic increase of zinc polarization during dissolution, via dissolution of catalytic sites as well as covering the surface with zinc hydroxides. In particular, the modeled result of voltage in dissolution fits to the experimental result perfectly. Furthermore, the model gives reasonable prediction of the dynamics of species and the physicochemical situation of the system.

Unfortunately, lack of information for all aspects of the systems does not allow further justification of the model at the present time. Only the voltage profile is available, which the model matches well with. Further justification and improvement requires information such as the rate of hydrogen evolution, the rate of zinc corrosion, rate of oxygen evolution at the cathode side, equilibrium constant and kinetics of the homogenous reactions as well as heterogeneous reactions, type of the adsorbed species on the surface of zinc, etc.

This model can be used for optimization purposes, e.g., optimizing concentration of salts in the solution, type of material used as the cathode, pH value, the volume of electrolyte used and so on.

We suggest that more experiments must be done to gain information that leads to improve the model. Basic information such as the equilibrium constant is required. Experiments with high precision are necessary, since the order of polarization is mV. The model must also be tested for different experimental situations and conditions, in order to be justified and improved. On the other hand, a half-cell model cannot cover all the

physicochemical processes in the system. A full model of the battery can be developed, which can be used to understand the overall behavior of ReHAB, and also for optimization purposes. The model can be expanded to add the electrochemistry of zinc in neutral water as well as in alkaline solutions. Precise information leads to sound parametrization, then the model can be used to investigate the degradation of zinc anode by cycling.

8.4 Conclusion on modeling

This work presented the capability of the continuum model to describe and predict various aspects of different battery systems. Various physiochemical phenomena can be added to the model via efficient formulation of those phenomena. For instance, in this work, the precipitation and dissolution of polysulfides to the electrolyte were added to continuum theory in the Li-S model, and adsorption and desorption of species on zinc surface were efficiently coupled with the continuum model in the zinc half-cell model.

APPENDICES

Appendix A

Parameters and Symbols

a	Specific surface area of the cathode
a_0	Initial value of
b	Bruggeman coefficient
c_i	Concentration of species i ($i = Li^+, S_{8(l)}, S_8^{2-}, S_6^{2-}, S_4^{2-}, S_2^{2-}, S^{2-}$, and A^- (anion of the lithium salt used in the electrolyte)), mol/m^3
$c_{i,ref}$	Reference concentration of species i, mol/m^3
C_j	Portion of reaction j in the total capacity for an ideal complete discharge
$D_{i,0}$	Diffusion coefficient of species i in the bulk medium, m^2/s
D_i	Diffusion coefficient of species i in the porous medium, m^2/s
F	Faraday constant, $C/equi$
i_j	Current density due to reaction j, A/m^2
$i_{j,ref}$	Exchange current density of the electrochemical reaction j at the reference concentrations, A/m^2
i_l	Superficial current density in the liquid phase, A/m^2
i_s	Superficial current density in the solid phase, A/m^2
I_{app}	Applied current density, A/m^2
I_J^N	Normalized current due to electrochemical reaction j

$K_{sp,k}$	Solubility product of precipitate k
k_k	Rate constant of precipitate k
L	Thickness of the cell, m
L_s	Thickness of the separator, m
N_i	Superficial flux of species i, $mol\ m^2/s$
n_j	Number of electrons transferred in electrochemical reaction j
$p_{i,j}$	Anodic reaction order of species i in electrochemical reaction j
$q_{i,j}$	Anodic reaction order of species i in electrochemical reaction j
R	Gas constant, $J\ mol^{-1}K^{-1}$
R_i	Production rate of species i due to precipitation reactions, $mol\ m^3s^{-1}$
R'_k	Rate of precipitation of solid species k, $mol\ m^3s^{-1}$
r_i	Production rate of species i due to electrochemical reactions, $mol\ m^3s^{-1}$
$s_{i,j}$	Stoichiometric coefficient of species i in electrochemical reaction j
T	Temperature, K
T_{DC}	Total time of an ideal complete discharge, s
t	Time, s
U_j^θ	Standard Open Circuit Potential (OCP) of electrochemical reaction j
$U_{j,ref}$	OCP of electrochemical reaction j at reference concentrations, V
$\widetilde{V}_k$	Molar volume of the precipitate k, m^3/mol
$\widetilde{V}_k$	Charge number of species i
α_{aj}	Anodic transfer coefficient of reaction j
α_{cj}	Cathodic transfer coefficient of reaction j
ε	Porosity of the separator and cathode
ε_k	Volume fraction of precipitate k in the separator and cathode
φ_l	Potential in the liquid phase, V
φ_s	Potential in the solid phase, V
$\gamma_{i,k}$	Number of ionic species i produced by dissociation of precipitate k
η_j	Overpotential for electrochemical reaction j
σ_j	Effective conductivity of the solid phase of the cathode, S/m

ξ_j Morphology parameter

References

[1] James R. Akridge, Yuriy V. Mikhaylik, and Neal White. Li/s fundamental chemistry and application to high-performance rechargeable batteries. *Solid state ionics*, 175(1):243–245, 2004.

[2] Nurhaswani Alias and Ahmad Azmin Mohamad. Advances of aqueous rechargeable lithium-ion battery: A review. *Journal of Power Sources*, 274:237–251, 2015.

[3] Michel Armand and Jean-Marie Tarascon. Building better batteries. *Nature*, 451(7179):652–657, 02 2008.

[4] Cline Barchasz, Florian Molton, Carole Duboc, Jean-Claude Leprtre, Sbastien Patoux, and Fannie Alloin. Lithium/sulfur cell discharge mechanism: an original approach for intermediate species identification. *Analytical chemistry*, 84(9):3973–3980, 2012.

[5] Chantal Cachet, F Ganne, Georges Maurin, Jacques Petitjean, Vincent Vivier, and Robert Wiart. Eis investigation of zinc dissolution in aerated sulfate medium. part i: bulk zinc. *Electrochimica acta*, 47(3):509–518, 2001.

[6] Chantal Cachet and Robert Wiart. Reaction mechanism for zinc dissolution in chloride electrolytes. *Journal of Electroanalytical Chemistry and Interfacial Electrochemistry*, 129(1):103–114, 1981.

[7] Chantal Cachet and Robert Wiart. Zinc electrowinning in acidic sulfate electrolytes: impedance analysis and modeling of the influence on nickel impurities. *Journal of The Electrochemical Society*, 141(1):131–140, 1994.

[8] Zheng Chang, Yaqiong Yang, Minxia Li, Xiaowei Wang, and Yuping Wu. Green energy storage chemistries based on neutral aqueous electrolytes. *Journal of Materials Chemistry A*, 2(28):10739–10755, 2014.

[9] Young-Jin Choi, Young-Dong Chung, Chang-Yong Baek, Ki-Won Kim, Hyo-Jun Ahn, and Jou-Hyeon Ahn. Effects of carbon coating on the electrochemical properties of sulfur cathode for lithium/sulfur cell. *Journal of Power Sources*, 184(2):548–552, 2008.

[10] Rezan Demir-Cakan, Mathieu Morcrette, Jean-Bernard Leriche, and Jean-Marie Tarascon. An aqueous electrolyte rechargeable li-ion/polysulfide battery. *Journal of Materials Chemistry A*, 2(24):9025–9029, 2014.

[11] Bruce Dunn, Haresh Kamath, and Jean-Marie Tarascon. Electrical energy storage for the grid: a battery of choices. *Science*, 334(6058):928–935, 2011.

[12] Brian L Ellis, Kyu Tae Lee, and Linda F Nazar. Positive electrode materials for li-ion and li-batteries. *Chemistry of Materials*, 22(3):691–714, 2010.

[13] Israel Epelboin, Mekki Ksouri, and Robert Wiart. On a model for the electrocrystallization of zinc involving an autocatalytic step. *Journal of The Electrochemical Society*, 122(9):1206–1214, 1975.

[14] Israel Epelboin, Mekki Ksouri, and Robert Wiart. Kinetics of zinc electrocrystallization correlated with the deposit morphology. In *Faraday Symposia of the Chemical Society*, volume 12, pages 115–125. Royal Society of Chemistry, 1977.

[15] Jean Fanous, Marcus Wegner, Jens Grimminger, nne Andresen, and Michael R Buchmeiser. Structure-related electrochemistry of sulfur-poly (acrylonitrile) composite cathode materials for rechargeable lithium batteries. *Chemistry of Materials*, 23(22):5024–5028, 2011.

[16] Alejandro A Franco. Multiscale modelling and numerical simulation of rechargeable lithium ion batteries: concepts, methods and challenges. *RSC Advances*, 3(32):13027–13058, 2013.

[17] F Ganne, Chantal Cachet, Georges Maurin, Robert Wiart, E Chauveau, and Jacques Petitjean. Impedance spectroscopy and modelling of zinc deposition in chloride electrolyte containing a commercial additive. *Journal of applied electrochemistry*, 30(6):665–673, 2000.

[18] Mahmoudreza Ghaznavi and P Chen. Sensitivity analysis of a mathematical model of lithium–sulfur cells part i: Applied discharge current and cathode conductivity. *Journal of Power Sources*, 257:394–401, 2014.

[19] Mahmoudreza Ghaznavi and P Chen. Sensitivity analysis of a mathematical model of lithium–sulfur cells: Part ii: Precipitation reaction kinetics and sulfur content. *Journal of Power Sources*, 257:402–411, 2014.

[20] John B Goodenough and Kyu-Sung Park. The li-ion rechargeable battery: a perspective. *Journal of the American Chemical Society*, 135(4):1167–1176, 2013.

[21] Dong-Hun Han, Bum-Soo Kim, Shin-Jung Choi, Yongju Jung, Juhyoun Kwak, and Su-Moon Park. Time-resolved in situ spectroelectrochemical study on reduction of sulfur in n, n-dimethylformamide. *Journal of The Electrochemical Society*, 151(9):E283–E290, 2004.

[22] Toru Hara, Aishuak Konarov, Almagul Mentbayeva, Indira Kurmanbayeva, and Zhumabay Bakenov. High mass-loading of sulfur-based cathode composites and polysulfides stabilization for rechargeable lithium/sulfur batteries. *Frontiers in Energy Research*, 3:22, 2015.

[23] Kazem Jeddi, Mahmoudreza Ghaznavi, and P Chen. A novel polymer electrolyte to improve the cycle life of high performance lithium–sulfur batteries. *Journal of Materials Chemistry A*, 1(8):2769–2772, 2013.

[24] Xiulei Ji and Linda F Nazar. Advances in li–s batteries. *Journal of Materials Chemistry*, 20(44):9821–9826, 2010.

[25] James W Johnson, Yun-Chung Sun, and William Joseph James. Anodic dissolution of zn in aqueous salt solutions. *Corrosion Science*, 11(3):153–159, 1971.

[26] Keith E Johnson. What's an ionic liquid? *Interface-Electrochemical Society*, 16(1):38–41, 2007.

[27] Hideaki Kita. Periodic variation of exchange current density of hydrogen electrode reaction with atomic number and reaction mechanism. *Journal of the Electrochemical Society*, 113(11):1095–1111, 1966.

[28] VS Kolosnitsyn and EV Karaseva. Lithium-sulfur batteries: Problems and solutions. *Russian Journal of Electrochemistry*, 44(5):506–509, 2008.

[29] Karthikeyan Kumaresan, Yuriy Mikhaylik, and Ralph E White. A mathematical model for a lithium–sulfur cell. *Journal of the Electrochemical Society*, 155(8):A576–A582, 2008.

[30] Wu Li and Jeff R. Dahn. Lithium-ion cells with aqueous electrolytes. *Journal of the Electrochemical Society*, 142(6):1742–1746, 1995.

[31] Wu Li, Jeff R. Dahn, and David S. Wainwright. Rechargeable lithium batteries with aqueous electrolytes. *Science*, 264(5162):1115–1118, 1994.

[32] Wu Li, William R. McKinnon, and Jeff R. Dahn. Lithium intercalation from aqueous solutions. *Journal of the Electrochemical Society*, 141(9):2310–2316, 1994.

[33] Jia-Yan Luo, Wang-Jun Cui, Ping He, and Yong-Yao Xia. Raising the cycling stability of aqueous lithium-ion batteries by eliminating oxygen in the electrolyte. *Nature chemistry*, 2(9):760–765, 2010.

[34] Yuriy V. Mikhaylik and James R. Akridge. Polysulfide shuttle study in the li/s battery system. *Journal of the Electrochemical Society*, 151(11):A1969–A1976, 2004.

[35] Manickam Minakshi, Pritam Singh, Dominique Appadoo, and Danielle E Martin. Synthesis and characterization of olivine linipo 4 for aqueous rechargeable battery. *Electrochimica Acta*, 56(11):4356–4360, 2011.

[36] Manickam Minakshi, Pritam Singh, David RG Mitchell, Touma B Issa, and Kathryn Prince. A study of lithium insertion into mno 2 containing tis 2 additive a battery material in aqueous lioh solution. *Electrochimica acta*, 52(24):7007–7013, 2007.

[37] Manickam Minakshi, Pritam Singh, Stephen Thurgate, and Kathryn Prince. Electrochemical behavior of olivine-type limnpo4 in aqueous solutions. *Electrochemical and solid-state letters*, 9(10):A471–A474, 2006.

[38] John Newman and Karen E Thomas-Alyea. *Electrochemical systems*. John Wiley & Sons, 2012.

[39] Marcel Pourbaix. *Atlas of electrochemical equilibria in aqueous solutions*. Pergamon Press, 1974.

[40] Venkatasailanathan Ramadesigan, Paul WC Northrop, Sumitava De, Shriram Santhanagopalan, Richard D Braatz, and Venkat R Subramanian. Modeling and simulation of lithium-ion batteries from a systems engineering perspective. *Journal of The Electrochemical Society*, 159(3):R31–R45, 2012.

[41] Ho Suk Ryu, Zaiping Guo, Hyo Jun Ahn, Gyu Bong Cho, and Huakun Liu. Investigation of discharge reaction mechanism of lithium— liquid electrolyte— sulfur battery. *Journal of Power Sources*, 189(2):1179–1183, 2009.

[42] Min-Kyu Song, Elton J Cairns, and Yuegang Zhang. Lithium/sulfur batteries with high specific energy: old challenges and new opportunities. *Nanoscale*, 5(6):2186–2204, 2013.

[43] Wei Tang, Yusong Zhu, Yuyang Hou, Lili Liu, Yuping Wu, Kian Ping Loh, Hanping Zhang, and Kai Zhu. Aqueous rechargeable lithium batteries as an energy storage system of superfast charging. *Energy & Environmental Science*, 6(7):2093–2104, 2013.

[44] Michael M Thackeray, Christopher Wolverton, and Eric D Isaacs. Electrical energy storage for transportationapproaching the limits of, and going beyond, lithium-ion batteries. *Energy & Environmental Science*, 5(7):7854–7863, 2012.

[45] Richard Van Noorden. Sulphur back in vogue for batteries. *Nature*, 498(7455):416–417, 2013.

[46] Klaus J Vetter. *Electrochemical kinetics: theoretical aspects*. Elsevier, 2013.

[47] Chong Wang, Jia-jia Chen, Yi-ning Shi, Ming-sen Zheng, and Quan-feng Dong. Preparation and performance of a core–shell carbon/sulfur material for lithium/sulfur battery. *Electrochimica Acta*, 55(23):7010–7015, 2010.

[48] Xujiong Wang, Yuyang Hou, Yusong Zhu, Yuping Wu, and Rudolf Holze. An aqueous rechargeable lithium battery using coated li metal as anode. *Scientific reports*, 3, 2013.

[49] Yonggang Wang, Jin Yi, and Yongyao Xia. Recent progress in aqueous lithium-ion batteries. *Advanced Energy Materials*, 2(7):830–840, 2012.

[50] Robert Wiart. Elementary steps of electrodeposition analysed by means of impedance spectroscopy. *Electrochimica Acta*, 35(10):1587–1593, 1990.

[51] Rui Xu, Ilias Belharouak, Xiaofeng Zhang, Bryant Polzin, and James CM Li. New developments in lithium sulfur batteries. In *SPIE Defense, Security, and Sensing*, pages 872804–872804. International Society for Optics and Photonics, 2013.

[52] Jing Yan, Jing Wang, Hao Liu, Zhumabay Bakenov, Denise Gosselink, and P Chen. Rechargeable hybrid aqueous batteries. *Journal of Power Sources*, 216:222–226, 2012.

[53] Baogui Zhang, Xue Qin, Guoran Li, and Xueping Gao. Enhancement of long stability of sulfur cathode by encapsulating sulfur into micropores of carbon spheres. *Energy & Environmental Science*, 3(10):1531–1537, 2010.

[54] Hanping Zhang, Xin Wu, Tao Yang, Shanshan Liang, and Xiaojian Yang. Cooperation behavior between heterogeneous cations in hybrid batteries. *Chemical Communications*, 49(85):9977–9979, 2013.

[55] Sheng S Zhang. Liquid electrolyte lithium/sulfur battery: fundamental chemistry, problems, and solutions. *Journal of Power Sources*, 231:153–162, 2013.

[56] Xiaoge Gregory Zhang. *Corrosion and electrochemistry of zinc*. Springer Science & Business Media, 2013.